UNIVERSITY COLLEGE OF SOUTHEAST NORWAY

Master Thesis

# Investigation of Element Variations in Ultrasound Transducer Arrays by Electrical Impedance Measurements

Author:

Duy Le Anh

Supervisor:

Prof. Lars Hoff

Co-supervisor:

Dr. Tung Manh

A thesis submitted in fulfillment of the requirements

for the degree of Master of Engineering

in the

Department of Micro and Nano Systems Technology

May 2016

# Abstract

The use of ultrasonic transducer array for medical applications has experienced a revolution in recent years. An ultrasonic transducer array is a transducer that contains a number of individually connected elements. Variations of the individual elements from their ideal state have significant effects on the performance of the linear transducer arrays.

Due to practical requirements, the study in this thesis mainly focused on investigating the variance in the fabricated transducer structures. Single-element transducers using different matching layer materials were fabricated and compared. Electrical impedance and pulse-echo test were performed.

Linear arrays consisting of only piezoelectric material were fabricated and characterized. Linear arrays consisting of a piezoelectric material and a DML (Dematching Layer) substrate were also fabricated and characterized. The structure of transducer arrays varied from element to element as prior expected due to fabrication process. Different sources causing variance in electrical impedance of each transducer structures were extensively investigated. Modeling such as 1D and 2D FEM simulations were build and compared to the experimental observations. More intriguingly, a novel bonding technique named SLID (Solid-Liquid Interdiffusion) to assembly stacks of piezoelectric ultrasonic transducers was also implemented and characterized. The performance of the transducer using this novel bonding method will be compared to that of the transducer using conventional epoxy bonding method. Advantages and disadvantages of both bonding methods were presented with simulations and characterization results. Based on these measurement results, essential recommendations was pointed out that SLID bonding method would be a potential bonding one for implementing high frequency transducers.

# Acknowledgements

I would like to express my great appreciation to my supervisor, Professor Lars Hoff for his valuable suggestions and discussion during my Master study. Prof. Lars Hoff's enthusiastic support and comments were helpful to the planning and development of this thesis.

I would like to express my deep gratitude to Dr. Tung Manh for his continuous guidance and encouragement from initial training steps to the completion of this thesis. He has shown me how to do research scientifically and motivated me all the time. Without his generous help and instructive advices, this thesis would not have been possible. I am especially grateful to Zekija Ramic, Muhammad Tayyib for their kind supports in my experiment.

I would like to give special thank to my research colleagues, seniors, juniors and friends, especially Binh Truong and Vy Nguyen for their meaningful discussions. The support and encouragement of all the faculty and staff members of the department are also greatly appreciated and acknowledged.

Most importantly, I would like to dedicate my work to my family, whose love and great encouragement enhance me to go further in my education.

# Contents

# List of Figures

# List of Tables

# Abbreviations

| | |
|---|---|
| SLID | Solid-Liquid Interdiffusion |
| PZT | Lead Zirconate Titanate |
| DML | Dematching layer |
| BW | Bandwidth |
| TM | Thickness Mode |

# CHAPTER 1. Introduction

## 1.1 Medical Ultrasound Imaging

Human ear can detect sound waves with frequencies between 20 Hz and 20,000 Hz (20 KHz). Ultrasounds are sound waves with frequencies above this range. Ultrasound has been extensively used in many different fields. The first practical application of ultrasound was reported during the World War I in locating submarines [1], [2]. In nondestructive testing (NDT) method, ultrasound is used to detect invisible flaws and measure thickness of objects without harming the objects [3]. The use of ultrasound as a potential imaging tool was discovered in the 1940s [4]. Then, it has been widely used in medical applications such as pelvis, cardiology, ophthalmology and orthopedics [5]. Compared with other diagnostic methods such as X-ray, Computed Tomography (CT), and Magnetic Resonance Imaging (MRI), ultrasound is considered as a desired imaging method because of its low cost, non-invasiveness, and portability. Today, two common uses of ultrasound imaging are the scanning of the fetus during pregnancy and the scanning of the heart.

## 1.2 Research motivations

One of the most important components in a medical ultrasound imaging system is the ultrasound transducer. Most ultrasonic transducers currently consist of a piezoelectric ceramic/piezocomposite active element, operating in thickness mode, one heavy/soft backing on the rear side and several matching layers on the front side of the piezoelectric layer to effectively couple energy from the active element to the human tissue. Transducers come in many shapes and sizes, but can be generally categorized into single element transducers and transducer arrays. Today, transducer arrays are desired in most clinical uses. To evaluate the performance of an ultrasonic array, several measurement tests such as pulse echo, electrical impedance, insertion loss test, etc. need to be performed. Among of them, electrical impedances of the elements initially give valuable information about the performance of an array. Ideally, these impedances must be identical across elements. However, this is not achievable due to variations between elements in an array during the fabrication process, i.e. dicing and bonding. This study mainly focuses on investigating possible sources for such variations, and estimates the contributions of these sources on the electrical impedance. The fabricated arrays were investigated under microscope, and the measured impedances were compared to FEM simulations.

One critical component that might change the electrical response and consequently degrade the entire performance of a transducer is the bondlines between layers. Adhesives such as epoxies are conventionally used as bonding materials between active and passive layers. The epoxy's bondline thickness must be significantly smaller compared to the ultrasound wavelength and better match to the acoustic impedance of piezoelectric material. Therefore, a novel bonding technique based on solid liquid-interdiffusion (SLID) to produces an intermetallic bondline between active and passive layers has been developed at IMST, HSN. This technology potentially provides relaxation on the requirements of both bondline thickness and thickness uniformity. This work also investigates the variations across elements in arrays using this novel bonding method by electrical impedance measurements and results are compared to those from conventional epoxy bonding method. The variances in electrical impedance of the elements in the transducer arrays implemented by these two bonding methods were also investigated and compared to FEM simulations. Based on these characterization and simulation results, advantages and disadvantages of the two bonding methods are discussed.

### 1.3 Objectives of this thesis

The objectives of "Fabricate and Investigate Electrical Impedance Variation of Ultrasound Transducer Arrays" thesis are:

- To fabricate linear transducer array and characterize electrical impedances of the element. Particular interest is on comparing the elements in the array and relate observed variations to variations in the fabricated structures. Corresponding models are also built in COMSOL to explain the measurement results and variations between array elements.
- Different bonding methods will be implemented in linear array structures. Specially, SLID and conventional epoxy bonding method will be investigated and characterized. Variations in electrical impedance of the elements in the transducer arrays implemented by these two bonding methods were also investigated and compared to FEM simulations. A comprehensive comparison between these two bonding methods are also presented.

Based on these objecives, the following tasks have been performed:

- Fabricate linear transducer array and characterize electrical impedances of the elements. Variations in structure and changes in material between element to

element were detected and 2D FEM simulations were built to explain the measurement results and variations between array elements.

- Linear transducer arrays using conventional epoxy bonding method were fabricated, investigated and characterized. Linear transducer arrays using SLID bonding method were investigated and characterized. Variations in electrical impedance of the elements in the transducer arrays were investigated and compared to FEM simulations. Based on these results, an extensive comparison between these two bonding methods was pointed out.
- In addition, single element transducers operating at 4 MHz were designed, simulated, and fabricated and characterized by the student. Each single element transducer was built from a circular piezoelectric disc with one matching layer and air backing. Modelling of the transducers was done using one-dimensional Mason-based program in Matlab and 2D FEM in COMSOL. The transducers were characterized by electrical impedances measurements. This task was done at the early stage of the master project to train the student using available tools in the ultrasound lab at HSN and hence helped the student to get acquainted with the entire process to make an ultrasound transducer. This task was also to provide other master student "in-house" transducers used for her pulse-echo measurements.

### 1.4 Thesis structure

The thesis is organized as follows. An introduction of medical ultrasound imaging system, research motivations, and the objectives of this thesis are given in Chapter 1. Chapter 2 presents the theoretical background as well as the literature review of the previously proposed studies in relation to ultrasound transducers. Chapter 3 describes the fabrication, simulation and characterization methods of three different transducer structures: single-element transducer, linear transducer array consisting of piezoelectric material and linear transducer array consisting of piezoelectric material and a passive layer using SLID and conventional epoxy bonding method. Chapter 4 shows the fundamental results of each transducer structures such as acoustic pulse-echo, variation in electrical impedances in the fabricated structures. The reasons and explanations of these discrepancies are also included. Chapter 5 discusses the above results in depth and some important recommendations and implications are pointed out. In chapter 6, the most valuable results are summarized and concluded upon. In addition, an outlook for future works is also given.

# CHAPTER 2. Theoretical Background

## 2.1 Design considerations of the ultrasonic transducer

### 2.1.1 Basic principles

A schematic of a typical piezoelectric transducer is shown in Figure 2.1. The operation of ultrasonic transducers bases on converse and direct piezoelectric effect of piezoelectric materials in which the applied voltage across the electrodes generates the vibration. The electrical signal would be generated when receiving an echo. Therefore, piezoelectric material is one of the most important elements in transducer technology. For each particular application, piezoelectric materials are selected based on many factors such as acoustic impedance (the product of material density and longitudinal wave velocity), dielectric properties, elastic properties, piezoelectric performance and stability.

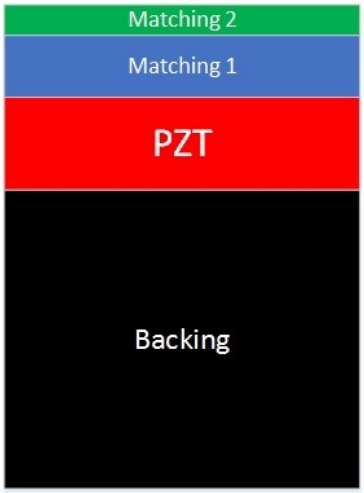


*Figure 2.1: A schematic of a typical piezoelectric transducer*

A transducer rings at its natural frequency once it is excited by an electrical source. Because the piezoelectric material has much higher acoustic impedance (~33 MRayls) than that of biological tissue or water (~1.5 MRayls), reverberation of acoustic waves will produce the so-called ringing effect for pulse-echo applications, resulting in poor axial resolution and sensitivity. Therefore, the performance of a transducer can be improved by adding layers to the front and back of an active layer. The first one is known as matching layer in the front for improving the energy transmission between the active layer and load medium. Backing layer supports the active element and minimizes ultrasound energy reflected from the backing layer, thus damping out the reverberation. The criteria of these mechanical layers are presented in the next section.

Pressure waves generated when a single electrical pulse is applied across the active element move in the front and back directions. The pressure wave moves forward to the front surface of the piezoelectric material. The transmission coefficient of this pressure at a normal incidence is calculated as follows:

$$T = \frac{2Z_l}{Z_p + Z_l} \tag{2.1}$$

where $Z_l$ and $Z_p$ are acoustic impedance of the loading medium and piezoelectric material, respectively. If a piezoelectric layer ($Z_p \sim 33$ MRayls) is in direct contact with the body medium ($Z_l \sim 1.5$ MRayls), only 10% energy is transmitted from the active layer to the load. To avoid this mismatch, a matching layer will be inserted between piezoelectric layer and load medium. Using transmission line theory [6], 100% transmission between piezoelectric layer and load occurs as the thickness of the matching layer is close to of $\lambda_m/4$ ($\lambda_m$ is wavelength in the matching layer) and acoustic impedance $Z_m$ [6], where:

$$Z_m = (Z_p Z_l)^{1/2} \tag{2.2}$$

For wideband transducers, Desilets, et al. [7] showed that the optimum impedance of single matching layer should be modified to:

$$Z_m = (Z_p {Z_l}^2)^{1/3} \tag{2.3}$$

And for transducers with two matching layers, the acoustic impedances of these two layers should be:

$$Z_m = ({Z_p}^4 {Z_l}^3)^{1/7} \tag{2.4}$$

$$Z_m = (Z_p {Z_l}^6)^{1/7} \tag{2.5}$$

Similarly, the pressure wave moves backward and reaches the rear surface of piezoelectric element at a normal incidence. A fraction of energy will be transmitted into the air and the rest is reflected back. The reflection coefficient is calculated as follows:

$$R = \frac{Z_a - Z_p}{Z_a + Z_p} \tag{2.6}$$

where $Z_a$ is the acoustic impedance of air. Large amount of energy will be reflected and reverberate inside the piezoelectric element, creating a long ring down (narrow bandwidth). Therefore, backing layer is used to damp out the ringing due to acoustic impedance

mismatch between the air and piezoelectric materials. Theoretically, when the acoustic impedance of the backing $Z_b$ is equal to that of piezoelectric element $Z_p$, R = 0 and the sensitivity will be significantly decreased. Therefore, a trade-off between bandwidth and sensitivity must be considered depending on specific applications.

To maximize energy transmission, the transducer input impedance should be real and the input resistance should match the electrical impedance of the source (normally 50 Ω). The reactive part of impedance could be tuned out by adding an inductor either in series or in parallel with the transducer [7], [8].

### 2.1.2 Losses in Piezoelectric Materials

In general, there are three kinds of losses in piezoelectric materials: mechanical, dielectric and electromechanical losses. In frequency domain, these losses can be taken into account by replacing elastic, dielectric and electromechanical coupling coefficient constants with their complex values [9]. In other words, the mechanical, dielectric and electromechanical losses are taken into account by using complex elastic constant ${c_{33}}^{E*}$, complex dielectric constant ${\varepsilon_{33}}^{E*}$ and complex electromechanical coupling coefficient ${k_t}^*$, respectively. These complex constants can be written as:

$${c_{33}}^{E*} = c_r + jc_i = {c_{33}}^E(1 + j\delta_m) \tag{2.7}$$

$${\varepsilon_{33}}^{S*} = \varepsilon_r - j\varepsilon_i = {\varepsilon_{33}}^S(1 - j\delta_e) \tag{2.8}$$

$${k_t}^* = k_{tr} + jk_{ti} = k_t(1 + j\delta_k) \tag{2.9}$$

where the subscripts r and j stand for real and imaginary terms. $\delta_m, \delta_e$ , $\delta_k$ are the mechanical, dielectric and electromechanical losses, respectively.

## 2.2 Ultrasonic transducer types

Ultrasonic transducers are designed in various forms and sizes depending on their specific applications. They range from single-element transducers with mechanical scanning, to linear arrays and multi-dimensional arrays with electronic scanning.

### 2.1.1 Single-element transducers

Single-element transducers are the simplest ultrasonic transducers that have only one active element. A single-element transducer can be translated or steered mechanically to form an image. In general, the single-element transducers can be classified as plane and focused for specific applications (Figure 2.2) [10]. Because the plane configuration limits

the lateral resolution and sound intensity, focusing is utilized to improve the lateral resolution and performance in high resolution imaging applications. Although focused transducers generate higher resolution images, plane transducer elements are commonly utilized for some applications requiring miniature transducer, such as intravascular imaging [11].

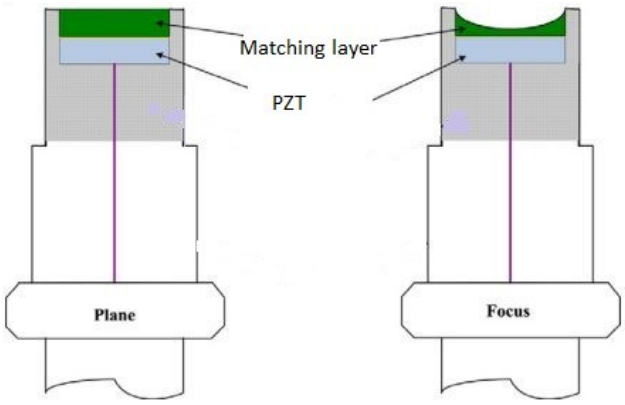


*Figure 2.2: Schematic of (a) plane and (b) focused transducer*

In this thesis, two plane single-element transducers using different matching layer materials will be fabricated and characterized.

### 2.1.2 Transducer Arrays

Arrays transducers involve more than one element. These elements may be rectangular-shaped and arranged in a line (called one-dimensional (1D) array); square in shape and arranged in rows and columns (called two-dimensional (2D) array); or ring shaped and arranged concentrically (called annular array). The schematic diagram of a 1D transducer array is shown in Figure 2.3 [12]. Compared to the single-element transducers, transducer arrays have been widely utilized in many clinical applications due to their clinical convenience, increased frame rates and the capability to focus the beam dynamically [13]. A 1D array is operated by applying successively voltage pulses to groups of elements. The sound beam is moved across the face of the transducer electronically, producing an image similar to the case obtained by scanning a single transducer mechanically [14].

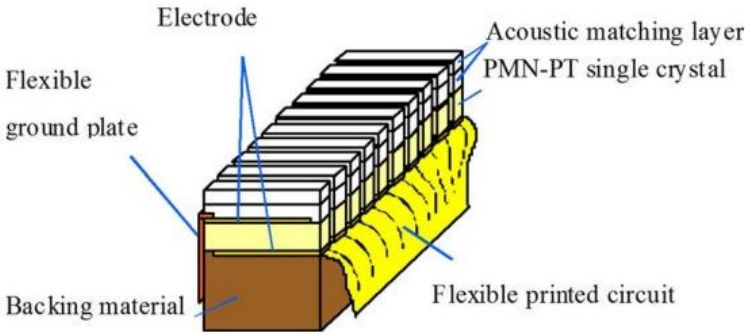


*Figure 2.3: Schematic diagram of a linear array transducer*

Deviations of the individual elements from their ideal state (single mode with no cross-coupling) will have important effects on the performance of the one-dimensional transducer array. Therefore, our thesis focuses on the fabrication and characterization of variation across array elements in transducer arrays.

## 2.3 SLID (Solid-Liquid Interdiffusion) bonding method

SLID bonding has been considered as a promising bonding technique, particularly for high-temperature applications. The SLID is based on formation of intermetallic compounds (IMCs) as the bonding medium, allowing a thermal stability at temperatures higher than the bonding temperature [15]. The SLID bonding method is based on two metal components, one metal has lower melting temperature (Sn, In) than the other (Au, Cu, Ag, Ni). At a temperature above lower melting point, the low melting metal component melts and IMCs solidify. The chemical reaction is set to thermal equilibrium condition and a bond line is comprised of the high melting component and IMCs with elevated melting temperatures. SLID bonding involves multiple metal systems such as Ag-In, Au-Sn, Cu-Sn. This technology has drawn much attention in recent research activities due to several advantages:

High temperature stability: the final bond line consisting of IMCs and high melting metal with high temperature stability allows repeating processing without bond melting [16].

High bond performance: Metals are used as intermediate layers, which enable high bond strength.

An gold-tin (Au-Sn) SLID interconnect technology has been developed at IMST, HSN to bond piezoelectric material to tungsten carbide (WC) passive layer. Successfully bonded

samples were then diced to form 1D arrays. Electrical impedance of the array elements was measured to assess variation across these elements.

## 2.4 Linear Transducer Array using SLID bonding method

Typically, a piezoelectric ultrasound transducer has a piezoelectric active layer with thickness of half of a resonant wavelength. A problem with this type of transducer is the perturbation from the back of the acoustical stack, such as parasitic reflections and radiation losses. In addition, this thickness requires use of high drive voltages to obtain the desired acoustic pressure because the thicker the piezoelectric material, the higher the applied voltage required to achieve the same electric field across the piezoelectric material. To solve this problem, a novel configuration was introduced by J.F. Gelly [17]. A quarter wavelength thickness ($\lambda/4$) piezoelectric material is coupled with a high impedance ($Z \sim$ 100 MRayl) material that is placed at the rear part of the piezoelectric layer. This high impedance layer is named as the dematching layer (DML). With this arrangement, transducers operate at lower voltage than those used in the conventional way while still provide the desired acoustic pressures. In addition, mismatch in acoustic impedances between the DML and the piezoelectric layer prevents acoustic energy from propagating into backing. Therefore, the amount of energy lost to the backing is less than that in the conventional half wave resonance configuration and more energy can be transferred toward the human body [18]. Typically, this arrangement decreases insertion losses around 1 to 3dB [17].

In the quarter wavelength thickness resonating configuration, the piezoelectric material and dematching layer are bonded together with an assembly material to form an acoustical connection. Adhesive such as epoxies, e.g. Epo-Tek 301 [13] have widely been used as bonding materials. However, SLID bonding method is utilized in this thesis. This method produces a bond line with acoustic impedance better matched to the impedances of the substrates. Hence the requirements on both bondline thickness and uniformity are potentially relaxed.

## 2.5 Modeling of piezoelectric ultrasound transducers

Modeling plays an important role in the development of a new transducer. A reliable model provides prior prediction of a transducer behavior and its performance. New transducers can be designed and optimized before moving to the fabrication steps based on

modeling. In this thesis, modeling of the transducers consists of (1D) model and FEM simulation.

### 2.5.1 One-dimensional model

In many cases, a 1D equivalent circuit model is sufficient to describe the thickness vibration mode of a piezoelectric transducer. There are several existing models, but the most commonly used are Mason[19], Redwood [20] and Krimholtz, Leedom and Matthaei (KLM) [21] models. In this thesis, Mason-based program named X-trans is used. This program was developed at the Department of Circulation and Medical Imaging, NTNU and has been widely used as an internal simulation tool by ultrasound group at HSN. The equivalent circuit of Masons' model of a piezoelectric element is shown in Figure 2.4.

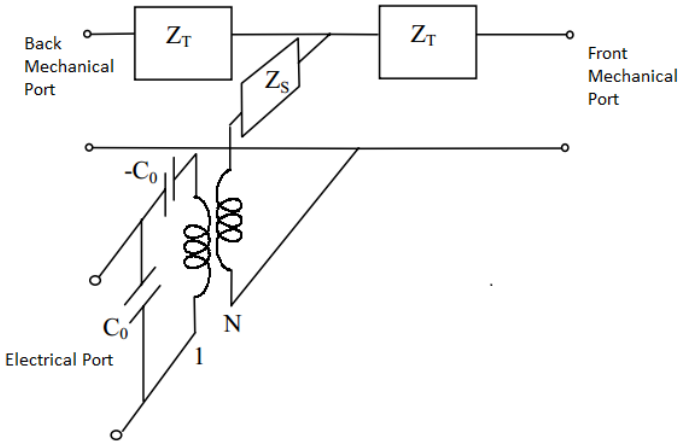


*Figure 2.4: Three port Mason's model of a piezoelectric layer*

The relationship between the constants of the Mason's equivalent circuits are shown as follows.

$$
\begin{aligned}
C_0 &= \varepsilon_{33}{}^S A/t^{PZT} \\
Z^T &= jZ^{PZT}\tan\left(k_3{}^{PZT}\, t^{PZT}\right)/2, \\
Z^S &= -jZ^{PZT}/\sin(k_3{}^{PZT} t^{PZT})/2, \\
h_{33} &= e_{33}/\varepsilon_{33}{}^S \\
N &= C_0 h_{33}
\end{aligned}
\tag{2.10}
$$

where $Z^{PZT} = \rho^{PZT} V^{PZT}$ is the characteristic impedance, $\rho^{PZT}$ is the density and $V^{PZT}$ is the longitudinal velocity, $k_3{}^{PZT} = \omega/V^{PZT} = 2\pi f/V^{PZT}$ is the wave number in the thickness direction of the piezoelectric element; $e_{33}$, $\varepsilon_{33}{}^S$ are the coupling coefficient and

relative dielectric constant in the thickness direction; $t^{PZT}$, A are thickness and area of the piezoelectric element.

The circuit has three ports, one electrical and two mechanical ports representing the front and back faces of the piezoelectric element. The front matching layers and backing layer can be cascaded to model the entire transducer. The matching layers can be represented by two port acoustic system.

### 2.5.2 Finite Element Method simulations

FEM is a general simulation technique to approximately solve partial differential equations in physics, mechanics, chemistry, or biology problems. It has been used to model a transducer's behavior, especially when simple 1D model is not able to predict the performance of the transducer. With this technique, the piezoelectric transducer and its surrounding medium are divided into a one, two or three-dimensional mesh of elements. The electric potential and elastic vibrations are computed from finite element matrix equations [22]. The finite element equations are solved at each node in the mesh and at frequency range. The simulation results are not absolute exact because the transducer structure is approximated by a mesh of discrete elements. To obtain more accurate results, the element size should be small compared to the wavelength of sound. In addition, one should have accurate material data and good understanding of the physics behind the FEM model.

The constitutive equations for a piezoelectric material are given by:

$$T = [c^E]\, S - [e]^t\, E \tag{2.10}$$

$$D = [e]\, S + [\varepsilon^S]\, E \tag{2.11}$$

In 3D case, T is the 6x1 stress vector, c is 6x6 the elasticity matrix, S is the 6x1 strain vector, e is the 3x6 piezoelectric matrix, E is the 3x1 electric field vector, D is the 3x1 electric displacement vector, and ε is the 3x3 dielectric permittivity matrix, $[e]^t$ is the transpose of $[e]$. The superscripts *E*, *S* indicates a zero or constant corresponding field. For example:

$$[c^E] = \begin{bmatrix} c_{11}^E & c_{12}^E & c_{13}^E & c_{14}^E & c_{15}^E & c_{16}^E \\ c_{21}^E & c_{22}^E & c_{23}^E & c_{24}^E & c_{25}^E & c_{26}^E \\ c_{31}^E & c_{32}^E & c_{33}^E & c_{34}^E & c_{35}^E & c_{36}^E \\ c_{41}^E & c_{42}^E & c_{43}^E & c_{44}^E & c_{45}^E & c_{46}^E \\ c_{51}^E & c_{52}^E & c_{53}^E & c_{54}^E & c_{55}^E & c_{56}^E \\ c_{61}^E & c_{62}^E & c_{63}^E & c_{64}^E & c_{65}^E & c_{66}^E \end{bmatrix}$$

When these matrices are provided in a modeling configuration, COMSOL recognizes which equations to be applied to each specific domain in FEM models.

# CHAPTER 3. Methods

This chapter is organized as follows. Section 3.1 describes the design, fabrication and characterization of single element transducers using two diffrent matching materials. Section 3.2 presents fabrication, simulations and characterization of (1D) linear transducer array consisting of only piezoelectric material. COMSOL models used to simulate electrical impedance variance across the array are also proposed. Section 3.3 describes fabrication of a (1D) linear transducer array consisting of piezoelectric material and a back substrate using two different bonding methods. Simulation and characterization steps are also addressed in this part.

## 3.1 Single Element Transducers

### 3.1.1 Design consideration and fabrication of the single-element transducers

Two single-element transducers using two different matching layer materials were fabricated. Piezoceramic Pz27 disks (FerroPerm A/S) with the dimension of 10 mm (diameter) and 0.5 mm (thickness) were used in this experiment.

To further enhance the bandwidth and sensitivity of the transducer, a single matching layer was employed. From equations (2.2) and (2.3), the acoustic impedance values were 7.17 MRayls and 4.25 MRayls. With the available materials in our lab, Eccosorb MF114 with 6.51 MRayls and Eccosorb MF112 with 4.94 MRayls, respectively were chosen. For maximum power transmission into the medium, the thickness of the matching layer was approximately $\lambda/4$ at the resonance frequency. The specific properties of matching layers MF112 and MF114 are listed in Table 3.1.

*Table 3.1: Properties of 2 matching layers used in single-element transducers*

| Parameters | Eccosorb MF112 | Eccosorb MF114 |
|---|---|---|
| Longitudinal velocity (m/s) | 2389 | 2246 |
| Shear velocity (m/s) | 1170 | 1145.60 |
| Density (kg/m$^3$) | 2066 | 2900 |
| Acoustic impedance (MRayls) | 4.94 | 6.51 |
| Attenuation_long (dB/cm/MHz) | 17.3 | 13.1 |
| Attenuation_shear (dB/cm/MHz) | | 46 |

The material MF112 and MF114 were ground down and polished to the desired thickness as the matching layers. The actual thicknesses of MF112 and MF114 matching

layers measured by Heidenhain-Metro length gauges were 161±5 μm and 136±2 μm, respectively. A margin of 0.4 mm was left on surface of the pz27 disks for connection of the core wires and ground wires. For each transducer, the fabrication process can be described as follows: A Pz27 disc and a matching layer were cleaned and baked at $60^0$C in oven for 3 hours. They were bonded together by an epoxy (DP460, 3M, Scotch-Weld, Epoxy Adhesive) under an external pressure to ensure a thin bondline. Degas process was performed in 3 minutes to sufficiently remove air bubble inside the epoxy. The multilayer stack was cured at $60^0$C for 8 hours. The core and ground wires were soldered for electrical connection. The bonded samples were inserted into a polypropylene tube. The transducers were then assembled into a BNC connector for further experiments. Transducer using MF112 as matching layer was named Type I and transducer using MF114 as matching layer was named Type II for clarification.

### 3.1.2 Transducer Simulations

The piezo disk transducer's model was build using COMSOL Multiphysics acoustic-piezoelectric interaction module in the frequency domain. This model was investigated in 2D axisymmetric model to save simulation time. A COMSOL model is showed in detail in Figure 3.1. All these materials were modeled as isotropic elastic materials, except for piezoelectric material. An electrical potential difference was applied to the top and bottom sides of the piezoelectric material to specify the electrical boundary condition. Mesh on all domains was chosen as free triangular with segment length less than approximately $\lambda/5$ to achieve acceptable compromise between accurate result and simulation time. To reduce the number of complete FEM nodes, the acoustic domain (i.e. water) was reduced to a small region surrounded by Perfectly Matched Layer (PML), which simulates the zero reflection condition.

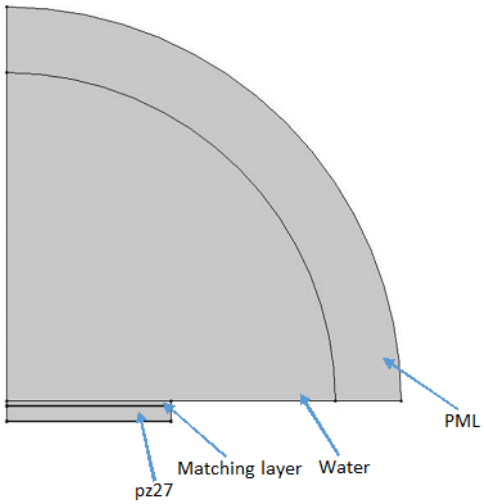


*Figure 3.1: COMSOL Model for single element transducers*

### 3.1.3 Transducer characterization

To evaluate the performance of the fabricated transducers, a set of measurement was performed. Electrical impedances of the transducers were measured by a network analyser HP8753D (Agilent Technologies Inc.Philadelphia, PA) with water load. The center frequency, bandwidth, sensitivity of the transducer were investigated using a pulse-echo response arrangement. Each transducer mounted in a water tank in front of a thick stainless and polished steel target, which was 6 mm away from the transducer's surface. The reflected waveforms were received by a LeCroy LT342 Waverunner oscilloscope (Teledyne LeCroy, Chestnut Ridge, NY) with a 1 MΩ coupling impedance. The cable length between the transducer and function generator was 1.5 m and that between the function generator and oscilloscope was 25 cm. The pulses were acquired in LabVIEW, saved and imported to Matlab, where the spectra were calculated. The bandwidth of each transducer was determined from the frequency spectrum of the first echo. The following parameters were calculated from the measured frequency spectrum:

(a) Lower and upper -6dB frequencies ($f_l$ and $f_u$) the frequencies at which the magnitude of the spectrum decreases by 6dB from its maximum.

(b) Center frequency

$$f_c = \frac{f_l + f_u}{2} \tag{3.1}$$

(c) -6 dB bandwidth

$$\text{BW} = \frac{f_u - f_l}{f_c} X\ 100\% \tag{3.2}$$

(d) Transducer Sensitivity: is defined as the ability of the transducer to detect reflected

ultrasound / generate an electrical signal. In this thesis, we only calculated the transmitting sensitivity as the ratio between output velocity at the radiating surface to the input current.

## 3.2 One-Dimensional Linear Array Ultrasonic Transducer

### 3.2.1 Flex Circuit Fabrication

a. Initial Flex Sample: The flex circuit consists of 26 µm-thick Polyimide layer sandwiched between two 9µm-thick Copper layers as shown in Figure 3.2.

*Figure 3.2: Cross section of a flex plate*

b. Mask design for the flexible circuit is shown in Figure 3.3.

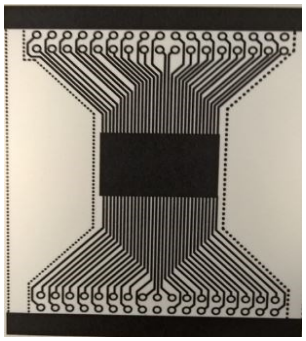

*Figure 3.3: Mask design for flex circuit*

c. Fabrication Steps:

Figure 3.4 shows the fabrication process to form a patterned flexible circuit. Firstly, a rectangular unpatterned flex plate and a silicon wafer were cleaned to remove contamination on the wafer and flex plate surface (Figure 3.4a). The flex sample was glued onto the wafer using double-side tape (3M-Scotch). The entire sample was then baked at $110^0$C for 2 minutes to remove the solvent. Positive Photoresist S1813 (Microchem) was spin-coated on the flex surface with parameters 60s (time)-2500 rpm (speed)-800 rpm/s (acceleration) (Figure 3.4b). After spin coating, the photoresist was soft-baked on a hot plate at $110^0$C for 2 minutes. Then, the mask pattern was transferred to the photoresist by alignment and exposure under ultraviolet (UV) light using Mask Aligner, Karl Suss MA56 (Figure 3.4c). The developing process was performed using MF-319 developer solution (Microchem) (Figure 3.4d). The whole sample was hard baked at $110^0$C for 2 minutes. The flex sample was taken away of the wafer and the copper layers on both sides were etched

using $Na_2S_2O_8$ solution at $40^0$C for 2 minutes (Figure 3.4e). Remaining photoresist was stripped by using Acetone, Isopropanol and DI water (Figure 3.4f).

### 3.2.2 Linear transducer array fabrication

Rectangular 8x20 $mm^2$ Pz27 samples were used in the present work. A Pz27 sample and flexible circuit were cleaned and baked at $60^0$C in oven for 3 hours. This sample was then bonded to the flexible circuit by DP460 epoxy, a bonding material used to stack up components. Degas process was performed in 3 minutes to sufficiently remove air bubble inside the epoxy because air bubble might prevent the ultrasound beam from transmitting into the medium. Applying an external pressure to make the bonding thickness as thin and flat as possible. Curing the epoxy in the oven at $60^0$C for 3h was performed.

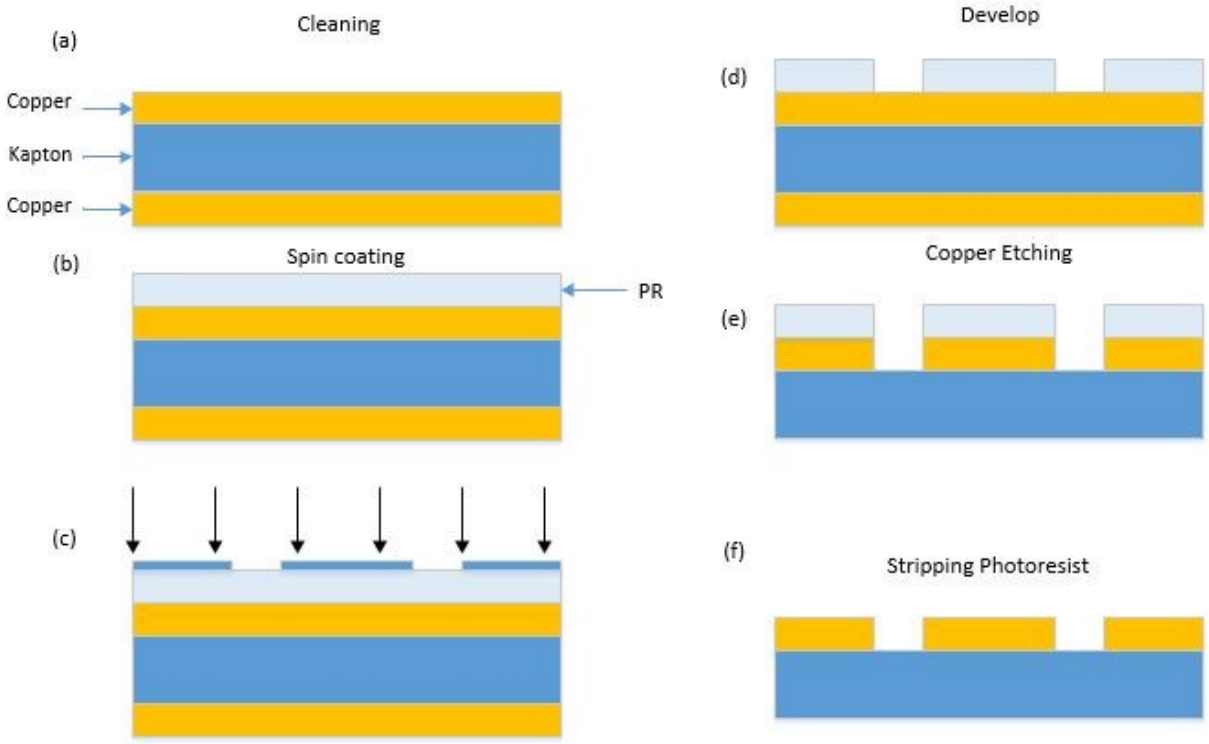


*Figure 3.4: Fabrication process for flexible circuit*

The next step was consequently to dice the sample into elements as shown in Figure 3.5. Diamond blade (Z09-SD1700-Y1-60 53.4x0.033ASx40) was used. Dicing was performed by using a DAD 321 dicing saw (Disco Corp., Tokyo, Japan).

**Dicing Parameters:**

- Dicing blade:0.033 mm thickness
- Feeding speed: 1mm/s.

- Dicing height: 0.1 mm from the chuck.
- Pitch: 300 µm

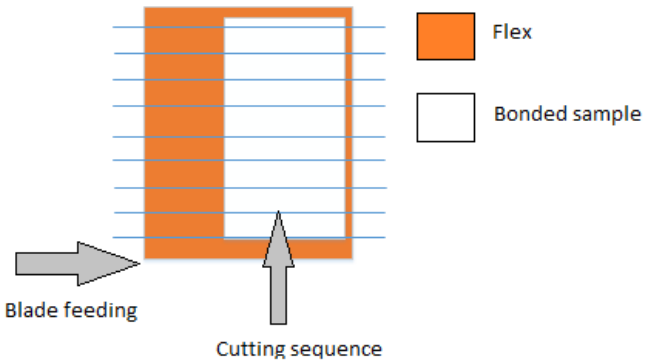


*Figure 3.5: Dicing Direction*

For the purpose of investigating the variation in the array, we diced the sample with different blade revolution speeds. A total of 53 elements was acquired. The blade speeds applied for the array were listed in Table 3.2.

*Table 3.2: Dicing conditions applied to the array*

| Blade speed (rpm) | 10000 | 30000 | 25000 | 20000 | 15000 |
|---|---|---|---|---|---|
| Element No | 1-13 | 14-24 | 25-36 | 37-43 | 44-53 |

### 3.2.3 Array Element Characterization

The linear array's impedances were measured with the Network Analyser HP8753D. The variance of resonance and anti-resonance at each vibrational mode can be calculated as follows:

$$\% \text{ variance at resonance} = \frac{f_{r\_max} - f_{r\_min}}{f_{r\_max}} \tag{3.3}$$

where $f_{r\_max}$, $f_{r\_min}$ are the maximum and minimum resonance frequencies among array elements at each mode.

$$\% \text{ variance at anti-resonance} = \frac{f_{a\_max} - f_{a\_min}}{f_{a\_max}} \tag{3.4}$$

where $f_{a\_max}$, $f_{a\_min}$ are the maximum and minimum anti-resonance frequencies among array elements at each mode.

The resonance frequency $f_r$ is the one at which the impedance magnitude become the minimum. The anti-resonance frequency $f_a$ is the one at which the impedance magnitude reaches the maximum.

### 3.2.4 Finite Element Model of the Array Element

#### 3.2.4.1 Find fitted material data for Pz27 in Comsol 2D Simulation

A reliable input material properties to a FEM model are important to provide a convincible result. Material data supplied by the manufacturer may not provide the most accurate model results. Therefore, we need to find the most accurate data for piezoelectric material Pz27. A testing sample 8x20mm$^2$ of Pz27 was used to find the fitted material data. Physical dimensions of the testing sample were shown in Table 3.3. 1D simulation using Xtrans and 2D using COMSOL were analyzed to obtain electrical impedance magnitude and phase plot of the testing sample. The material data used in these tests were taken from FerroPerm Piezoceramics A/S [23] and three additional sources [24],[25],[9]. Particularly, the third material dataset was taken from source 2 but with some changes in density, relative permittivity, longitudinal velocity, dielectric and loss values.

*Table 3.3: Physical dimensions of a Pz27 testing sample*

| Parameters | Physical dimension (μm) |
|---|---|
| Top Electrode | 22 |
| PZT | 484 |
| Bottom Electrode | 18 |

The detailed material datasets from FerroPerm manufacturer and three additional sources are shown in Table 3.4 and Table 3.5.

*Table 3.4: Material data for Xtrans/Mason Simulations*

| | $h_{33}(10^8)$(V/m) | $\varepsilon_{11}{}^S/\varepsilon_0$ | $Z^{PZT}$ (Mrayl) | $V^{PZT}$ (m/s) | Q |
|---|---|---|---|---|---|
| FerroPerm | 19.8 | 914 | 33.3719 | 4334 | 75 |
| Source 1 [23] | 19.69 | 920 | 33.2559 | 4318.95 | 75 |
| Source 2 [24] | 19.69 | 920.02 | 33.4796 | 4348 | 75 |
| Source 3 [25] [9] | 22.9302 | 790 | 34.8172 | 4445 | 66.67 |

The simulation results from 1D and 2D models were successively compared to mesurement result. The one that most fitted to mesurement result will be chosen as final material data for pz27 piezoelectric material.

*Table 3.5: Material data of Pz27 from Ferroperm Piezoceramics A/S and 3 other sources for COMSOL models*

| Ferroperm Piezoceramics A/S [23] | | Source 1 [24] | Source 2 [25] | Source 3 [25] [9] |
|---|---|---|---|---|
| ${c_{11}}^E(10^{10}\ \mathrm{N}/m^2)$ | 14.70 | 11.875 (1 + i/95.75) | 12.0 (1+i/110) | 12.0 (1+i/110) |
| ${c_{12}}^E(10^{10}\ \mathrm{N}/m^2)$ | 10.50 | 7.430 (1 + i/71.24) | 7.43 (1+i/250) | 7.43 (1+i/250) |
| ${c_{13}}^E(10^{10}\ \mathrm{N}/m^2)$ | 9.370 | 7.425 (1 + i/120.19) | 7.5 (1+i/200) | 7.5 (1+i/200) |
| ${c_{33}}^E(10^{10}\ \mathrm{N}/m^2)$ | 11.30 | 11.205(1+ i/177.99) | 11.4(1+i/177.99) | 12.02562(1+i*0.015) |
| ${c_{44}}^E(10^{10}\ \mathrm{N}/m^2)$ | 2.30 | 2.110 (1 + i/75) | 2.105 (1+i/75) | 2.105 (1+i/75) |
| $e_{13}$ (C/$m^2$) | -3.090 | -5.4 (1- i/166) | -5.4 (1-i/70) | -5.4 (1-i/70) |
| $e_{33}$ (C/$m^2$) | 16 | 16.0389(1-i/323.77) | 16.0389(1-i/200) | 16.0389 (1-i/200) |
| $e_{15}$ (C/$m^2$) | 11.60 | 11.20 (1- i/200) | 11.0 (1-i/200) | 11.0 (1-i/200) |
| ${\varepsilon_{11}}^S/\varepsilon_0$ | 1130 | 916 (1 -i/50) | 916.02 (1-i/50) | 916.02 (1-i/50) |
| ${\varepsilon_{33}}^S/\varepsilon_0$ | 914 | 920 (1- i/86.28) | 920.02 (1-i/80) | 790 (1-3*i/500) |
| Density (kg/m$^3$) | 7700 | 7700 | 7700 | 7720 |
| $k_t$ | 0.469 | 0.4689 | 0.4658 | 0.46 |

### 3.2.4.2 General description of COMSOL model

Finite element model (FEM) was used to anticipate array performance prior to fabrication. The relevant properties of the active and passive materials used in the COMSOL model are listed in Table 3.5 (Source 3) and Table 3.6. A 2D model was first used to generate an electrical impedance magnitude and phase plot of array element (Figure 3.6).

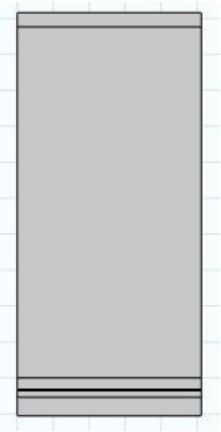

*Figure 3.6: COMSOL model used for element*

Parameters used in COMSOL simulation model are shown in Table 3.6.

*Table 3.6: Parameter values used in the Model*

| | |
|---|---|
| Piezo width (µm) | 250 |
| Piezo thickness (µm) | 490 |
| Upper electrode thickness (µm) | 18 |
| Lower electrode thickness (µm) | 18 |
| Cu thickness (µm) | 9 |
| Kapton thickness (µm) | 26 |
| Bond thickness (µm) | 2 |

FEM for the linear ultrasonic transduce array was built using COMSOL Multiphysics acoustic-piezoelectric interaction module in the frequency domain. The measured results were verified by COMSOL model under the Acoustic-Piezoelectric Interaction Physics Package with following boundary conditions: the whole structure was free, Electric potential and ground were applied to top and bottom sides of piezoelectric material. In order to visualize the vibration mode characteristics, we can check deformed shape animation at a specific frequency. Material data for pz27 array element were chosen from the result of section 3.2.4.1. The vibration was obtained by plotting displacement field.

The electrical impedance Z of a piezoelectric element can be expressed by the following formula:

$$Z = \frac{V}{I} \tag{3.5}$$

where V is the potential difference voltage across the two piezoelectric material faces and I is the current flowing inside.

The electric current flowing in the element can be calculated by the following integral:

$$I = b\int_0^d j_y dx \tag{3.6}$$

where $j_y$ is the current density component along y axis, d is the piezoelectric material width, b is the length of each element. In this case, b = 8 mm.

Optimization of mesh size was conducted. The mesh size was optimized by performing mesh with three numbers of elements, or gradually increasing the mesh density and finding a corresponding final results. The mesh illustrations of these cases are shown in Figure 3.7.

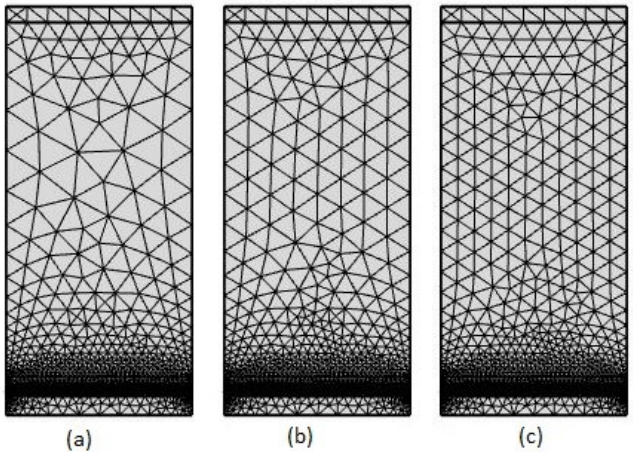


*Figure 3.7: Optimization of simulation mesh with three triangular of elements (a) 2647 (b) 2695 (c) 2811*

### 3.2.5 COMSOL models used to explain variation in electrical impedances

The measured impedances were compared and variations between elements were classified as caused by geometric differences or changes in material properties. Sources for geometric differences between the elements can be e.g. variations in element width, kerf shape, piezoelectric plate or electrode thickness. Debris inside the kerf was also observed on microscopic images. Material property changes were linked to local heating of the piezoelectric material during the dicing [26]. Contributions from these sources on the electrical impedance of each element were studied and compared to Finite Element simulations using COMSOL.

### 3.2.5.1 Geometric differences

Using the typical COMSOL model described in the above sections, models with different geometries due to variation in element width, keft shape, piezoelectric plate or electrode thickness were build to investigate the effect of each factor into electrical impedance of each element. Element width, piezoelectric plate or electrode thickness were observed under microscopic images. To verify the real kerf shape, epoxy was filled to a testing array structure. After being cured, the array structure was grinded and polished to investigate sample's cross section. Detailed description of these factors will be discussed in Result and Discussion Chapters.

### 3.2.5.2 Changes in material properties

Variation in electrical impedances was also originated from changes in material properties of piezoelectric material and debris inside the kerf. Models used to simulation these phenomenon were shown in Figure 3.8 and Figure 3.9, respectively. Result and Discussion parts will be devoted to explain comprehensively these phenomena.

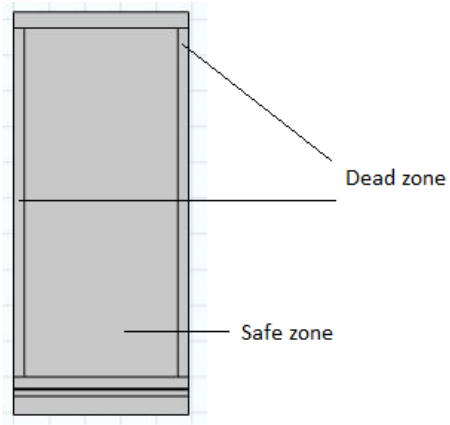


*Figure 3.8: Model used to explaiin changes in material properties*

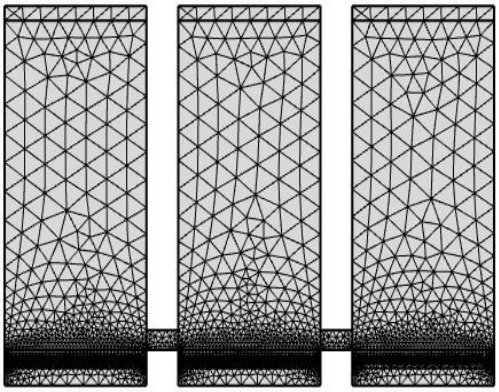

*Figure 3.9: Model used to simulate debris inside the kerfs*

## 3.3 Piezoelectric linear array ultrasonic transducer using different bonding methods

### 3.3.1 Array Module Fabrication

#### 3.3.1.1 One-Dimentional Linear Transducer Array using SLID bonding method

Initially, a 8x20mm$^2$ PZT HD3203 plate was bonded to a 8x20mm$^2$ Tungsten Carbide (WC) substrate using SLID bonding method. This bonding process was performed by postdoctoral researcher Hoang-Vu Nguyen, IMST, HSN. Successfully backed transducer was then bonded to a flexible circuit described in section 3.2.1 using a mixture of DP460 epoxy and adhesion promoter AP131 (Lord Chemical, Erie, PA). Procedures for a thin bond line was performed as thoroughly described in section 3.2.2. Figure 3.10 illustrates a completed bonded structure.

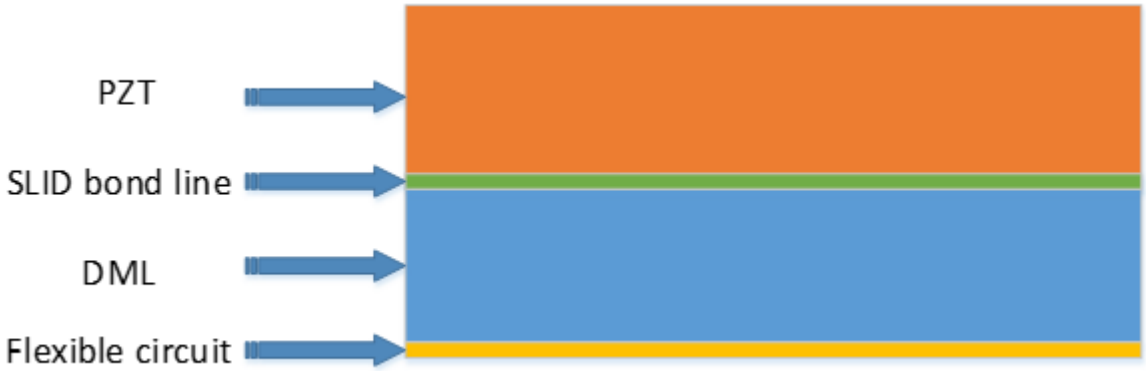


*Figure 3.10: Cross section of bonded structure in SLID bonding method*

The multilayer stack was vertically cut into 64 elements along the width direction with partial separation on the Polyimide layer (~10-µm flexible circuit layer remained uncut) as shown in Figure 3.11. Diamond blade (Z09-SD1700-Y1-60 53.4x0.033ASx40) was used in this dicing step. The element pitch was 300 µm. Feeding speed and revolution speed were set at 1mm/s and 20000 rpm, respectively.

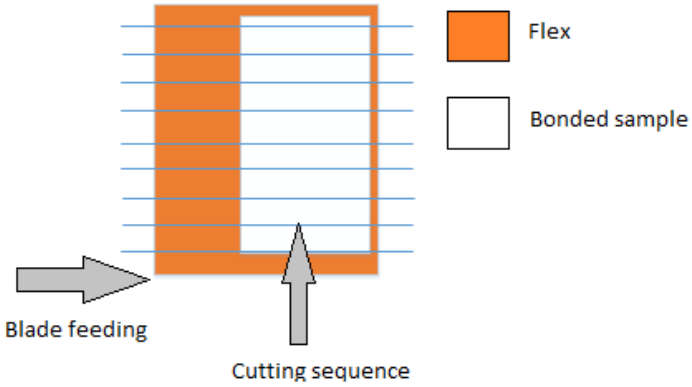


*Figure 3.11: Cutting direction into array elements*

IM4000 Ion Milling System machine was utilized to reveal cross section of the samples. Optical Microscope II Neophot 32 and Optical Microscope I Leica DM4000M were used to observe array structures.

### 3.3.1.2 One-Dimentional Linear Transducer Array using epoxy bonding method

The piezoelectric material and WC substrate used in this method are the same as described in the above section. Epoxy was used as bonding material between PZT and WC substrate instead of SLID. Figure 3.12 presents a cross section of structure prior bonding process. Figure 3.13 outlines a completed bonded structure.

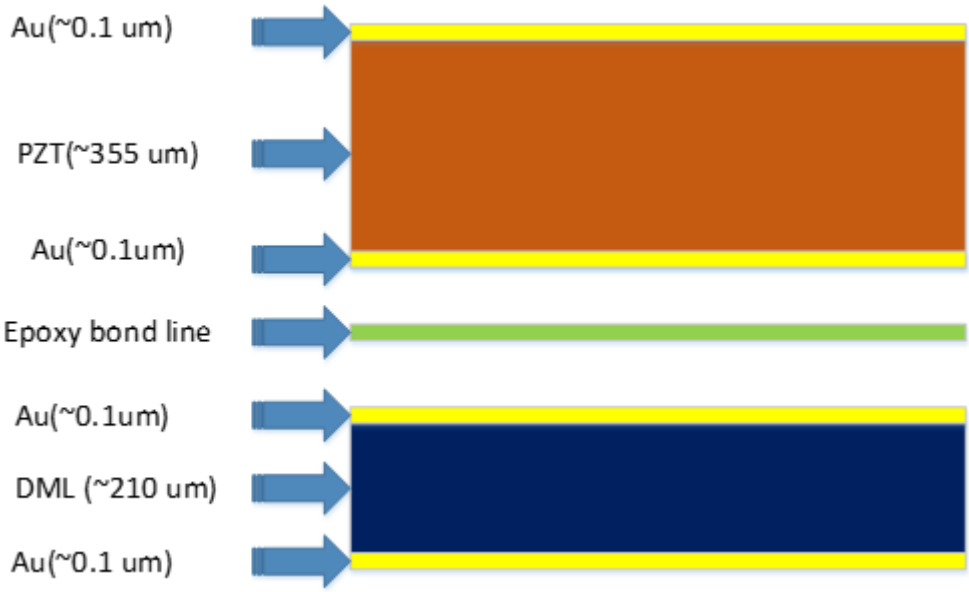


*Figure 3.12: Sample before conventional epoxy bonding method*

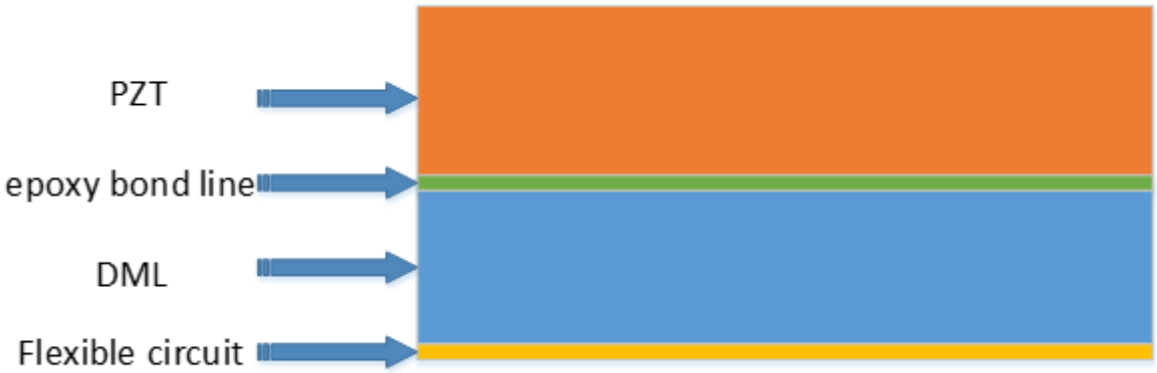


*Figure 3.13: Cross section of bonded structure in epoxy bonding method*

Diamond blade (ZH05-SD 2000-N1-EG) was used in the dicing step. The completed transducer was diced into elemment with the same parameters as described in section 3.3.1.1.

### 3.3.2 Finite Element Model of the Array Element

#### 3.3.2.1 General Description of the model using SLID bonding method

FEM was used to predict array performance prior to fabrication. The relevant properties of the active and passive materials used in the COMSOL model are listed in Table 3.7 and Table 3.8. A 2-D model was first used to generate an electrical impedance magnitude and phase plot of an array element.

*Table 3.7: Material Properties for PZT HD3203 used in COMSOL model*

| Stiffness constants | | Dielectric constants | | Stress constants | | Other properties | |
|---|---|---|---|---|---|---|---|
| $c_{11}{}^{E}$(GPa) | 141.9 | $\varepsilon_{11}{}^{S}/\varepsilon_0$ | 1513.44 | $e_{15}$ (C/m$^2$) | 14.286 | Density (kg/m$^3$) | 7850 |
| $c_{12}{}^{E}$(GPa) | 91.44 | $\varepsilon_{22}{}^{S}/\varepsilon_0$ | 1513.44 | $e_{31}$ (C/m$^2$) | -12.207 | | |
| $c_{13}{}^{E}$(GPa) | 101.3 | $\varepsilon_{33}{}^{S}/\varepsilon_0$ | 1286.72 | $e_{33}$ (C/m$^2$) | 19.249 | | |
| $c_{33}{}^{E}$(GPa) | 140.8 | | | | | | |
| $c_{44}{}^{E}$(GPa) | 25.51 | | | | | | |

*Table 3.8: Passive material properties used in COMSOL model*

| Parameters | DML | Gold | Flexible Circuit | |
|---|---|---|---|---|
| | | | Copper | Polyimide |
| Longitudinal velocity (m/s) | 6895 | 3240 | 5010 | 2400 |
| Shear velocity (m/s) | 4165 | 1200 | 2270 | 1200 |
| Density (kg/m$^3$) | 14930 | 19290 | 8930 | 1420 |
| Acoustic impedance (MRayls) | 103.94 | 62.5 | 44.7 | 3.41 |

COMSOL model (Figure 3.14) and its physical dimensions (Table 3.9) in SLID bonding method are thoroughly described in the following part.

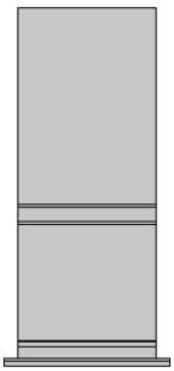

*Figure 3.14: COMSOL model of array element in SLID bonding method*

The model for the linear array ultrasonic transduce was built using COMSOL Multiphysics acoustic-piezoelectric interaction module in the frequency domain. This model is investigated in 2D. The model consisted of piezoelectric material bonded to Tungsten Carbide (WC) by SLID bonding method.

*Table 3.9: Parameter values of each layer in COMSOL model*

| Paramters | Values |
|---|---|
| PZT (µm) | 355 |
| Element width (µm) | 250 |
| Gold (µm) | 5 |
| Intermetallic layer (µm) | 26 |
| DML (µm) | 210 |
| Copper(µm) | 9 |
| Epoxy bond line (µm) | 2 |
| Polyimide (µm) | 26 |

SLID bond line included an intermetallic layer sandwiched between two surplus gold layers. Epoxy bond line and flexible circuit were also implemented in this model. All these material were modeled as isotropic elastic materials, except for piezoelectric material. A potential difference were applied to the top and bottom sides of the piezoelectric material to specify the electrical boundary condition. Because the structure was diced to polyimide layer of the flexible circuit, periodic boundary condition was applied to both sides of back Copper layer and Polyimide layer.

Similarly, the electrical impedance Z of a piezoelectric linear array can be calculated as described in section 3.2.4.2. The electrical impedance of piezoelectric element was calculated in the range from 0.10 MHz to 20 MHz with 0.025 MHz frequency step.

### 3.3.2.2 Choose optimal model to investigate variance between array elements for SLID bonding method

It has been previously reported that finite element simulation can provide an accurate prediction of array performance [27], and reduce the number of time-consuming prototype fabrication. For this linear transducer array, FEM is also used to determine the electrical impedance of array elements. The accuracy of the result is accompanied with the accurate material properties used in the model. In this case, parameters from DML, Au, piezoelectric material (PZT), flexible circuit listed in Table 3.7 and Table 3.8 are quite accurate. Unfortunately, the properties of the intermetallic compounds in SLID bond line have not been thoroughly characterized. Therefore, in order to accurately model the array elements,

a number of assumptions were made to fill in these missing material properties. A typical SLID bond line in the transducer array was shown in Figure 3.15.

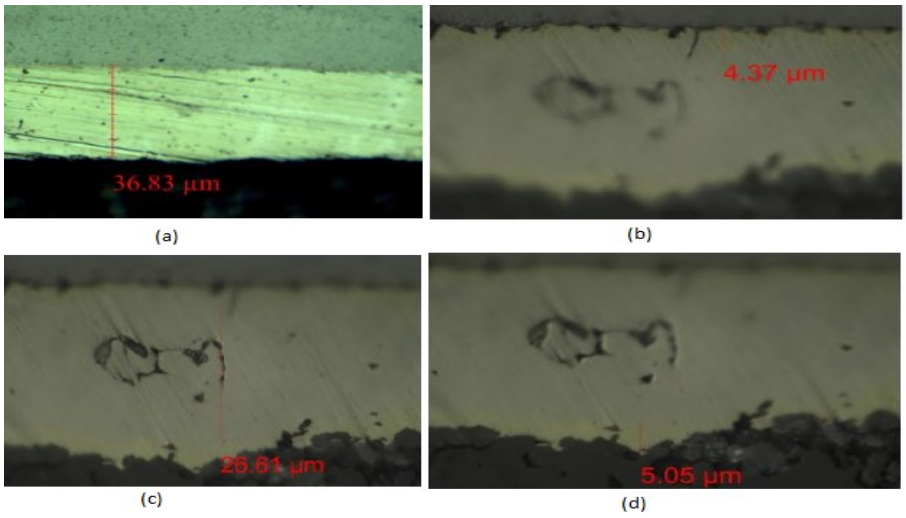


*Figure 3.15: Bond line thickness (a) Total SLID bond line (b) Upper layer Au (c) Intermetallic layer (d) Bottom layer Au*

The total bond line thickness was approximately 36 µ$m$. The upper and bottom layer were gold (Au) around 5 µ$m$ thick. Initially, ζ-AuSn, $\delta$-AuSn and ζ'-AuSn phase were assumed to be the intermetallic layer. Material parameters of these phases are listed in Table 3.10. An approximate density of intermetallic compounds AuSn 17503 kg/m$^3$ was calculated based upon EDS (Energy-dispersive X-ray Spectroscopy) analysis result from Scanning Electron Microscopy SU3500 SEM Hitachi. A Poisson's ratio of 0.2 was assumed for ζ-AuSn phase. Other material properties ( E, G) were kept the same.

*Table 3.10: Properties of the intnermetallic layer in the SLID model*

| Parameter | ζ-AuSn [28] | $\delta$-AuSn [28] | ζ'-AuSn [28] |
|---|---|---|---|
| Young's modulus, E (GPa) | 58 | 70 | 62 |
| Shear modulus, G (GPa) | 20 | 25 | 22 |
| Poisson's ratio, v | 0.2 | 0.3 | 0.4 |
| Density, ρ( kg/m$^3$) | 17503 | 17503 | 17503 |

Electrical impedance of an element with three different properties of the intermetallic layer was shown in the Result Chapter. The most well fitted simulation result will be chosen for conducting all other simulation results.

### 3.3.2.3 Mesh optimization of the model in SLID bonding method

The mesh size was optimized by performing mesh with three numbers of elements, or gradually increasing the mesh density and finding a corresponding final results. The mesh illustrations of these cases are shown in Figure 3.16.

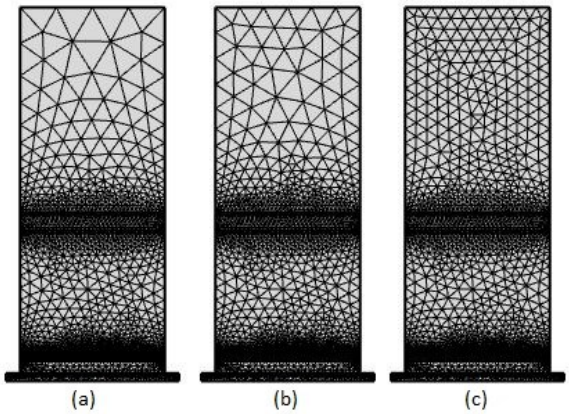


*Figure 3.16: Optimization of simulation mesh with 3 trianguar of elements (a) 4418 elements (b) 4476 elements (c) 4667 elements*

### 3.3.2.4 General Description of the model using Epoxy bonding method

The relevant properties of the active and passive materials, mesh optimization process, boundary conditions applied in model for epoxy bonding method was the same as described for SLID bonding method. However, the SLID bond line was replaced by Epoxy bond line.

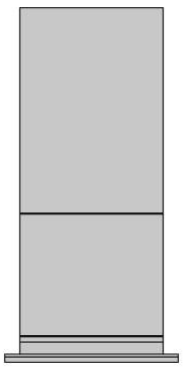

*Figure 3.17: COMSOL model of array element in epoxy bonding method*

### 3.3.2.5 Mesh optimization of the model in Epoxy bonding method

The mesh optimization was performed similarly to section 3.3.2.3. The mesh illustrations of these cases are shown in Figure 3.18.

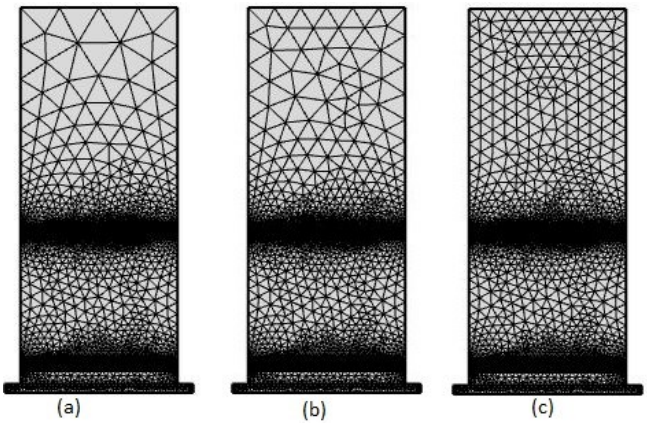


*Figure 3.18: Optimization of simulation mesh with 3 different cases*

### 3.3.3 Array Element Characterization

#### 3.3.3.1 Electrical impedance characterization for SLID bonding method

Three fabricated arrays were characterized and a typical one was presented in the result section. To evaluate transducer's performance, electrical impedance characterization was performed. The electrical impedance of the array elements was measured using the Network Analyzer HP8753D in the range from 0.10 MHz to 20 MHz with a frequency step of 0.025 MHz. Electrical probes made direct contact to each array elements. The variance of resonance and anti-resonance at each vibrational mode can be calculated in equations (3.3) (3.4).

When we want to compare two different datasets with different means and determine which one is more spread out, coefficient of variation is used:

$$\mathrm{CV} = \frac{Standard\ deviation}{Mean} \tag{3.7}$$

where CV: coefficient of variation

#### 3.3.3.2 Characterization of electrical impedance variance for SLID bonding method

The measured impedances were compared and variations between elements were classified due to geometric differences and material properties in the SLID bond line. Sources for geometric differences between the elements can be e.g. variations in element width, piezoelectric and SLID bond line thickness. Voids inside SLID bond line also primary reason causing variation between elements. Each factor generating electrical impedance variation was measured at many elements. Average and standard deviation values were reported in Result sections.

The array elements were investigated by cross-section microscopy. To investigate voids inside SLID bondline, some elements were moulded, grinded, polished and Ar ion milled to reveal cross-sectioned bondframes. The cross-sections were investigated with optical microscopy. To determine void fraction to total intermetallic layer, the cross-section micrographs were analyzed with image processing software (ImageJ). The total void area can be calculated by this software. Voids with different fractions compared to original bond line were inserted into the model and electrical impedance curve for each case were plotted, assuming other parameters were kept the same. Contributions from these sources on the electrical impedance of each element were studied and compared to Finite Element simulations using COMSOL.

The variance of resonance and anti-resonance at each vibrational mode due to each source can be calculated as follows:

$$\% \text{ variance at resonance} = \frac{f_{r\_max} - f_{r\_min}}{f_{r\_max}} \tag{3.8}$$

where $f_{r\_max}$, $f_{r\_min}$ are the maximum and minimum resonance frequencies among simulation cases being investigated.

$$\% \text{ variance at anti-resonance} = \frac{f_{a\_max} - f_{a\_min}}{f_{a\_max}} \tag{3.9}$$

where $f_{a\_max}$, $f_{a\_min}$ are the maximum and minimum anti-resonance frequencies among simulation cases being investigated.

#### 3.3.3.3 Electrical impedance characterization for Epoxy bonding method

Electrical impedance characterization was performed similarly as described in SLID bonding method. The percent of variance of electrical impedance was also calculated using equations (3.3), (3.4).

#### 3.3.3.4 Characterization of electrical impedance variance for Epoxy bonding method

The measured impedances were also compared and variances between elements were identified mainly due to geometric differences such as element width and piezoelectric thickness. These sources of variation were also investigated and compared to COMSOL simulations. Equations (3.8) and (3.9) were also used to calculate percent of variation among simulation cases being studied.

# CHAPTER 4. Results

This chapter is organized as follows. Section 4.1 describes the pulse-echo test, simulation and measurement results of electrical impedance test of single-element transducers. Section 4.2 presents the most suitable material data for pz27 and electrical characterization of the (1D) linear transducer array consisting of only a piezoelectric layer. Parameters that creates variance in electrical impedance across the array are investigated in depth. Section 4.3 describes the electrical impedance characterization of (1D) linear transducer array consisting of piezoelectric material and a back substrate using two bonding methods. Parameters causing electrical impedance variation across the arrays are presented. Finally, a comprehensive comparison between SLID and conventional epoxy bonding method is given.

## 4.1 Single Element Transducers

The fabricated single-element transducers are shown in Figure 4.1. Type I included a piezoelectric material and a front matching layer MF112. Type II consisted of a piezoelectric material and a front matching layer MF114.

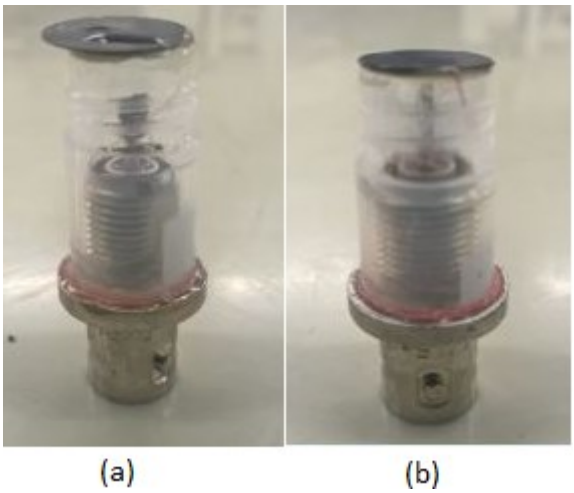


*Figure 4.1: Fabricated single-element transducers: (a) Type I (b) Type II*

### 4.1.1 Electrical impedance test

Figure 4.2 and Figure 4.3 show the measured and modeled electrical impedances of two single-element transducers. For transducer (Type I), the magnitude and the phase angle of the electrical impedance were 22 Ohm and $-53^0$ at the center frequency of 3.90 MHz. For transducer (Type 2), the magnitude and the phase angle of the electrical impedance were 33.5 Ohm and $-63^0$ at the center frequency of 4.06 MHz.

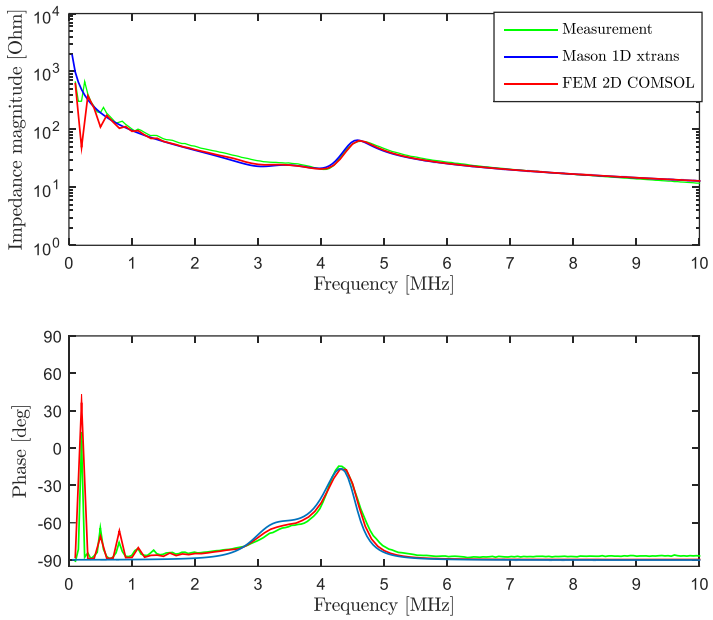


*Figure 4.2: Measured and modeled electrical impedance of transducer Type I*

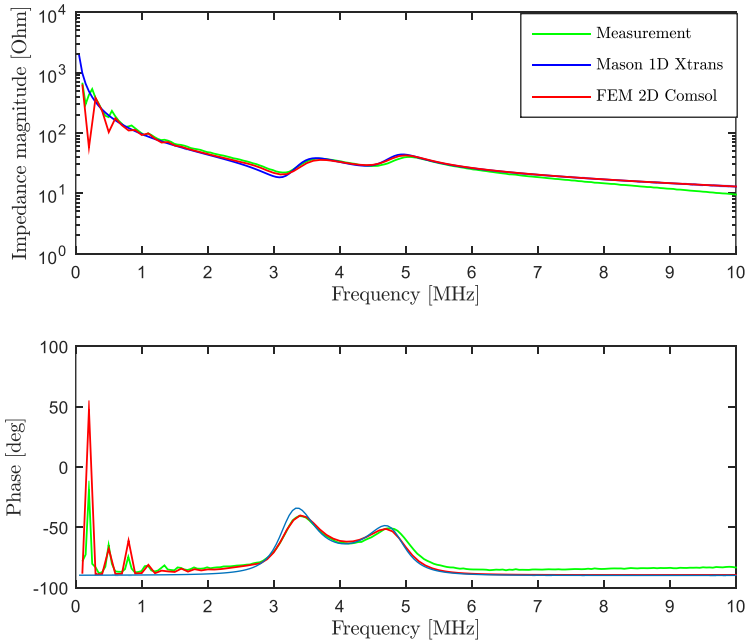


*Figure 4.3: Measured and modeled electrical impedance of transducer Type II*

### 4.1.2 Pulse echo test

The measured pulse-echo response response of two single-element transducers were shown in Figure 4.4 and Figure 4.5. The frequency response was quantified by the center frequency and the -6dB fraction bandwidth of the spectrum. For transducer (Type I) as shown in Figure 4.4, the -6dB frequencies of the spectrum were 3.05 MHz and 4.75 MHz.

Therefore, the center frequency and the -6dB fractional bandwidth were 3.90 MHz and 43.6 %, respectively.

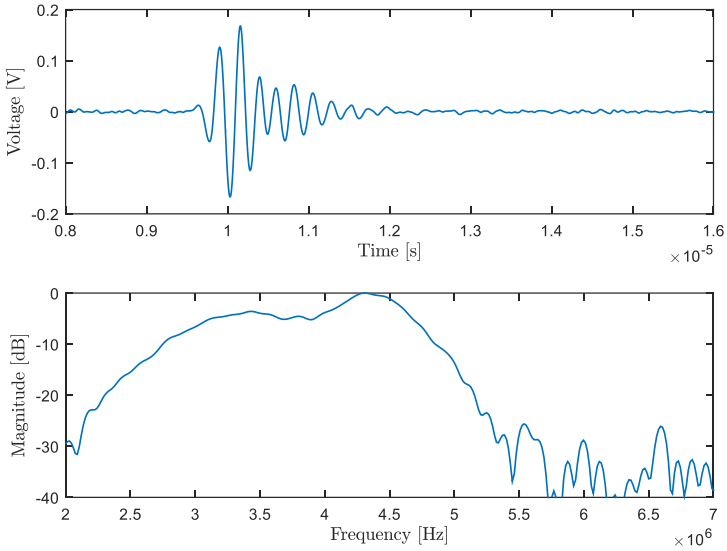


*Figure 4.4: Measured pulse-echo response of transducer (Type I): waveform in time domain and spectrum in frequency domain*

For Type II transducer as shown in Figure 4.5, the -6dB frequencies of the spectrum were 3.07 MHz and 5.05 MHz. Therefore, the center frequency and the -6dB fractional bandwidth were 4.06 MHz and 48.8 %, respectively.

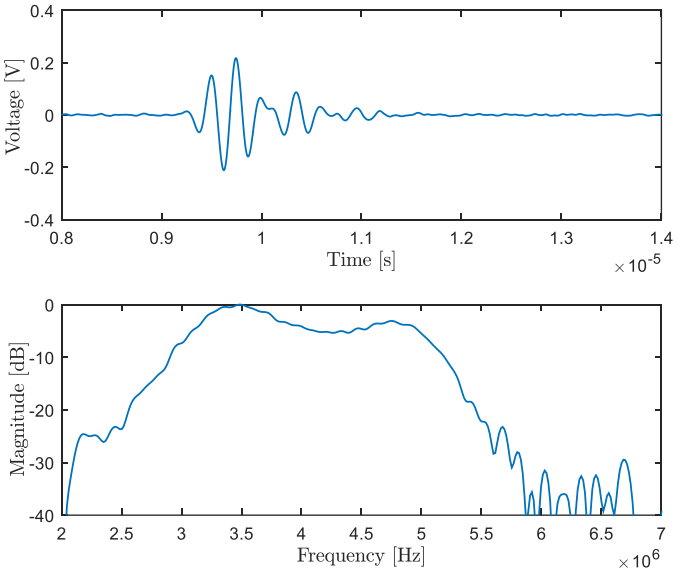


*Figure 4.5: Measured pulse-echo response of transducer (Type II): waveform in time domain and spectrum in frequency domain*

Pulse echo test results are summarized in Table 4.1.

*Table 4.1: Sumary of performance of two single-element transducers*

| | -6 dB Bandwidth (%) | Sensitivity (m/(sA)) | Center frequency (MHz) | Pulse length (μs) |
|---|---|---|---|---|
| Type I | 43.6 | 0.5146 | 3.90 | 2.35 |
| Type II | 48.8 | 0.6 | 4.06 | 2.14 |

## 4.2 One-Dimensional Linear Array Ultrasonic Transducer

### 4.2.1 Find fitted material data for Pz27 in Comsol 2D Simulation

The electrical impedance results from 1D and 2D simulations implemented by FerroPerm manufacturer material data were shown in Figure 4.6. A large mismatch between the simulated and measured results was observed.

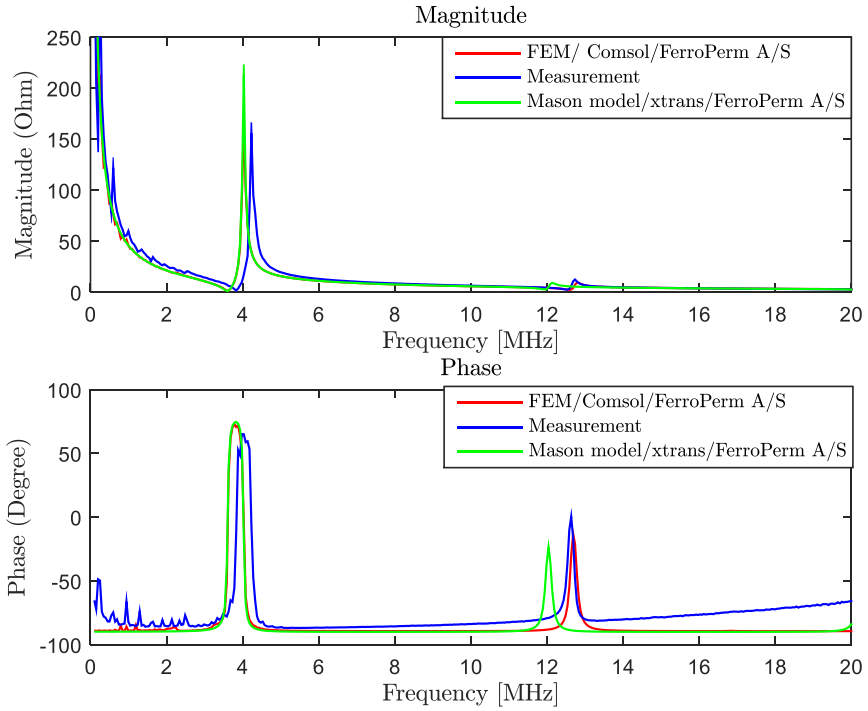


*Figure 4.6: Measured and simulated electrical impedance responses (FerroPerm)*

The electrical impedance results from 1D and 2D simulations implemented by three additional material data were shown in Figure 4.7, Figure 4.8 and Figure 4.9, respectively.

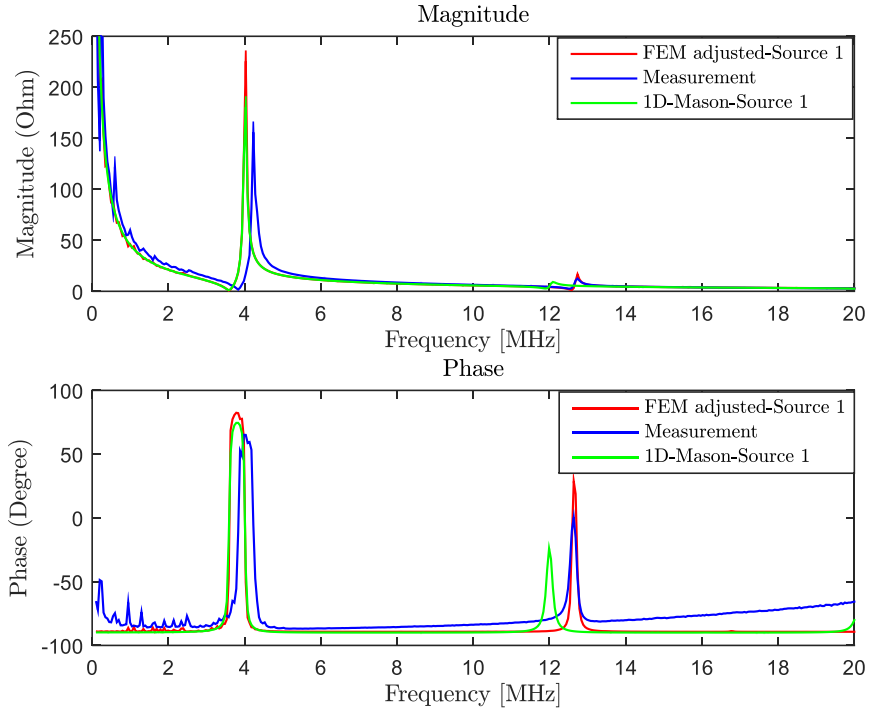


*Figure 4.7: Measured and simulated electrical impedance responses. Material data from Aanes et al.[24]*

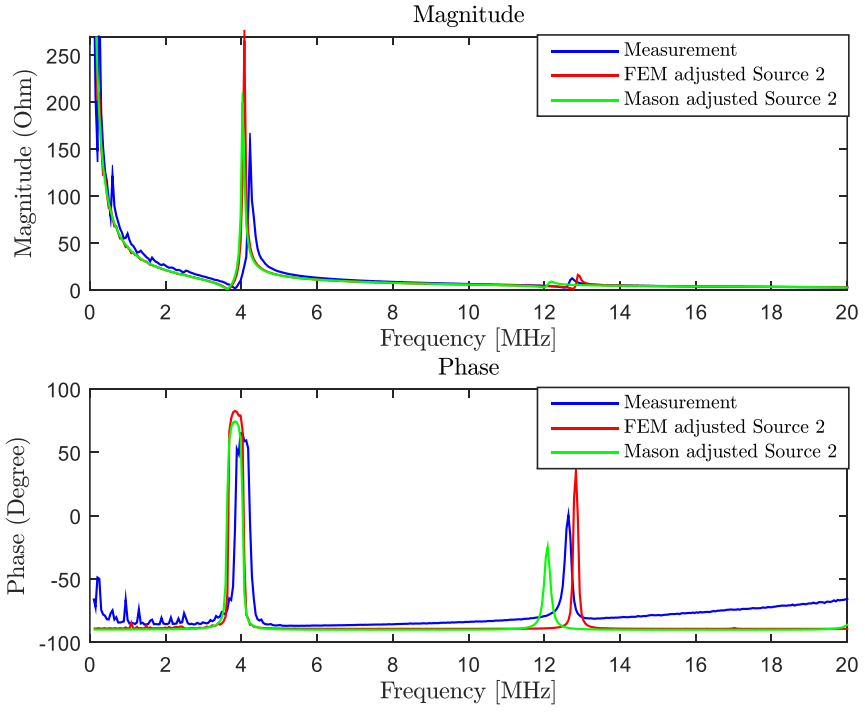


*Figure 4.8: Measured and simulated electrical impedance responses. Material data from Aanes et al. [25]*

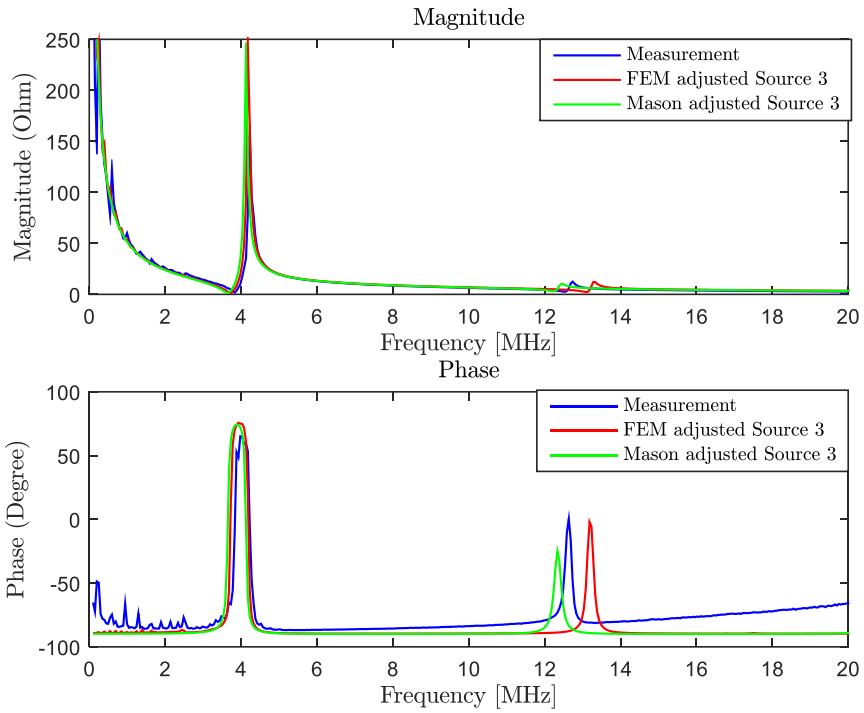


*Figure 4.9: Measured and simulated electrical impedance responses. Material data from Aanes et al.[25]Tran-Huu-Hue et al.[9]*

A large mismatch between Xtrans, FEM simulations implemented by Source 1, Source 2 dataset and measurement results were observed. However, an acceptable agreement between simulation implemented by Source 3 dataset and measurement result was clearly seen at the fundamental resonance frequencies. We only take care of thickness mode resonance; therefore, these material data are sufficient enough to predict our transducer performance.

*Table 4.2: Resonant and anti-resonant frequency of 1D Xtrans and 2D FEM comparison using Source 3 dataset*

| | Xtrans/Mason Simulation | Comsol/FEM Simulation |
|---|---|---|
| $f_a$ [MHz] | 4.13 | 4.18 |
| $f_r$ [MHz] | 3.63 | 3.73 |

Both the simulation models provided similar $f_a$ value, i.e. 4.13 MHz by Xtrans and 4.18 MHz by COMSOL. This is because $f_a$ is mainly determined by the thickness of the piezoceramic [29]. Because material data from source 3 were characterized at 4.78 MHz anti-resonant frequency that was comparable to our transducer design, a suitable agreement was noticed between simulation and measurement results. These results illustrated that the material data extracted from source 3 well predict electromechanical performance of

piezoelectric materials in COMSOL Multiphysics software. Therefore, source 3 dataset was used to simulate all COMSOL simulations in this section.

### 4.2.2 Mesh independence study

Figure 4.10 shows electrical impedance curves of three different mesh cases. The resonant and anti-resonant frequencies were recored and presented in Table 4.3. It is clearly that at the mesh density of 2695, increasing the mesh density will have very small impact on the final results. No large deviation occurs in those different mesh sizes. Based on processing time and accuracy result, the mesh size with 2695 number of elements was selected for the final COMSOL simulation. For example, for the mesh density of 2695 elements, the magnitude of electrical impedance at anti-resonant is $4.887 \times 10^4$ where that for mesh density of 2811 elements is $4.871 \times 10^4$ , i.e. the difference is about 0.3%.

*Table 4.3: Optimization of mesh size. The mesh size was utilized with the calibration of General Physics*

| Case | Number of elements | $f_r(MHz)$ | $f_a(MHz)$ | Magnitude at $f_r(\Omega)$ | Magnitude at $f_a\ (\Omega)$ |
|---|---|---|---|---|---|
| 1 | 2647 | 2.737 | 3.533 | 66.77 | $4.9 \times 10^4$ |
| 2 | 2695 | 2.737 | 3.533 | 66.77 | $4.887 \times 10^4$ |
| 3 | 2811 | 2.737 | 3.533 | 66.77 | $4.871 \times 10^4$ |

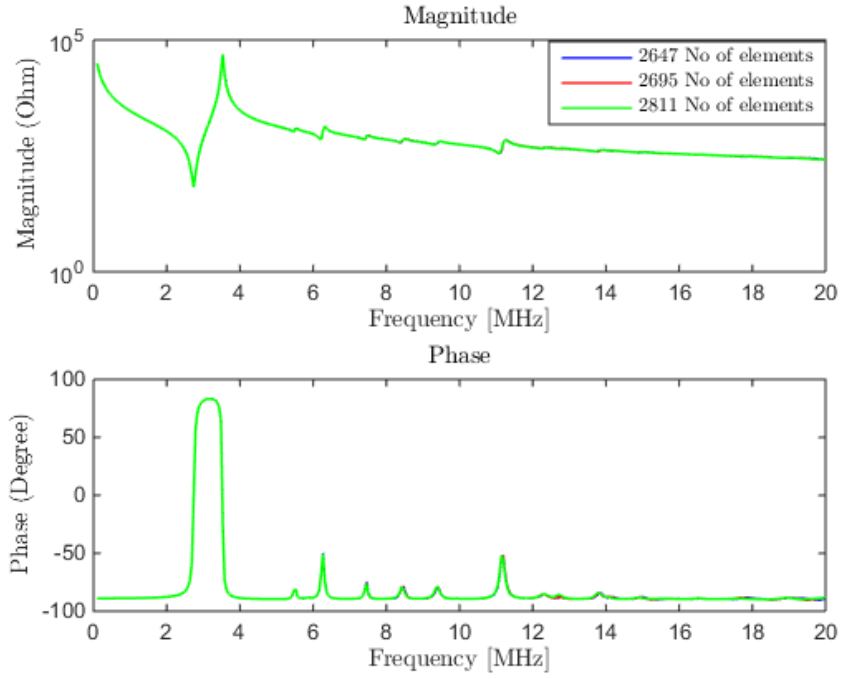


*Figure 4.10: Electrical impedance with three different mesh sizes*

### 4.2.3 Electrical characterization of linear transducer array

Completed fabricated flexible circuit is shown in Figure 4.11. This flexible circuit is responsible for electrical connection in measurement process.

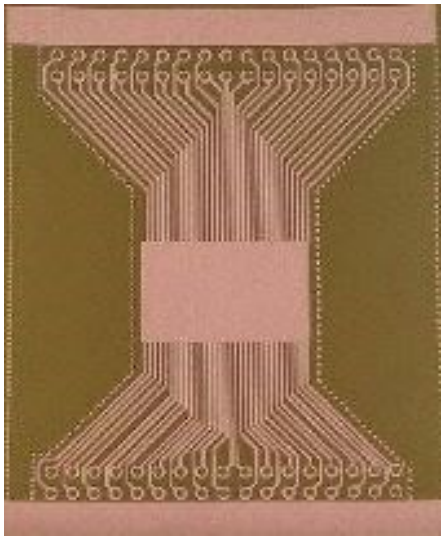

*Figure 4.11: Fabricated Flexible Circuit*

The fabricated sample after bonding piezoelectric material to flexible circuit is shown in Figure 4.12.

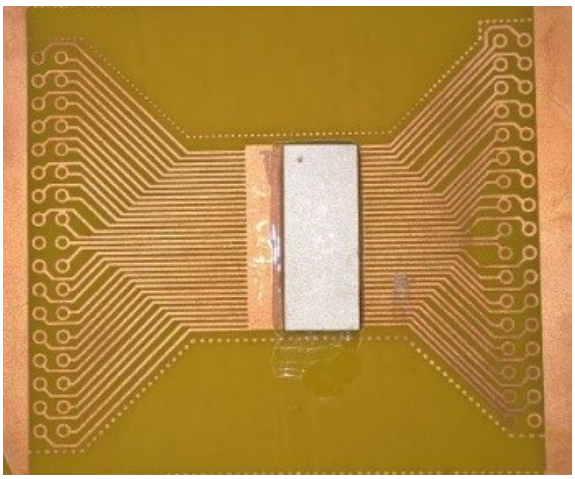

*Figure 4.12: Fabricated sample after bonding step*

After dicing fabricated sample into elements, the magnitude and phase of impedance for 53 elements were measured and shown in Figure 4.13. Measurements results are shown in blue and Comsol simulation results are shown in red.

The array displayed no shorted elements and no open elements. All of the individual element test results for the array are summarized in Table 4.4.

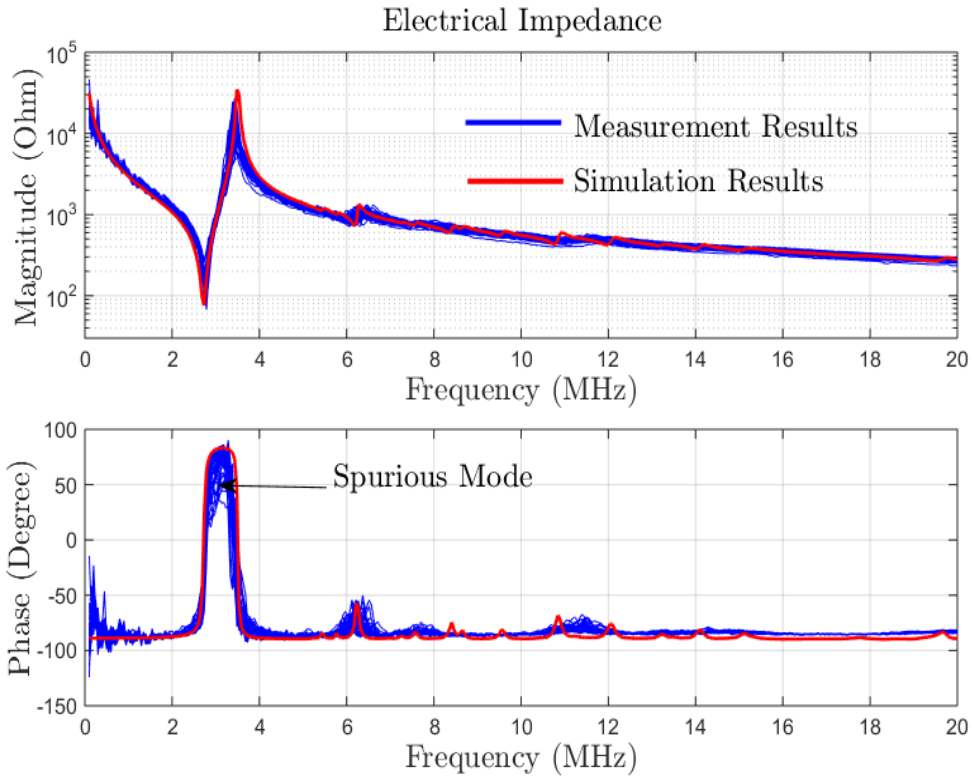


*Figure 4.13: Impedance response including magnitude and phase of 53 elements*

*Table 4.4: Measured Properties of 53-Element Array*

| Properties | Values |
|---|---|
| Number of elements | 53 |
| Number of open elements | 0 |
| Number of shorted elements | 0 |
| Average resonance frequency at thickness mode | 2.77 MHz |
| Average anti-resonance frequency at thickness mode | 3.43 MHz |

Some spread in electrical impedance was observed and needed to be explained. Variance at resonance and anti-resonance of the main thickness extension mode was shown in Figure 4.14. The magnitude at resonant frequency and maximum phase of all elements were plotted in Figure 4.15 to visualize the variation.

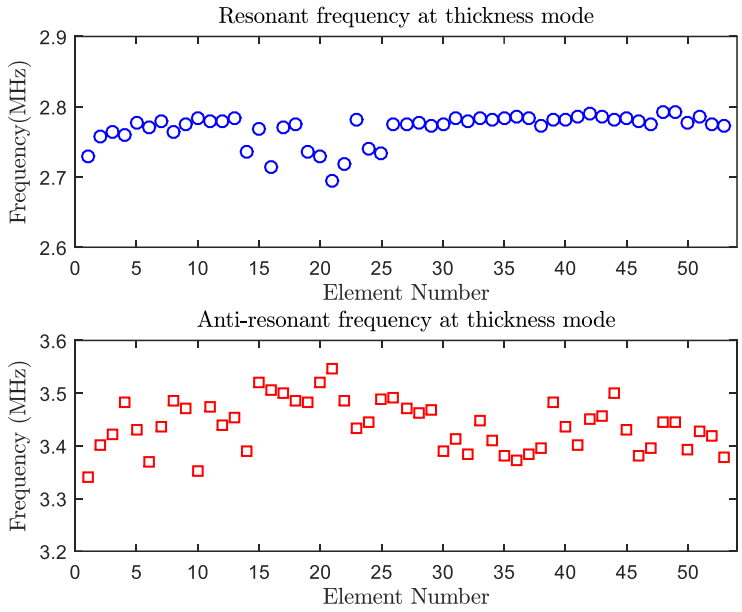


*Figure 4.14: Variation at resonant and anti-resonant frequencies of thickness mode between array elements*

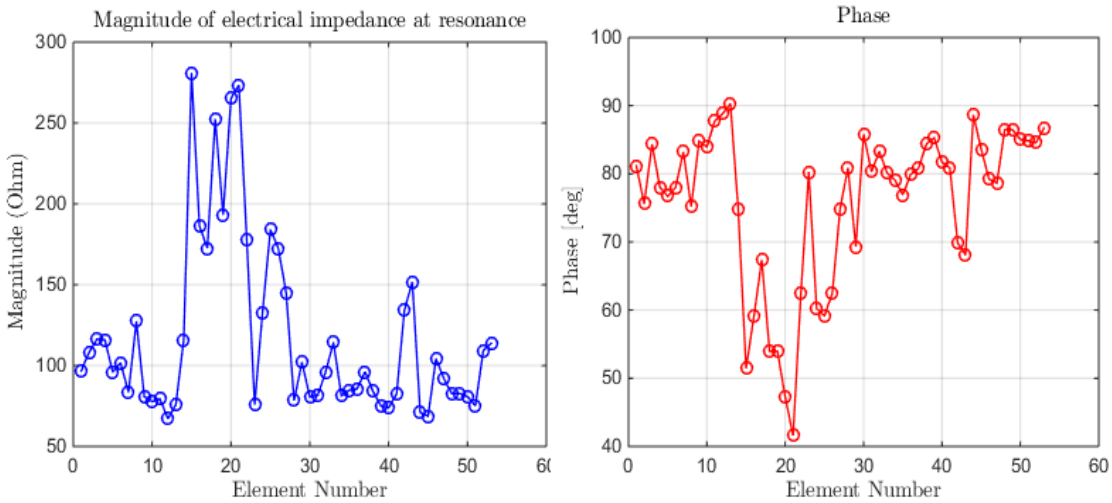


*Figure 4.15: Magnitude of electrical impedance at resonant frequency and maximum phase of each array element*

Table 4.5 shows statistical analysis of resonance frequencies at thickness mode. Table 4.6 numerically shows the variance of resonance and anti-resonance frequencies at main thickness vibrational modes by using formula in equations (3.3) (3.4).

*Table 4.5: Statistical analysis of resonance and anti-resonance frequencies at thickness mode*

| Parameters | $f_r$ (MHz) | $f_a$ (MHz) |
|---|---|---|
| Mean | 2.77 | 3.44 |
| Std | 0.02 | 0.04 |

*Table 4.6: The variance of resonance and anti-resonance frequencies at thickness mode*

| Modes | $f_{r\_max}$ (MHz) | $f_{r\_min}$ (MHz) | Variance (%) | $f_{a\_max}$ (MHz) | $f_{a\_min}$ (MHz) | Variance (%) |
|---|---|---|---|---|---|---|
| Thickness mode | 2.81 | 2.67 | 5 | 3.54 | 3.34 | 6 |

Figure 4.15 shows that some elements had magnitude at resonance larger than that of typical elements. Their magnitudes at corresponding anti-resonance were also smaller than that of typical elements. A typical and an imperfect electrical impedance element are shown in Figure 4.16 and Figure 4.17, respectively.

Spurious mode, influenced the main thickness extension mode, was also observed in Figure 4.13.

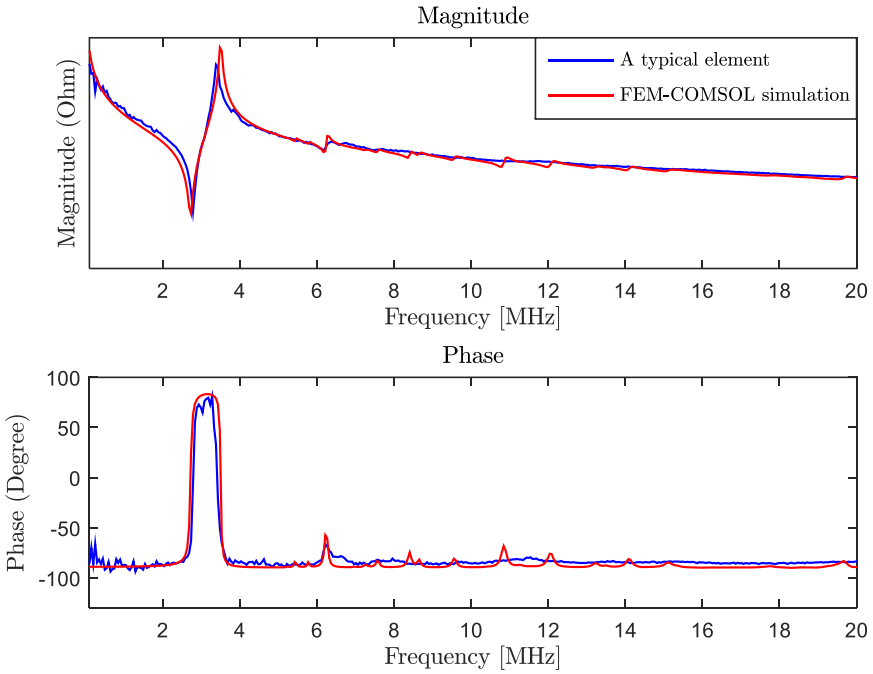


*Figure 4.16: Electrical impedance of a typical element and FEM simulations*

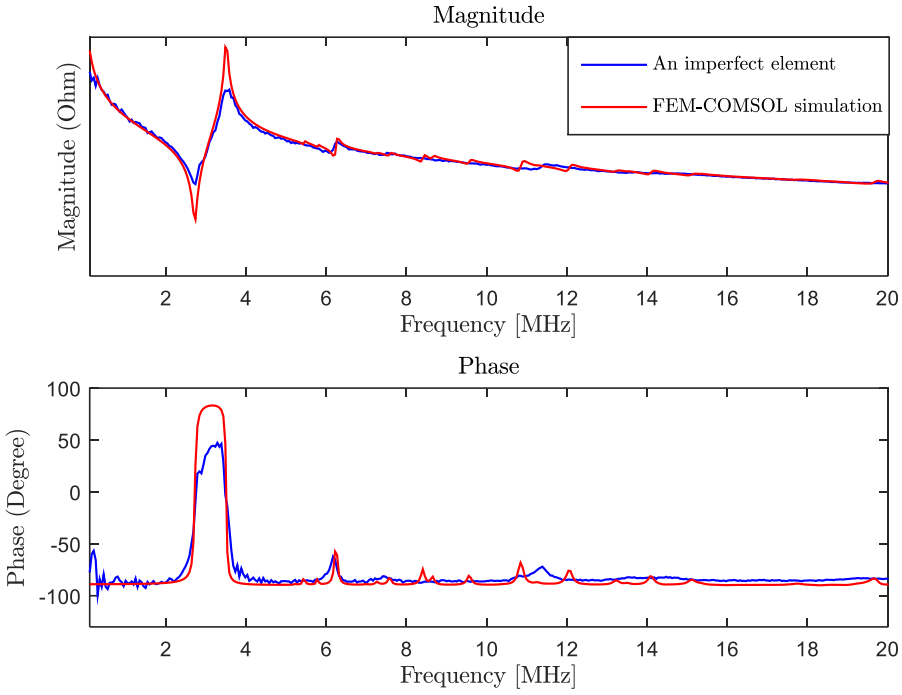


*Figure 4.17: Electrical impedance of an imperfect element and FEM simulation*

### 4.2.4 Parameters causing variation in Electrical Impedances

As mentioned in the Methods Chapter, factors that causing variation in electrical impedances were classified as geometric differences and changes in material properties. The influence of these factors will be presented in the following parts.

#### 4.2.4.1 Element width

Element width variance and its standard deviation measurement values are shown in Figure 4.18 and Table 4.7.

*Table 4.7: Element width variance across the array*

| Element width (µm) | 244.4 | 251.6 | 260.2 |
|---|---|---|---|
| Element width σ (std) (µm) | 1.1 | 0.9 | 1.2 |

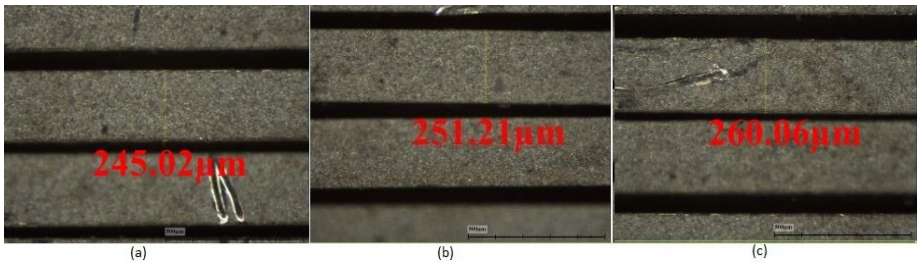


*Figure 4.18: Element width variation in the array elements*

Figure 4.19 shows the FEM-simulations of effect of varying the element width on electrical impedance of an element. The simulation confirmed that as the element width increases, the resonant peak shifts down from 6.40 MHz to 6.10 MHz. Element width variance approximately from 244 µm to 260 µm was found to create a 5% downward shift at width-extentional mode. In addition, no measurable affect on resonance at thickness mode was observed.

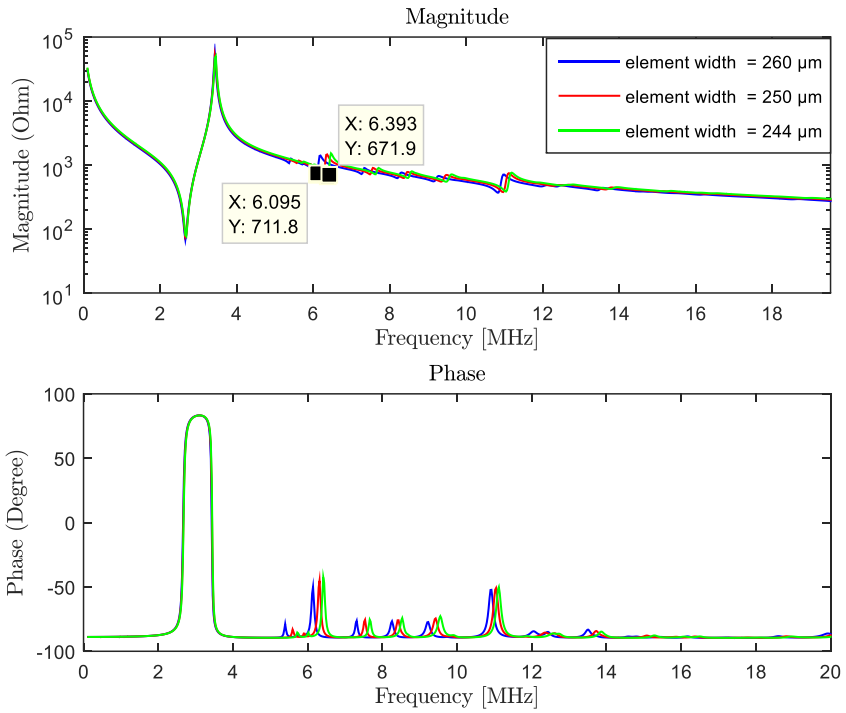


*Figure 4.19: FEM-simulations of electrical impedances with different element widths*

Figure 4.20 shows vibration pattern of the width-extensional mode of a 250 µm-width element case.

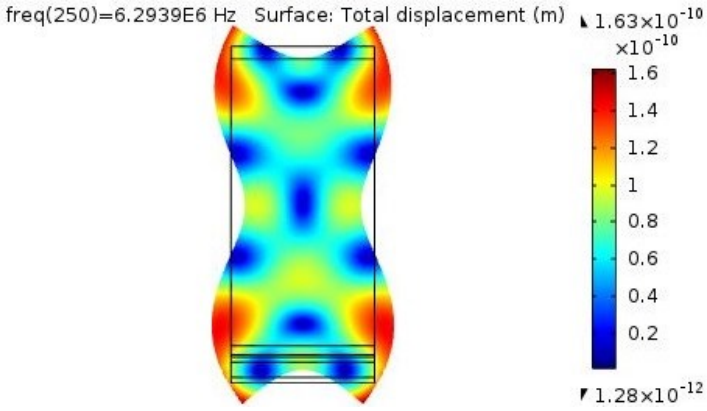


*Figure 4.20: Finite element analysis (FEA) of the width-extensional resonant mode of 250 um-width element*

### 4.2.4.2 Kerf shape

When a sample was diced by a diamond blade, some kerfs were not ideally identical at both the top and bottom. Figure 4.21 shows the image of a sample diced with a blade Z09-SD1700-Y1-60 53.4x0.033ASx40.

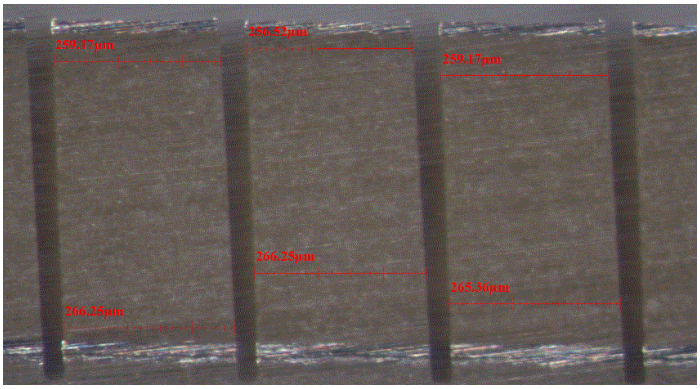


*Figure 4.21: An image of a sample diced by blade Z09. The image shows non-vertical kerf width. The kerf is smaller at the bottom than at the top*

The kerf at the bottom is a little smaller than that at the top of element. This deviation was defined as an offset value. Therefore, the element's width at the bottom was larger than that at the top. Table 4.8 shows offset values being investigated in COMSOL model.

*Table 4.8: Variation in kerf shape*

| | | |
|---|---|---|
| Offset (μm) | 2.5 | 5 |

Figure 4.22 shows the effect of kerf shape on electrical impedance with different offset values.

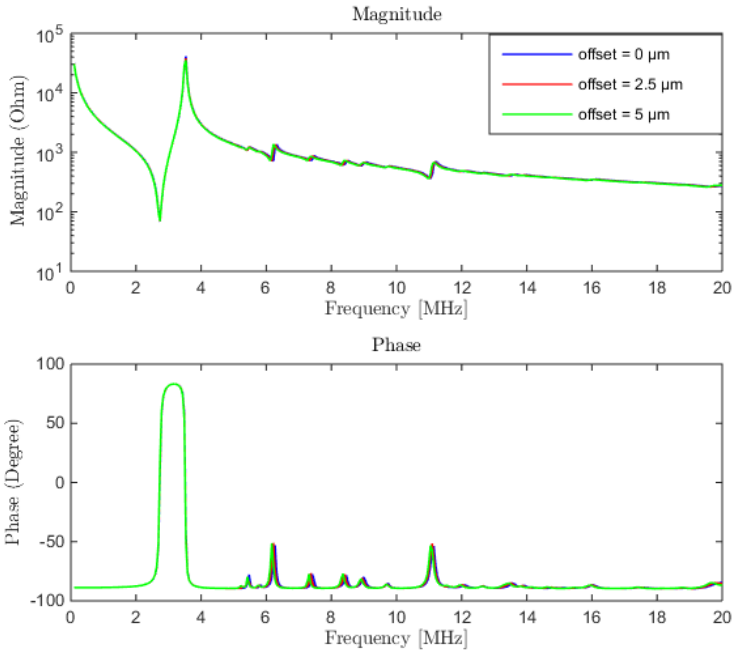


*Figure 4.22: FEM-simulations of electrical impedances with different offset values, i.e. the difference in kerf width at the top and the bottom*

### 4.2.4.3 Piezoelectric material thickness

Piezoelectric material thickness variance and standard deviation of the array are shown in Figure 4.23 and Table 4.9.

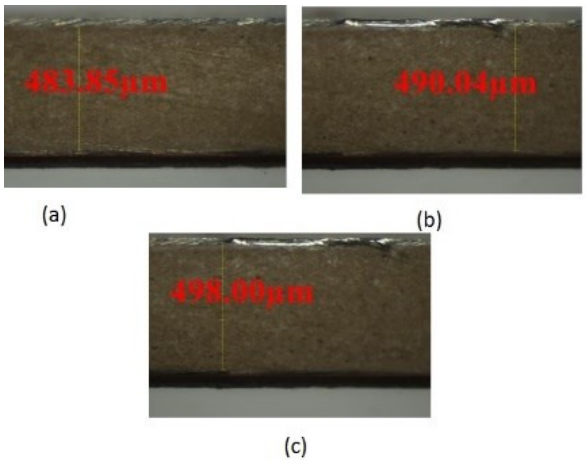


*Figure 4.23: Piezoelectric material thickness variance in array elements*

*Table 4.9: Piezoelectric material thickness variance*

| PZT thickness (µm) | 483.4 | 490.6 | 498.2 |
|---|---|---|---|
| PZT thickness σ (std) (µm) | 0.8 | 1.1 | 0.7 |

These values were inputed into COMSOL model to simulate the effect of PZT thickness on electrical impedances. As the piezoelectric material thickness increases, the resonance peak at thickness vibration mode shifts down from 2.76 MHz to 2.69 MHz, approximately 3% (Figure 4.24). Similar results were also observed at anti-resonance peak.

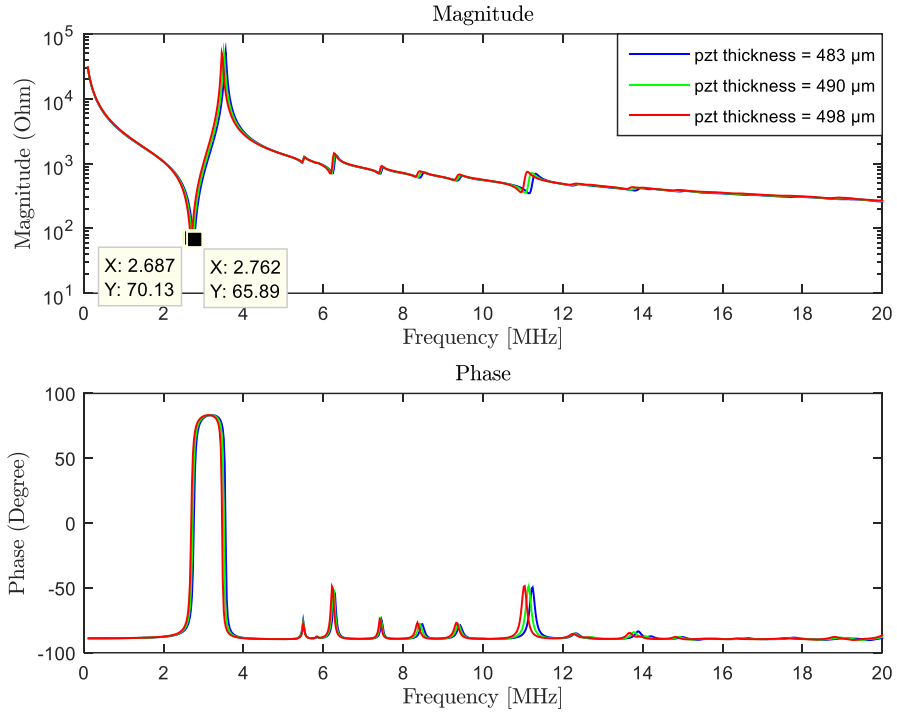


*Figure 4.24: FEM-simulations of electrical impedances with piezoelectric material thickness values*

### 4.2.4.4 Electrode thickness

Figure 4.25 and Table 4.10 show electrode thickness variance and its standard deviation values in the arrays. These values were inputed into COMSOL model to simulate the effect of electrode thickness on electrical impedances. As the electrode thickness increases, the resonance peak at thickness vibration mode shifts down from 2.74 MHz to 2.69 MHz, approximately 2% (Figure 4.26).

*Table 4.10: Electrode thickness variance*

| Electrode thickness (μm) | 18.1 | 20.3 | 22.2 |
|---|---|---|---|
| Electrode thickness σ (μm) | 0.4 | 0.5 | 0.6 |

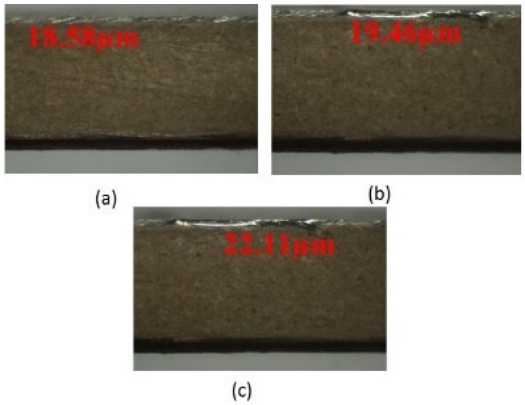


*Figure 4.25: Electrodes thickness variance in array elements*

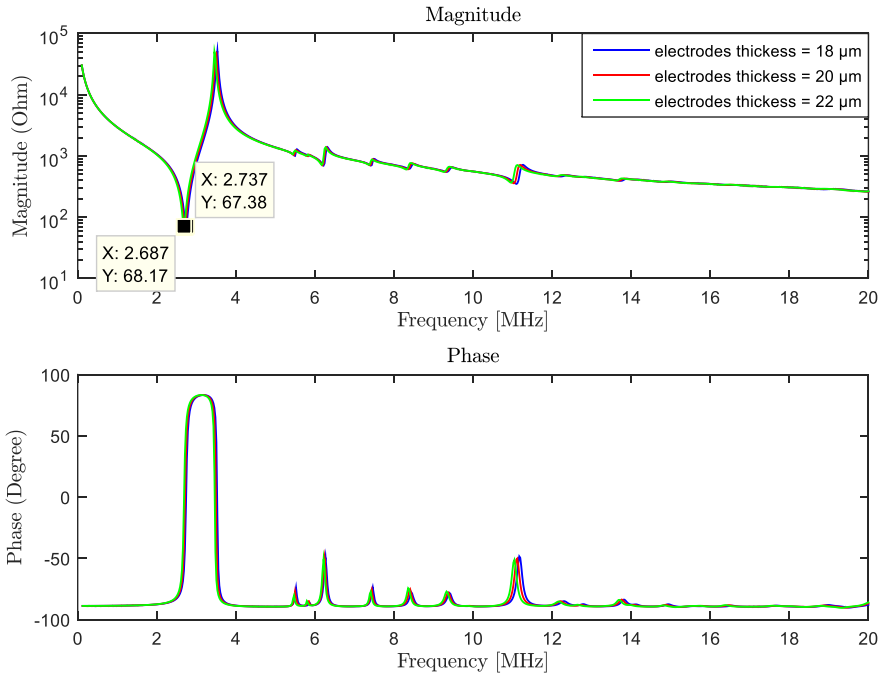


*Figure 4.26: FEM-simulations of electrical impedances with different electrodes thickness*

### 4.2.4.5 Material property changes

Material property changes were identified as the main source of the impedance variations, causing a decrease of nearly 50% in magnitude at the anti-resonant frequency, and an increase of 160% to 200 % at the resonant frequency.

Model in Figure 3.8 with 15 µm-thick dead zone on both size of an element was proposed to investigate the change of piezoelectric material data at that region during dicing process. Thickness mode (TM) resonance was our main concern, therefore; we investigated loss values of elastic and dielectric constants at that mode.

a. Influence of Mechanical losses

We simulated the effect of modifying the imaginary part of a mechanical loss around the reference value given in Table 3.5. The effect produced by the change of the mechanical loss is shown in Table 4.27 and Table 4.28.

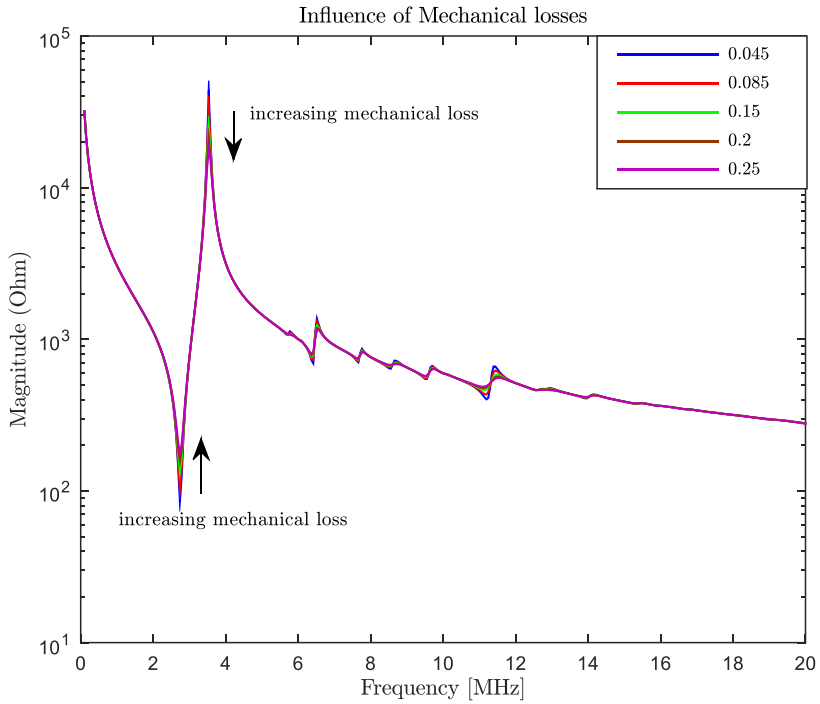


*Figure 4.27: FEM-simulations of influence of mechanical loss on magnitude of the electrical impedance response*

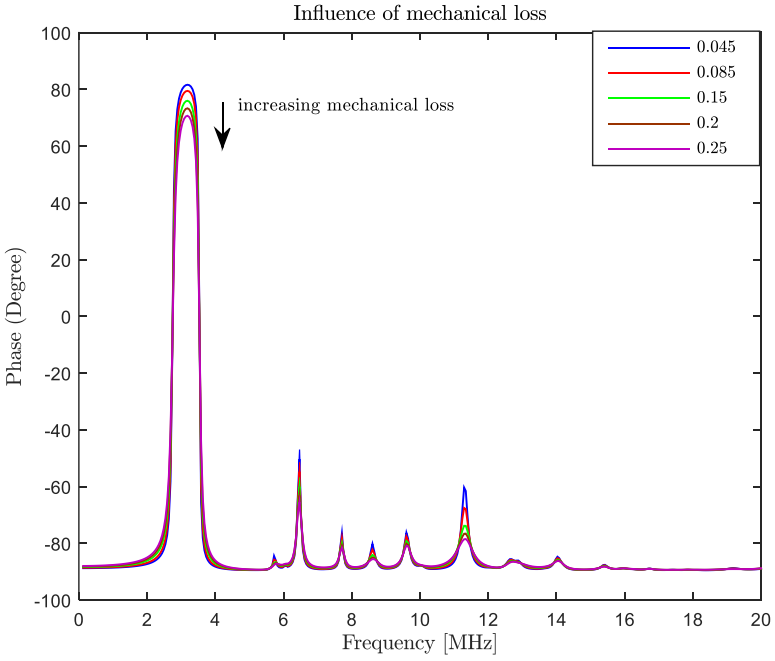


*Figure 4.28: FEM-simulations of influence of mechanical loss on phase of the electrical impedance response*

b. Influence of Dielectric losses

The influence of the dielectric loss on electrical impedance is shown in Figure 4.29 and Figure 4.30.

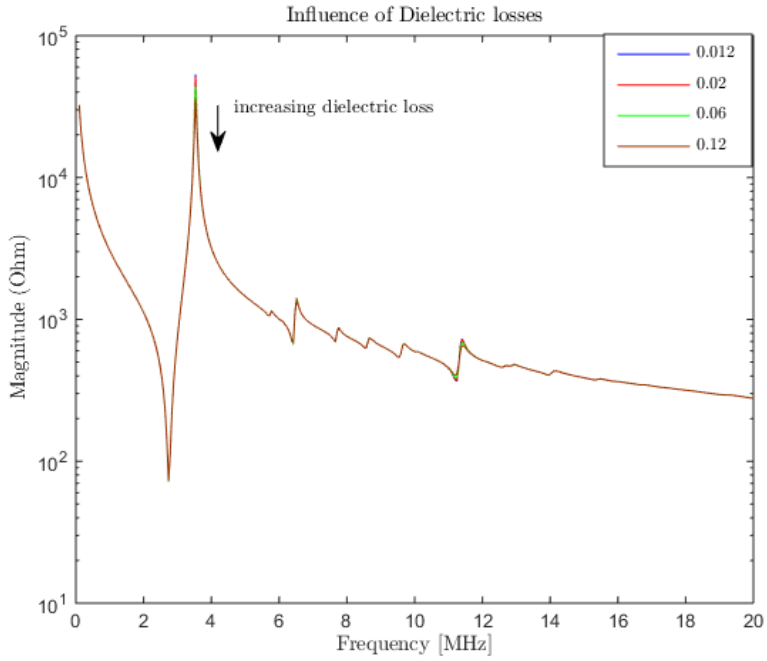


*Figure 4.29: FEM-simulations of influence of dielectric loss on magnitude of the electrical impedance response*

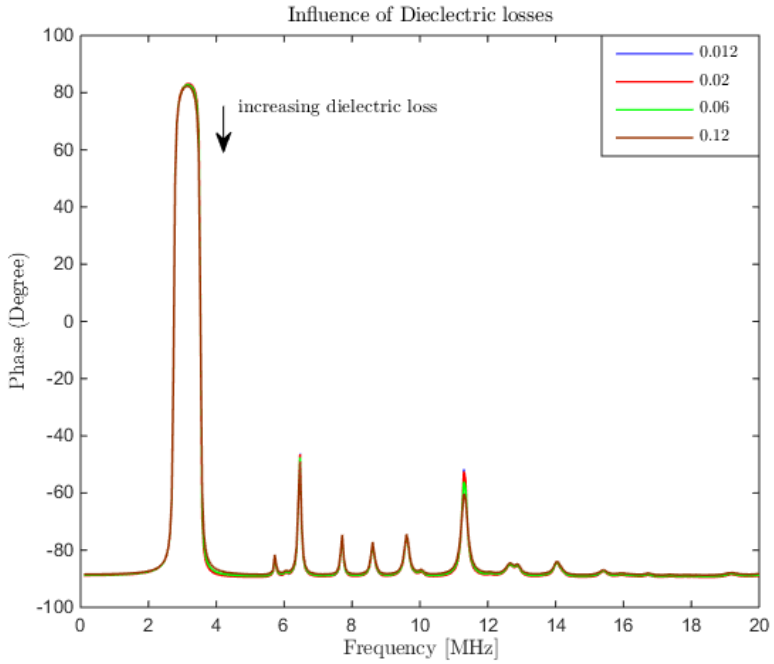


*Figure 4.30: FEM-simulations of influence of dielectric loss on phase of the electrical impedance response*

#### 4.2.4.6 Debris inside the kerf

Noticeable spurious mode influences the main extension mode (Figure 4.13). This undesired mode is most probably related to procedures during fabrication steps. When dicing into elements, some debris from piezoelectric material might drop inside the kerfs causing interaction between elements.

Model in Figure 3.9 was proposed with debris inside the kerf to study this phenomenon. The spurious mode was investigated by changing the debris thickness from 1 to 7 per cent of the piezoelectric material's. Magnitude and phase impedance response were plotted in Figure 4.31 and Figure 4.32 to visualize this mode.

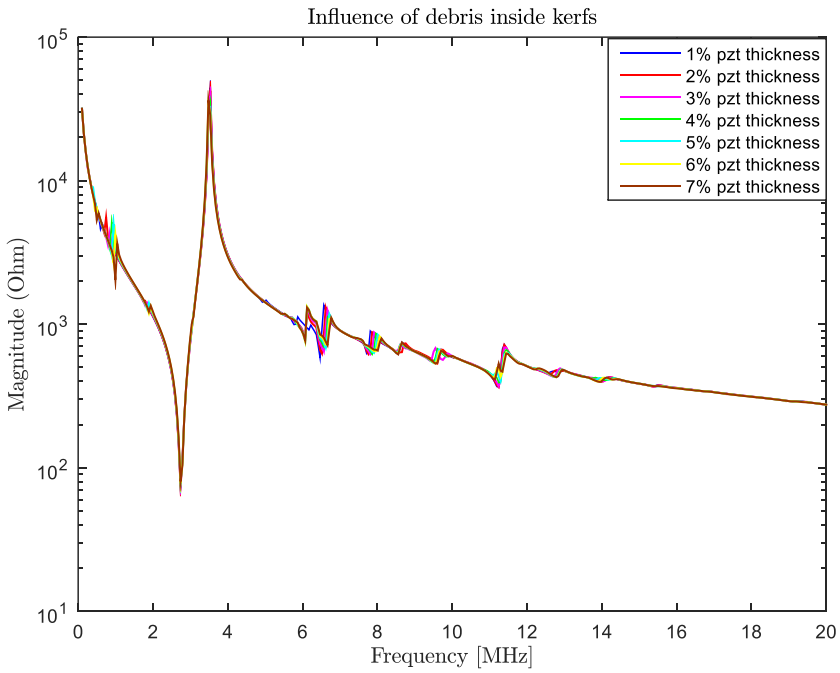


*Figure 4.31: FEM-simulations of impedance magnitude with different debris thicknesses*

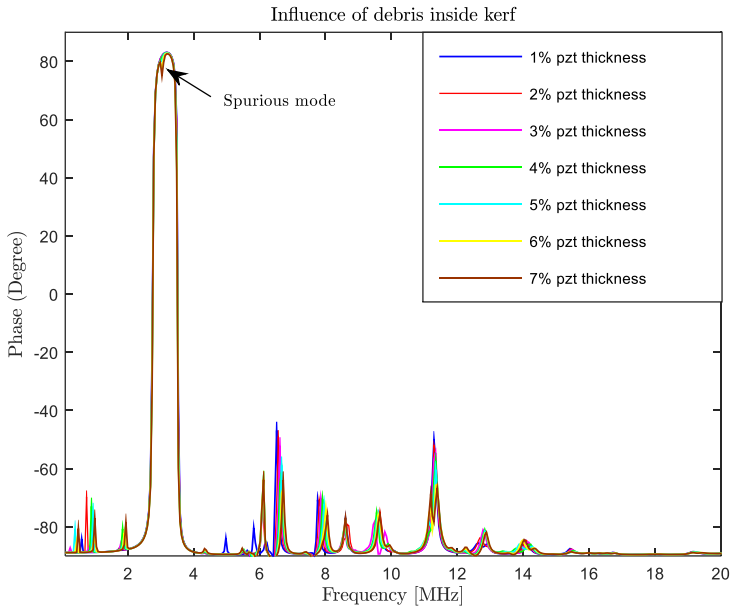


*Figure 4.32: FEM-simulations of impedance phase with different debris thicknesses*

## 4.3 Piezoelectric linear array ultrasonic transducer using different bonding methods

### 4.3.1 Intermetallic layer property in SLID bond line and mesh independent study

Electrical impedance of an array element with three different properties of the intermetallic layer was shown in Figure 4.33.

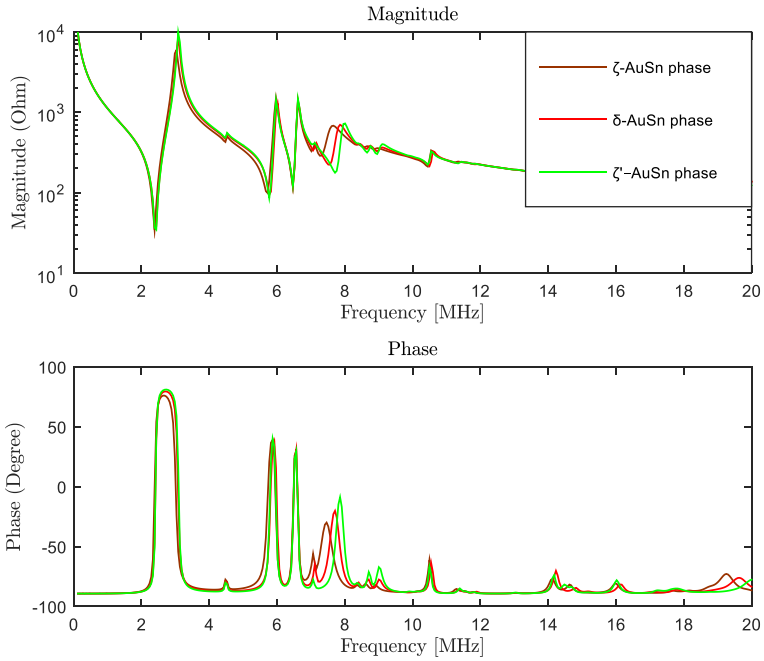


*Figure 4.33: FEM-simulations of electrical impedances of an array element with three different material data of intermetallic layer in SLID bond line*

Only a large mismatch was seen at fourth vibrational mode. After comparing these electrical impedance curves to measurement results, the simulation result using parameters of ζ-AuSn phase was the most well fitted one. Therefore, ζ-AuSn phase was assumed to be the intermetallic layer in the bond line for conducting all simulations in this model. Figure 4.35 showed total displacement of an array element at different vibrational modes of a typical model that ζ-AuSn phase was present in the intermetallic layer.

Figure 4.34 shows electrical impedance curves of three different mesh cases. The resonant and anti-resonant frequencies were recored and presented in Table 4.11. It is clearly that at the mesh density of 4418, increasing the mesh density will have very small impact on the final results. No large deviation occurs in those different mesh sizes. Based on processing time and accuracy result, the mesh size with 4418 number of elements was selected for all simulations in the Result section. For example, for the mesh density of 4418 elements, the magnitude of electrical impedance at anti-resonant is 5950 while that for mesh density of 4667 elements is 5951, i.e. the difference is about 0.02 %.

*Table 4.11: Optimization of mesh size. The mesh size was utilized with the calibration of General Physics*

| Case | Number of domain elements | $f_r(MHz)$ | $f_a(MHz)$ | Magnitude at $f_r(\Omega)$ | Magnitude at $f_a\ (\Omega)$ |
|---|---|---|---|---|---|
| 1 | 4418 | 2.389 | 3.035 | 34.51 | 5950 |
| 2 | 4476 | 2.389 | 3.035 | 34.51 | 5950 |
| 3 | 4667 | 2.389 | 3.035 | 34.51 | 5951 |

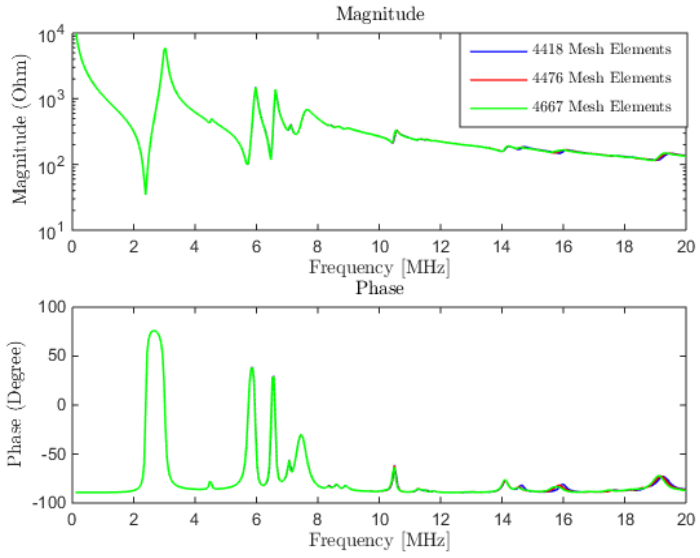


*Figure 4.34: Electrical Impedance with three different mesh sizes*

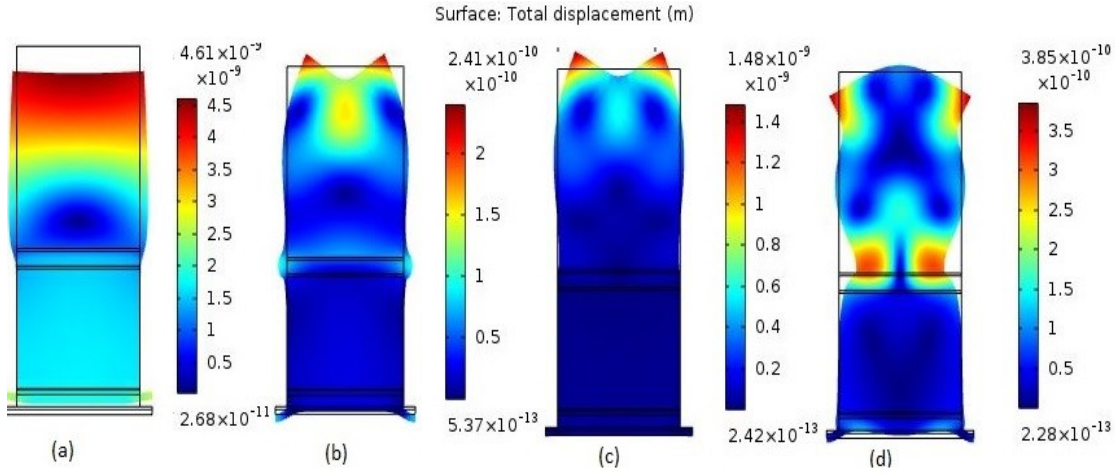


*Figure 4.35: Total displacement at 4 different vibrational modes (a) Thickness mode (b) Second Vibrational mode (c) Third Vibrational mode (d) Fourth Vibrational mode*

### 4.3.2 Electrical characterization of array element in SLID bonding method

The linear array's impedance was measured in air using the network analyser HP8753D. The magnitude and phase of 64 elements are shown in Figure 4.36. All 64 electrical impedances of element are shown in blue while that of FEM Comsol simulation is shown in red.

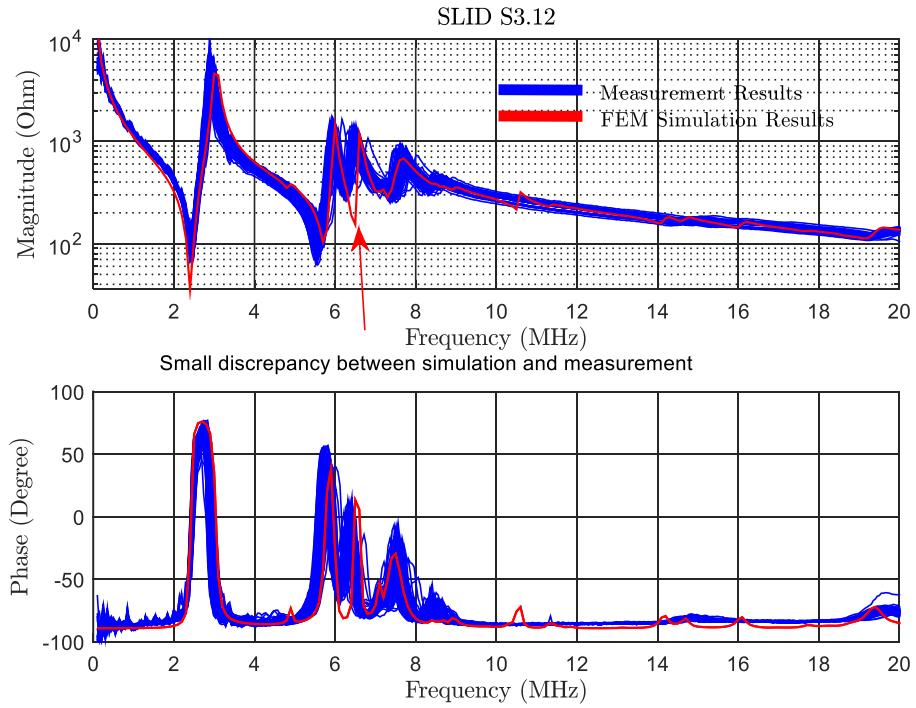


*Figure 4.36: Impedance response including magnitude and phase of 64 elements*

The array displayed no shorted elements and no open elements. All of the individual element test results for the array are summarized in Table 4.12.

*Table 4.12: Measured Properties for the 64-Element Array*

| Properties | Values |
|---|---|
| Number of elements | 64 |
| Number of open elements | 0 |
| Number of shorted elements | 0 |
| Average resonance frequency at thickness mode | 2.44 MHz |
| Average anti-resonance frequency at thickness mode | 2.97 MHz |

Figure 4.37 and Figure 4.38 show the variation at thickness, second, third and fourth vibrational modes, respectively, of two typical array elements. Large spread in electrical impedance curves can be observed at different frequency ranges.

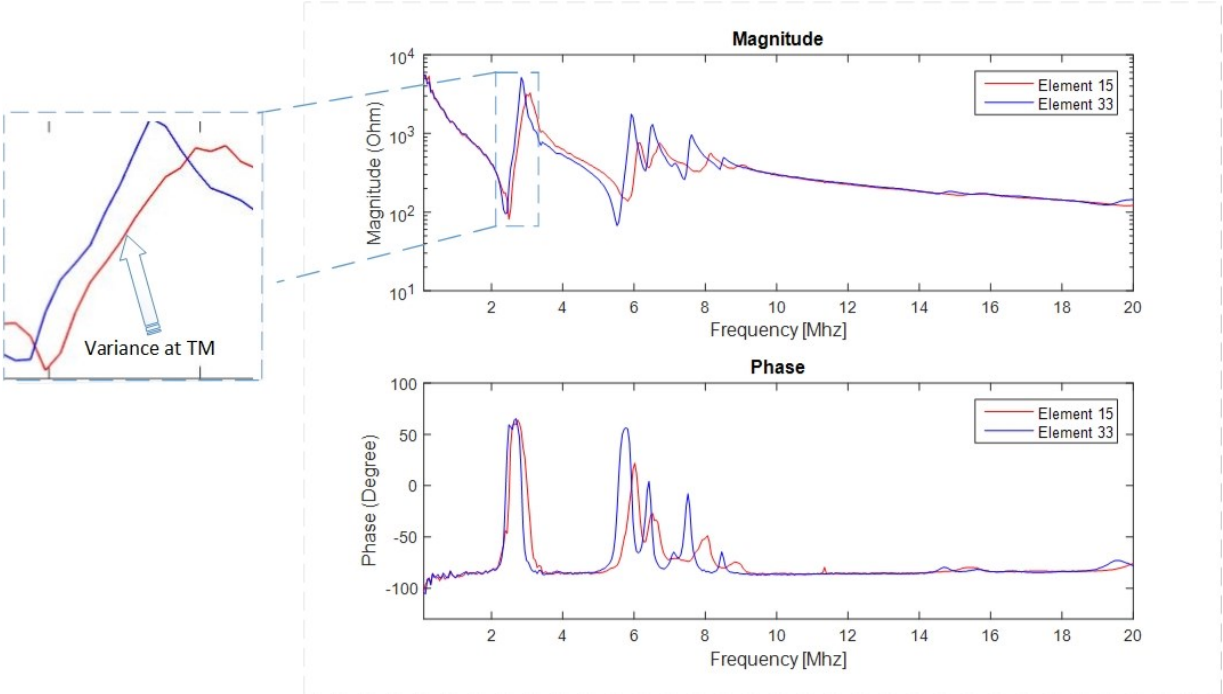


*Figure 4.37: The variation at thickness vibration mode of two array elements*

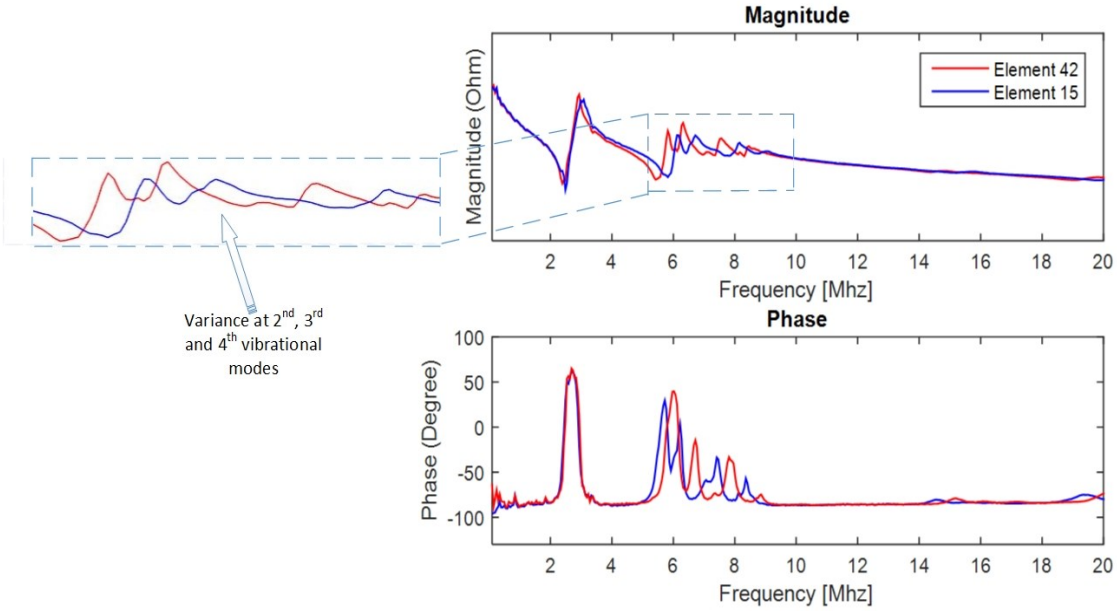


*Figure 4.38: The variation at second, third and fourth vibrational modes of two array elements*

To numerically visualize these variations, the variance of resonance $f_r$ and anti-resonance $f_a$ frequencies at different vibrational modes was collected and plotted as shown in the following figures. Figure 4.39, Figure 4.40, Figure 4.41 and Figure 4.42 show the variation of resonance and anti-resonance frequencies of array elements at different vibrational modes, respectively.

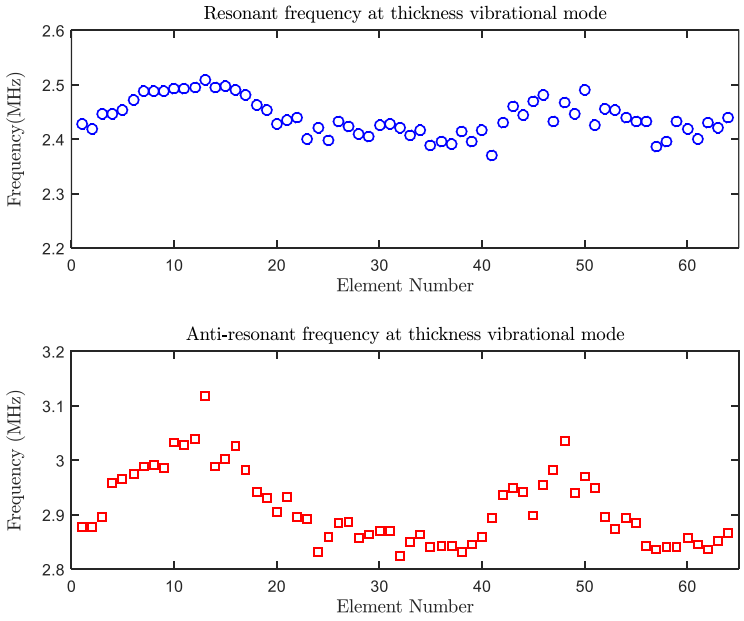


*Figure 4.39: The variation of resonance and anti-resonance frequencies at thickness vibration mode across the array*

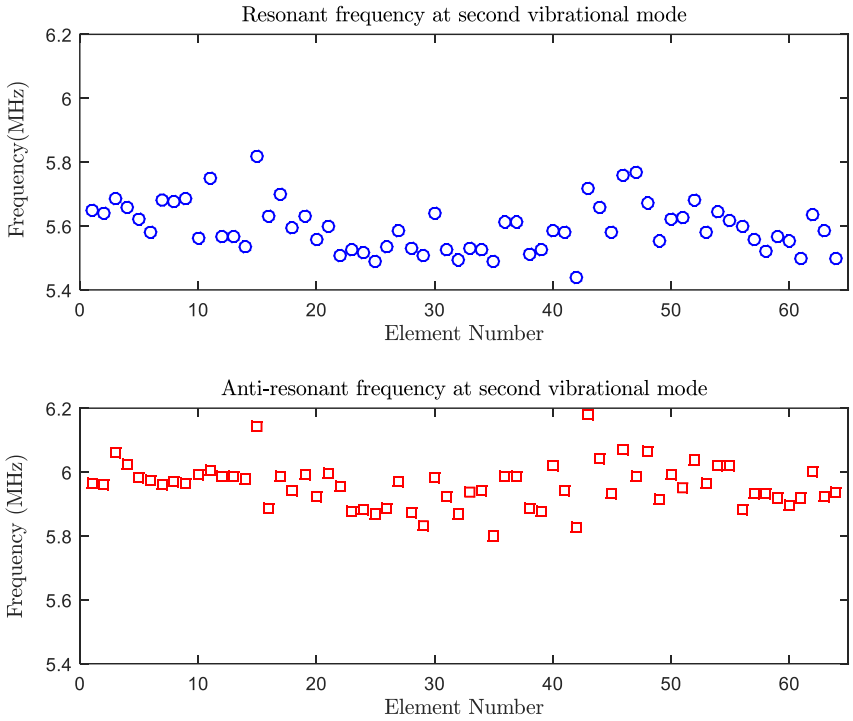


*Figure 4.40: The variation of resonant and anti-resonant frequencies at second vibrational mode across the array*

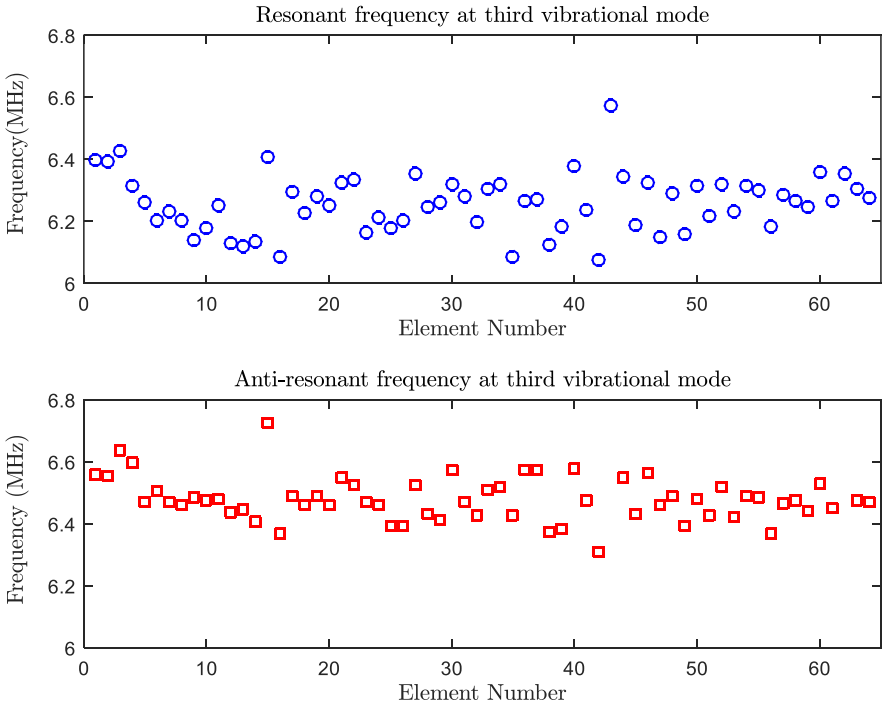


*Figure 4.41: The variation of resonant and anti-resonant frequencies at third vibrational mode across the array*

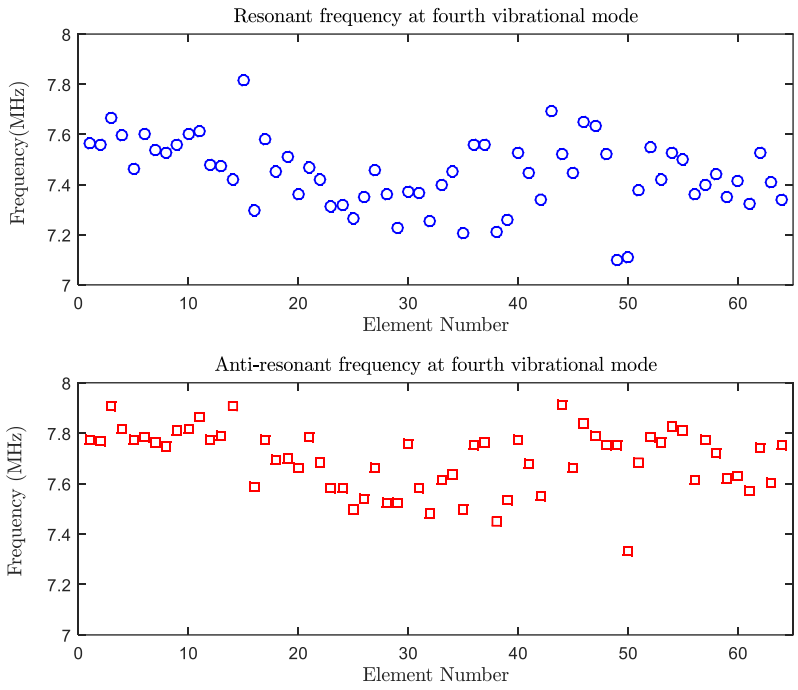


*Figure 4.42: The variation of resonant and anti-resonant frequencies at fourth vibrational mode across the array*

Table 4.13 summarizes the mean, standard deviation and coefficient of variation of resonance and anti-resonance frequencies at different vibrational modes.

*Table 4.13: Statistical analysis of resonance and anti-resonance frequencies at different vibrational modes*

| | $f_{r1}$ | $f_{a1}$ | $f_{r2}$ | $f_{a2}$ | $f_{r3}$ | $f_{a3}$ | $f_{r4}$ | $f_{a4}$ |
|---|---|---|---|---|---|---|---|---|
| Mean (MHz) | 2.44 | 2.91 | 5.60 | 5.96 | 6.26 | 6.49 | 7.44 | 7.71 |
| Std (MHz) | 0.03 | 0.07 | 0.08 | 0.07 | 0.09 | 0.12 | 0.14 | 0.14 |
| CV (%) | 1.23 | 2.41 | 1.43 | 1.17 | 1.44 | 1.85 | 1.88 | 1.82 |

where $f_{r1}, f_{a1}, f_{r2}, f_{a2}, f_{r3}, f_{a3}, f_{r4}, f_{a4}$ are resonant and antiresonant frequencies at four different modes, respectively.

Table 4.14 numerically shows the variance of resonance and anti-resonance frequencies at different vibrational modes.

*Table 4.14: The variance of resonance and anti-resonance frequencies at different vibrational modes*

| Modes | $f_{rmax}$ (MHz) | $f_{rmin}$ (MHz) | Variance (%) | $f_{amax}$ (MHz) | $f_{amin}$ (MHz) | Variance (%) |
|---|---|---|---|---|---|---|
| TM | 2.51 | 2.37 | 5.6 | 3.12 | 2.82 | 9.6 |
| 2nd mode | 5.82 | 5.44 | 6.5 | 6.18 | 5.80 | 6.1 |
| 3rd mode | 6.58 | 6.08 | 7.6 | 7.10 | 6.39 | 10 |
| 4th mode | 7.81 | 7.10 | 9.1 | 8.15 | 7.3 | 9.7 |

### 4.3.3 Parameters causing variations in electrical impedance in SLID bonding method

The spread in electrical impedance curves can be attributed to variation in geometric structures such as piezoelectric thickness, element width and SLID bond line thickness. Void formation in the SLID bond line was also another factor that created loss and shifted down resonances. In the following part, influence of each factor will be investigated and analyzed. How these factors contribute to the spread in electrical impedance curves was presented numerically by graphs in the following parts.

#### 4.3.3.1 Element width

Figure 4.43 and Table 4.15 show the results of the element width and its standard deviation values of the fabricated array. Element width was seen to vary slightly from element to element.

*Table 4.15: Element width variance of the array*

| Element width (µm) | 245.4 | 250.6 | 255.5 |
|---|---|---|---|
| Element width σ (µm) | 1.1 | 0.9 | 1.2 |

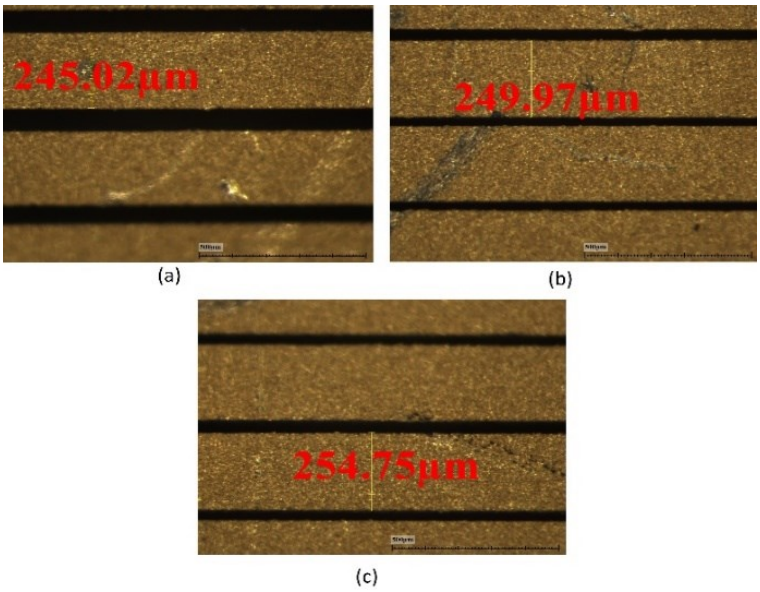


*Figure 4.43: Element width variance (a) 245 µm (b) 250 µm (c) 255 µm*

This range of element width with 5 µm step was chosen to investigate element width influence on electrical impedance curves in COMSOL. Figure 4.44 shows COMSOL

simulation results with 3 different element width parameters. Variation in electrical impedances was observed at second, third and fourth vibrational modes.

Equations (3.8) (3.9) were also used to calculate variation at each mode. Table 4.16 numerically illustrates the influence of element width variation at different vibrational modes on electrical impedance curves more clearly.

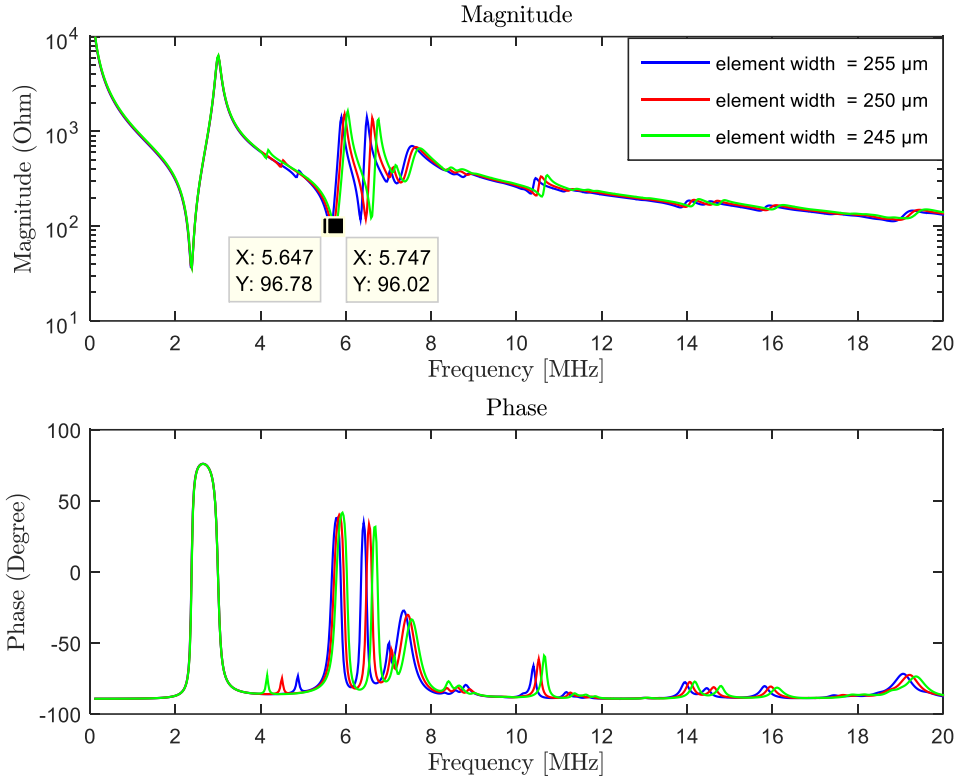


*Figure 4.44: FEM-simulations of electrical impedances with different element widths*

*Table 4.16: The variance of resonance and anti-resonance frequencies at different vibrational modes due to element width variation*

| Modes | $f_{rmax}$ (MHz) | $f_{rmin}$ (MHz) | Variance (%) | $f_{amax}$ (MHz) | $f_{amin}$ (MHz) | Variance (%) |
|---|---|---|---|---|---|---|
| TM | 2.39 | 2.39 | 0 | 3.01 | 3.01 | 0 |
| 2nd mode | 5.75 | 5.65 | 1.7 | 6.05 | 5.90 | 2.5 |
| 3rd mode | 6.60 | 6.34 | 4.0 | 6.77 | 6.50 | 4.0 |
| 4th mode | 7.39 | 7.19 | 2.7 | 7.74 | 7.54 | 2.6 |

#### 4.3.3.2 PZT thickness

PZT thickness variation and its standard deviation values of fabricated array are shown in Figure 4.45 and Table 4.17. PZT thickness was observed to vary from element to element.

*Table 4.17: PZT thickness measurements of the array*

| | | | |
|---|---|---|---|
| PZT thickness (µm) | 345.4 | 351.1 | 355.7 |
| PZT thickness σ (µm) | 0.8 | 0.9 | 1.0 |

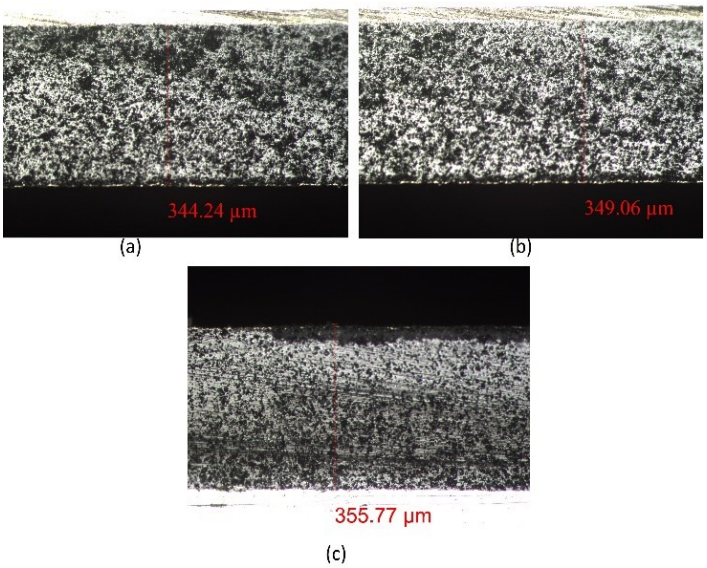


*Figure 4.45: PZT thickness variance (a) 345 µm (b) 350 µm (c) 355 µm*

Electrical impedance of an element was simulated using COMSOL model with different PZT thickness parameters, i.e. 5 µm step (Figure 4.46).

Equations (3.8) (3.9) were also used to calculate variation at each mode. The spread at different vibrational modes due to piezoelectric material thickness are obviously illustrated in Table 4.18.

*Table 4.18: The variance of resonance and anti-resonance frequencies at different vibrational modes due to PZT thickness variation*

| Modes | $f_{rmax}$ (MHz) | $f_{rmin}$ (MHz) | Variance (%) | $f_{amax}$ (MHz) | $f_{amin}$ (MHz) | Variance (%) |
|---|---|---|---|---|---|---|
| TM | 2.44 | 2.39 | 2.0 | 3.09 | 3.01 | 2.5 |
| 2nd mode | 5.75 | 5.70 | 0.9 | 6.02 | 5.97 | 0.8 |
| 3rd mode | 6.47 | 6.47 | 0 | 6.61 | 6.61 | 0 |
| 4th mode | 7.31 | 7.31 | 0 | 7.66 | 7.66 | 0 |

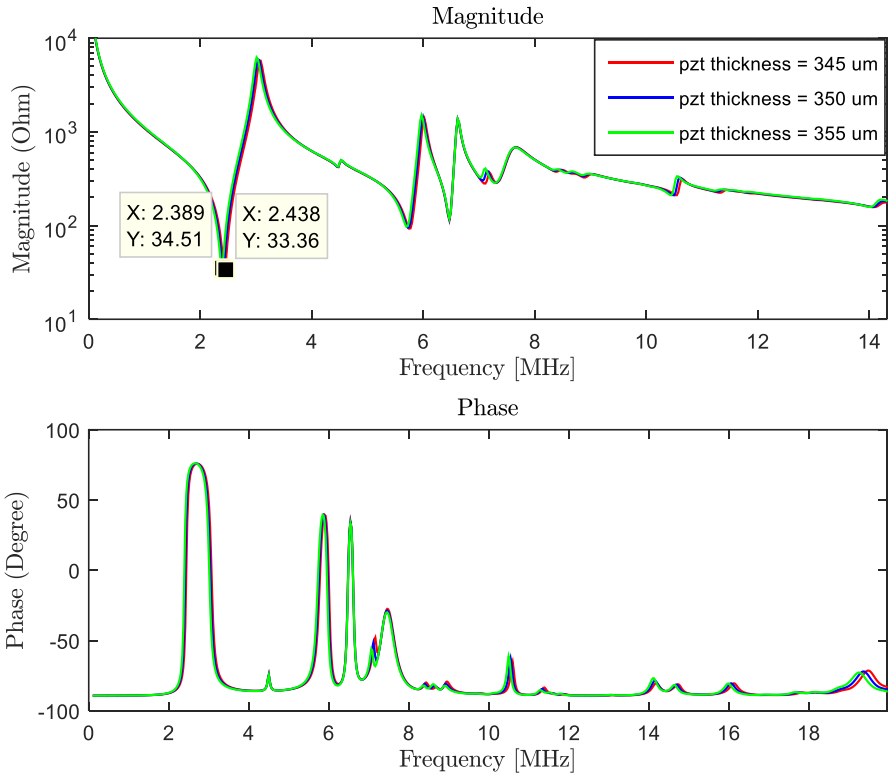


*Figure 4.46: FEM-simulations of electrical impedances with different PZT thickness*

#### 4.3.3.3 Thickness of intermetallic layer in SLID bondline

The initial thickness of electroplated gold layer in PZT and DML was around 10-11 µm.Thickness of preform Au-Sn foil was 25 µm. A total 36 µm SLID bondline was assumed. The intermetallic layer approximately differed from 22 µm to 30 µm (Figure 4.47). The remaining gold layer at both sides approximately varied from 7 µm to 3 µm. These parameters were inputed into COMSOL model to investigate the influence of intermetallic layer thickness on electrical impedance curve, assuming other parameters were kept the same.

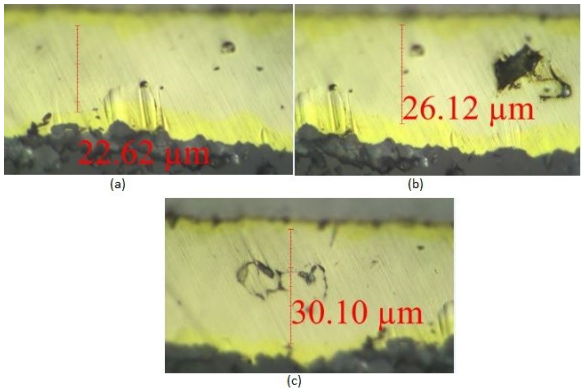


*Figure 4.47: Variance in thickness of intermetallic layer in SLID bond line*

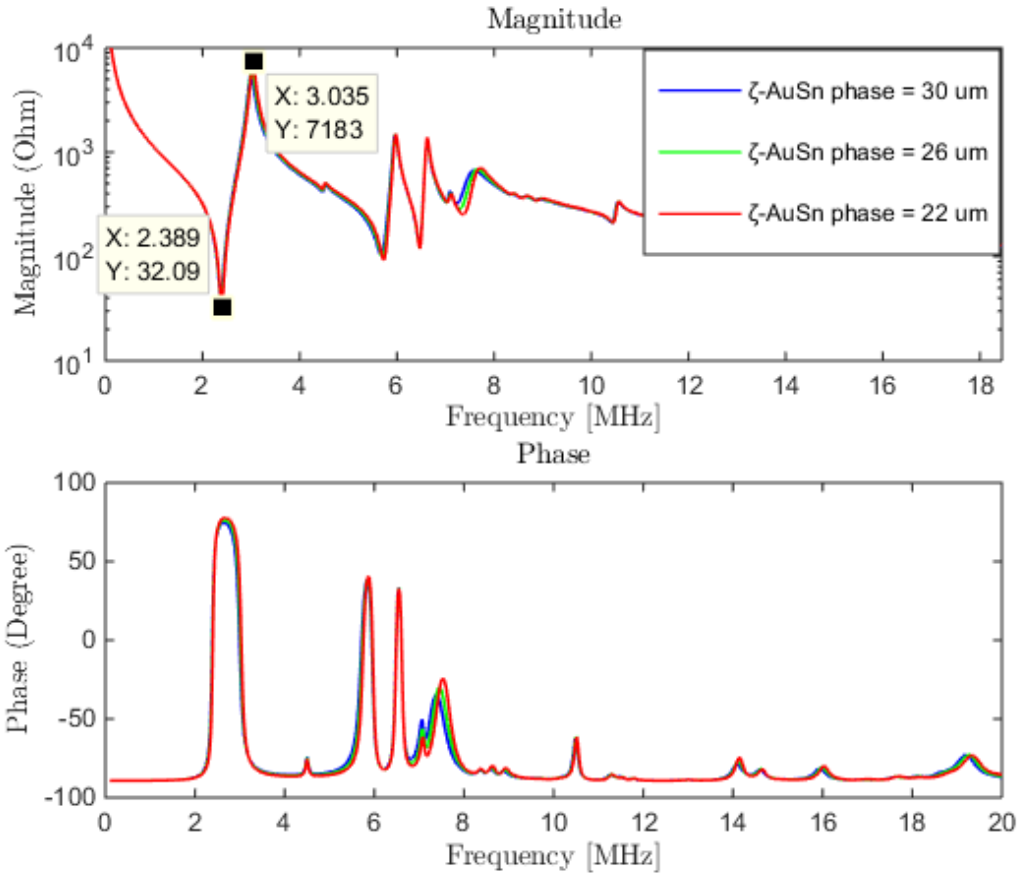


*Figure 4.48: FEM-simulations of electrical impedances with different thicknesses of intermetallic layer in SLID bond line*

Figure 4.48 shows electrical impedance curves with different intermetallic layer thicknesses. A similar method to calculate variance of 5 investigated cases was implemented as described in equations (3.8) (3.9). Table 4.19 summarizes variation at different vibrational modes. A slight variation in anti-resonance at thickness mode with thicker intermetallic (ζ-AuSn) layer. 2 % variance was seen at fourth vibrational mode. The intermetallic layer does not have effect on third vibrational mode.

*Table 4.19: The variance of resonance and anti-resonance frequencies at different vibrational modes due to intermetallic layer variation in SLID*

| Modes | $f_{rmax}$ (MHz) | $f_{rmin}$ (MHz) | Variance (%) | $f_{amax}$ (MHz) | $f_{amin}$ (MHz) | Variance (%) |
|---|---|---|---|---|---|---|
| TM | 2.39 | 2.39 | 0 | 3.04 | 2.99 | 1.6 |
| 2nd mode | 5.72 | 5.67 | 0.9 | 5.97 | 5.97 | 0 |
| 3rd mode | 6.47 | 6.47 | 0 | 6.62 | 6.62 | 0 |
| 4th mode | 7.36 | 7.24 | 2.0 | 7.71 | 7.59 | 1.6 |

#### 4.3.3.4 Voids inside SLID bond line

Different shapes of voids appear at different locations in the SLID bond line, mostly along the original bond interface or intermetallic layer (Figure 4.49, Figure 4.50). Voids were also reported in previous Cu-Sn SLID bonding method [30].

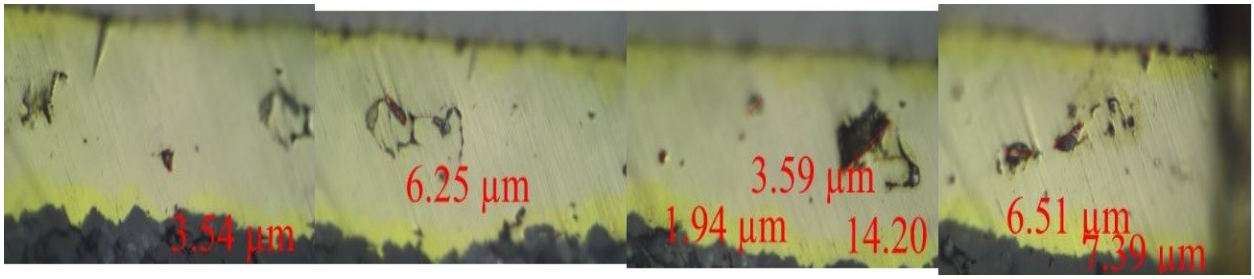


*Figure 4.49: Bond line with different shapes of void*

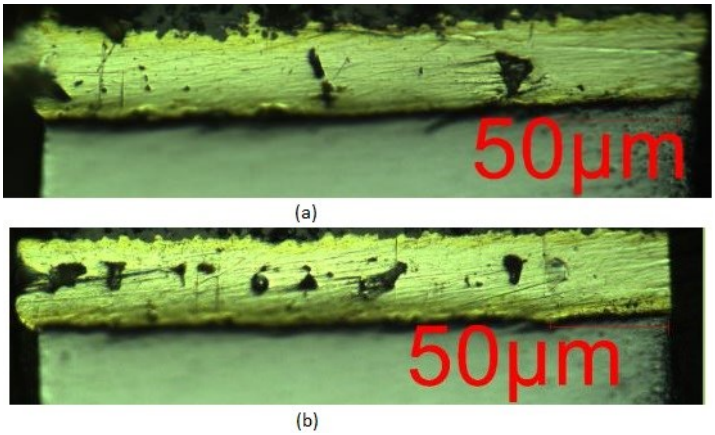


*Figure 4.50: Bond lines with different void fractions (a) 2.5 % void fraction (b) 10 % void fraction*

*Figure 4.51: Void analysis*

Bond line in Figure 4.49 had almost 5 % void fraction. Each array element possessed different void fractions, i.e (10% in Figure 4.50(b)). Therefore, we investigated the effect of void formation by assuming void fraction fluctuates from 2.5 % to 10 % in the original bond interface by using COMSOL simulations.

The variation in electrical impedances with different void fractions in the SLID bond line was recognized (Figure 4.52). Specifically, in the worst case, i.e. 10 % void fraction, almost 4% variance at anti-resonance of thickness mode and 5 % variance at resonance at second vibrational mode were observed.

Simulations show that voids in the SLID bondline shift the resonances to lower frequency and introduce higher loss compared to the intact SLID layer. The void fraction did not have large effect on third vibrational modes. A summary of variation at different vibrational modes are shown in Table 4.20.

*Table 4.20: The variance of resonance and anti-resonance frequencies at different vibrational modes due to void fractions in SLID bond line*

| Modes | $f_{rmax}$ (MHz) | $f_{rmin}$ (MHz) | Variance (%) | $f_{amax}$ (MHz) | $f_{amin}$ (MHz) | Variance (%) |
|---|---|---|---|---|---|---|
| TM | 2.389 | 2.339 | 2.1 | 3.035 | 2.936 | 3.3 |
| 2nd mode | 5.722 | 5.473 | 4.4 | 5.971 | 5.871 | 1.7 |
| 3rd mode | 6.468 | 6.468 | 0 | 6.617 | 6.617 | 0 |
| 4th mode | 7.264 | 7.165 | 1.4 | 7.662 | 7.413 | 3.2 |

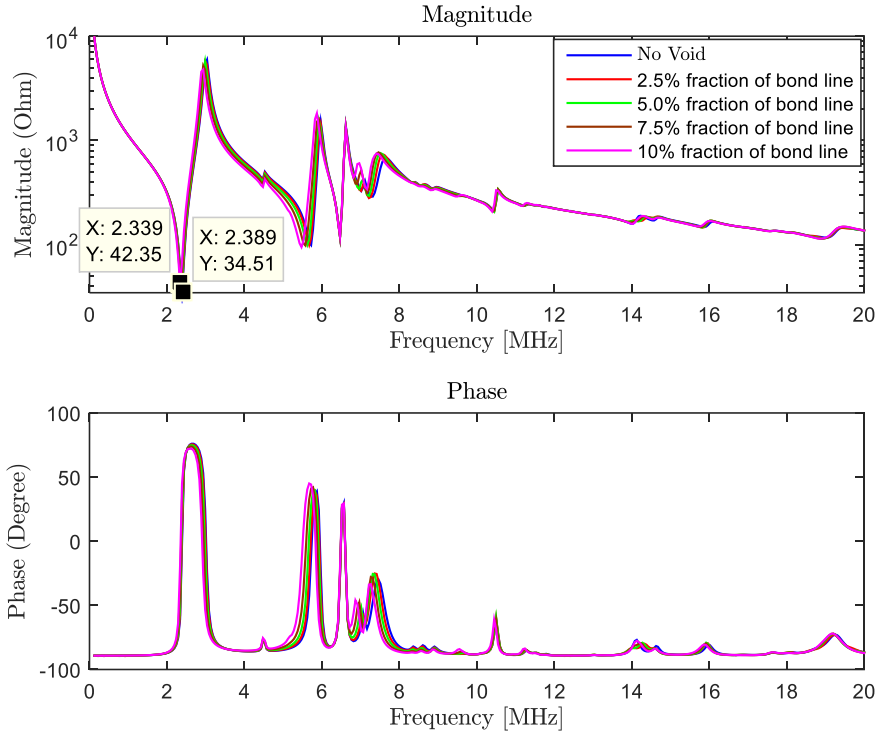


*Figure 4.52: FEM-simulations of electrical impedances with different void fractions in intermetallic bond line*

The amount of downshift in frequency at resonances and anti-resonances as a function of void fraction from 2.5 % to 10 % of the bond line compared to intact SLID bond line was shown in Figure 4.53. Interestingly, the larger the void fraction, the more downshift in resonances frequency.

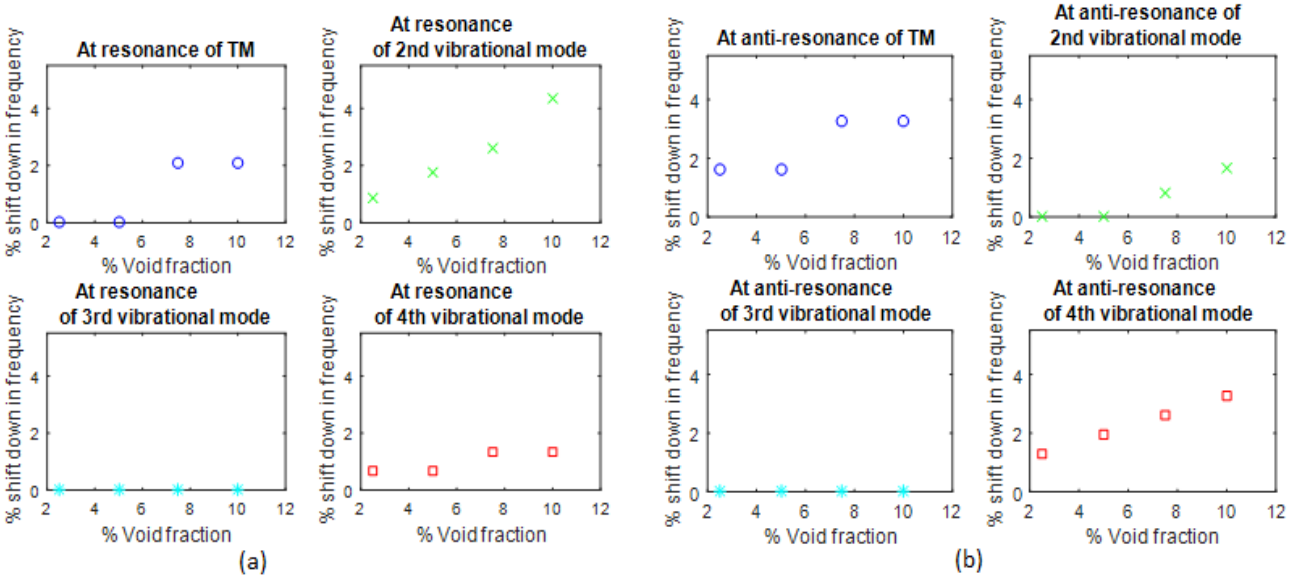


*Figure 4.53: % Shift down in frequency as a function of void fraction at resonance and anti-resonance of different modes*

### 4.3.4 Electrical characterization of array element in Epoxy bonding method

The linear array's impedance was measured in air with the network analyser HP8753D. The magnitude and phase of 59 elements are shown in Figure 4.54.

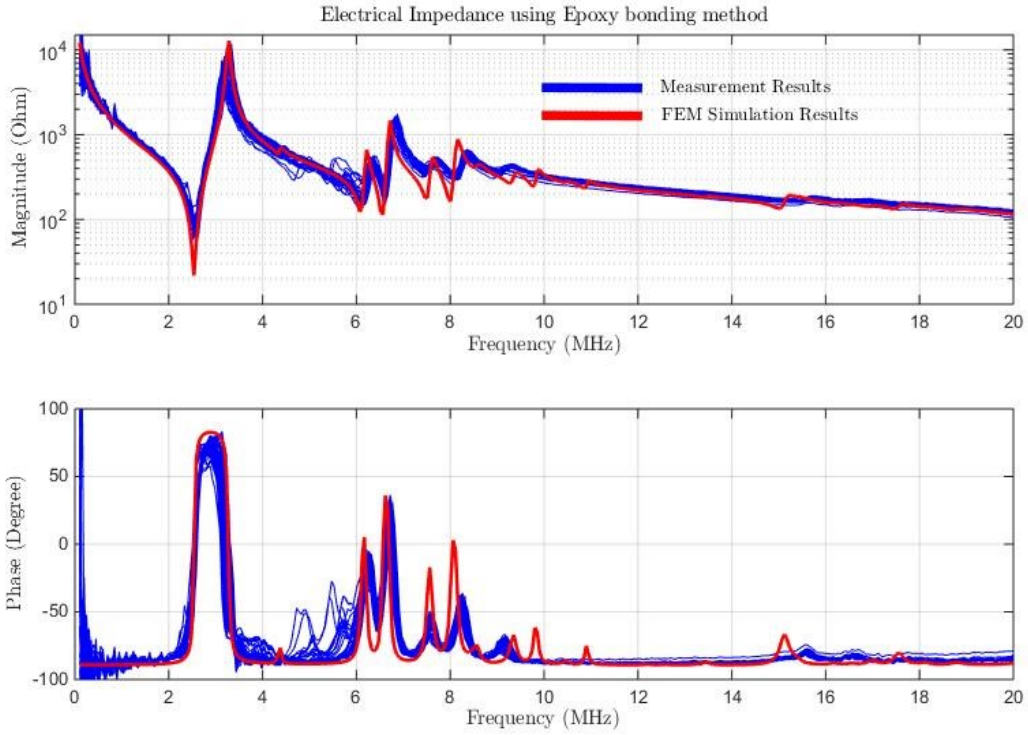


*Figure 4.54: Impedance response including magnitude and phase of 59 elements*

In the fabricated array, 5 of the elements showed an extra resonance peak around 4 MHz. This is the half-wavelength resonance frequency of the piezoelectric element alone, and a peak at this frequency is a clear sign of delamination between the piezoelectric element and the dematching layer. Hence, these elements are classified as error elements. The electrical impedances measured on these 5 error elements are shown in Figure 4.55.

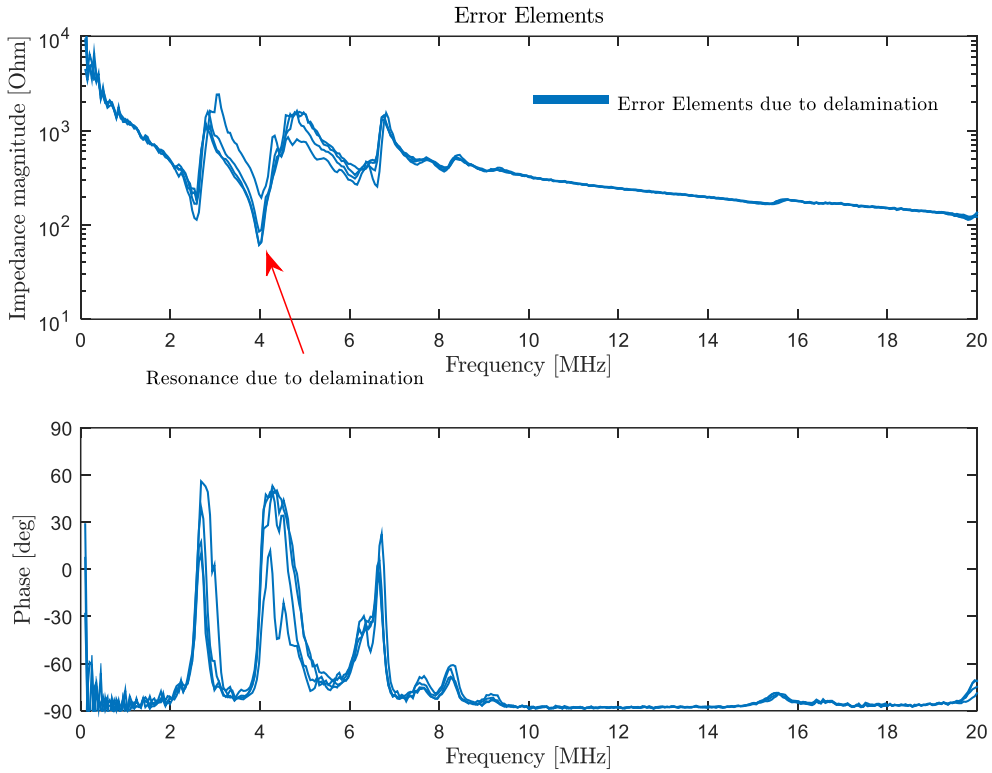


*Figure 4.55: Electrical impedance of 5 error array elements*

Figure 4.56 shows the interface between piezoelectric material thickness and WC substrate of the error elements. Delamination phenemenon happened, resulting in separation of the layers in the structure of these error elements. Therefore, a resonance at 4 MHz was observed.

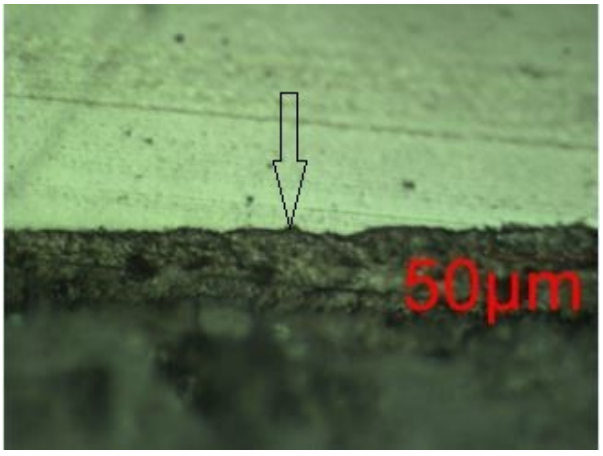


*Figure 4.56: Interface between PZT and WC of error elements*

All of the individual element test results for the array are summarized in Table 4.21.

*Table 4.21: Measured Properties for the 64-Element Array for Epoxy bonding method*

| Properties | Values |
|---|---|
| Number of elements | 64 |
| Number of open/shorted element | 0/0 |
| Number of error elements | 5 |
| Average resonance frequency at thickness mode | 2.55 MHz |
| Average anti-resonance frequency at thickness mode | 3.18 MHz |

There was also spread in electrical impedances at different frequency ranges. To better visualize these variations, the variance of resonance $f_r$ and anti-resonance $f_a$ frequencies at different vibrational modes were collected and plotted. Figure 4.57, Figure 4.58 and Figure 4.59 show the variation of resonance and anti-resonance frequencies of array elements at different vibrational modes, respectively.

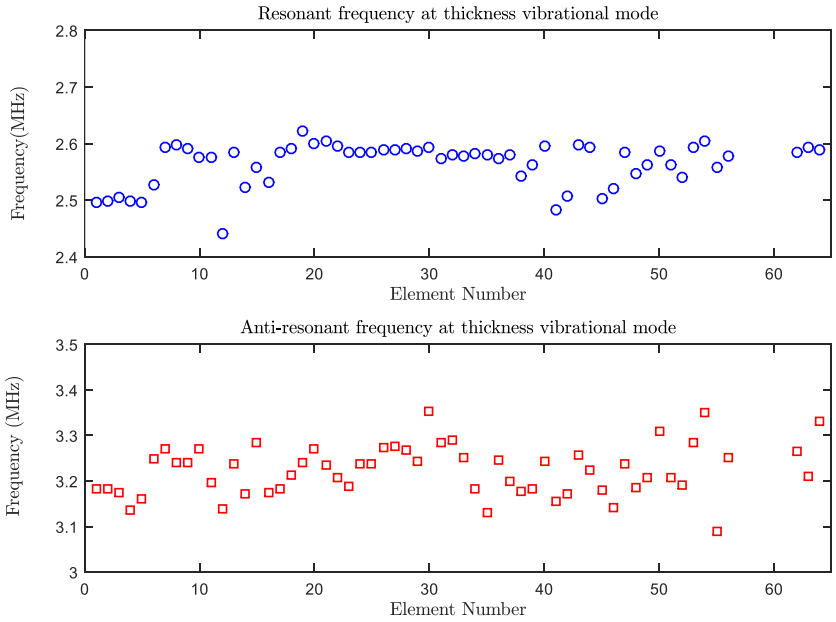


*Figure 4.57: The variation of resonance and anti-resonance frequencies at thickness vibration mode across the array*

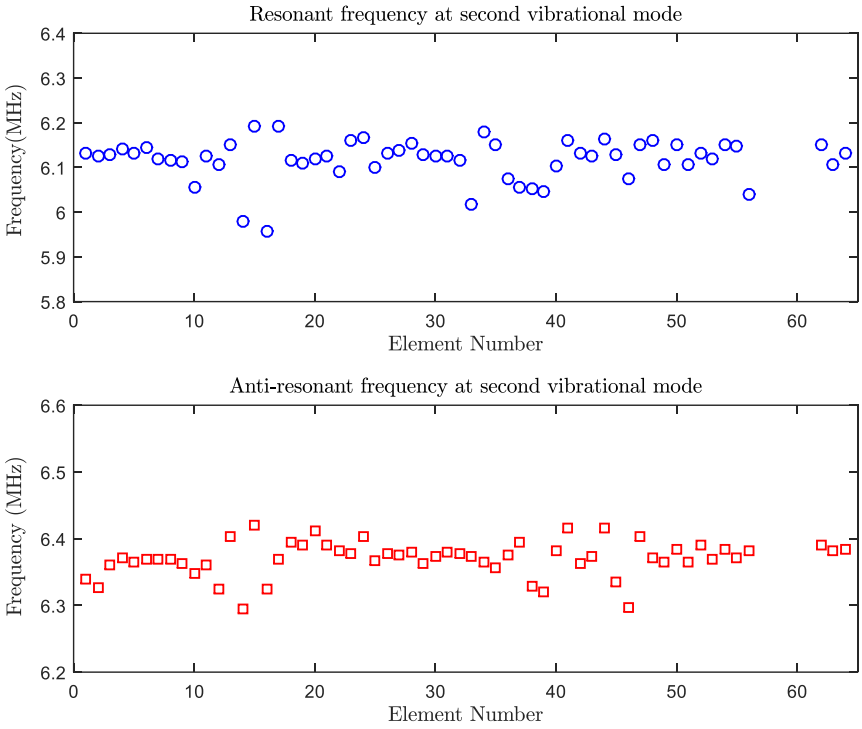


*Figure 4.58: The variation of resonant and anti-resonant frequencies at second vibrational mode across the array*

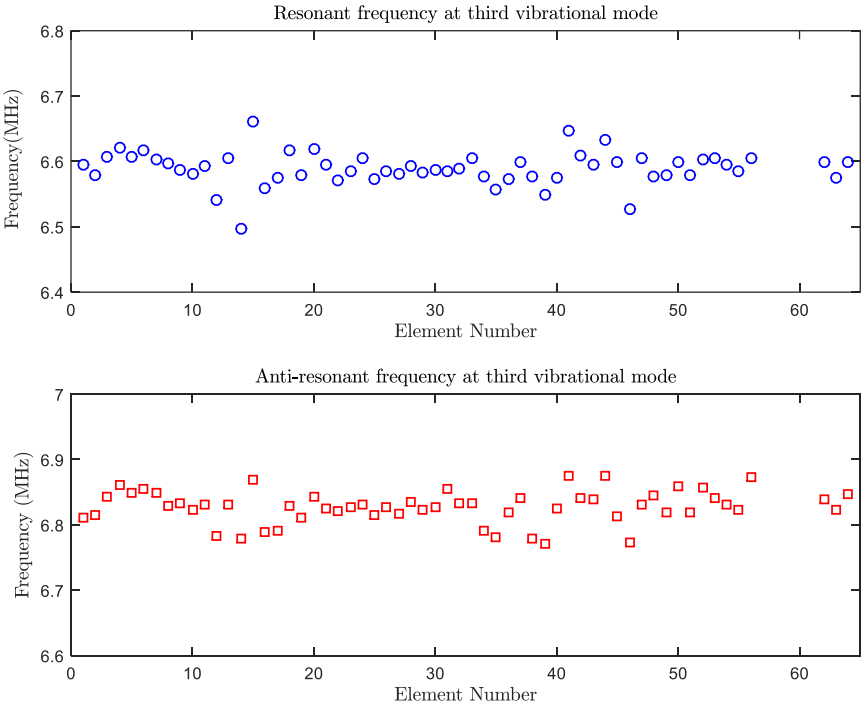


*Figure 4.59: The variation of resonant and anti-resonant frequencies at second vibrational mode across the array*

Table 4.22 summarizes the mean, standard deviation and coefficient of variation of resonance and anti-resonance frequencies at different vibrational modes.

*Table 4.22: Statistical analysis of resonance and anti-resonance frequencies at different vibrational modes*

| | $f_{r1}$ | $f_{a1}$ | $f_{r2}$ | $f_{a2}$ | $f_{r3}$ | $f_{a3}$ |
|---|---|---|---|---|---|---|
| Mean (MHz) | 2.55 | 3.22 | 6.12 | 6.37 | 6.59 | 6.83 |
| Std (MHz) | 0.04 | 0.05 | 0.05 | 0.03 | 0.03 | 0.03 |
| CV (%) | 1.56 | 1.55 | 0.82 | 0.47 | 0.46 | 0.44 |

The variance of resonance and anti-resonance frequencies at 3 different vibrational modes was summaried in Table 4.23.

*Table 4.23: The variance of resonance and anti-resonance frequencies at 3 different vibrational modes*

| Modes | $f_{rmax}$ (MHz) | $f_{rmin}$ (MHz) | Variance (%) | $f_{amax}$ (MHz) | $f_{amin}$ (MHz) | Variance (%) |
|---|---|---|---|---|---|---|
| TM | 2.62 | 2.44 | 6.9 | 3.35 | 3.09 | 7.8 |
| 2nd mode | 6.19 | 5.96 | 3.7 | 6.42 | 6.29 | 2.0 |
| 3rd mode | 6.66 | 6.50 | 2.4 | 6.92 | 6.77 | 2.2 |

### 4.3.5 Parameters causing variation in electrical impedance in Epoxy bonding method

#### 4.3.5.1 Element width

Figure 4.60 and Table 4.24 show the results of the element width and standard deviation measurements of fabricated array elements. Array element widths were seen to differ by only 5 µm.

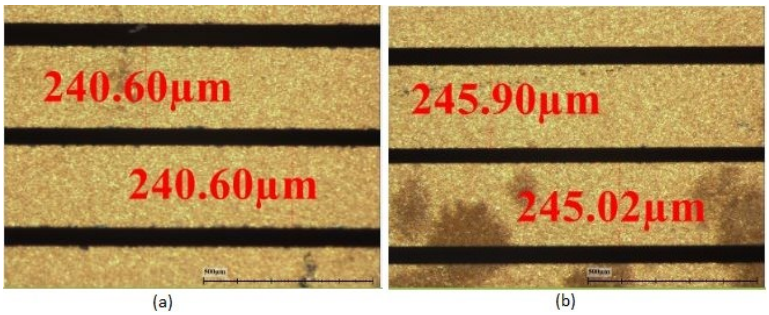


*Figure 4.60: Element width variance (a) 240 um (b) 245 um*

*Table 4.24: Element width measurements for array elements*

| | | |
|---|---|---|
| Element width (μm) | 240.5 | 245.3 |
| Element width σ (μm) | 0.9 | 0.8 |

Figure 4.61 shows COMSOL simulation results with 3 different element width parameters. Overall, element width factor was seen to create almost 3 % variation at second, third vibrational modes.

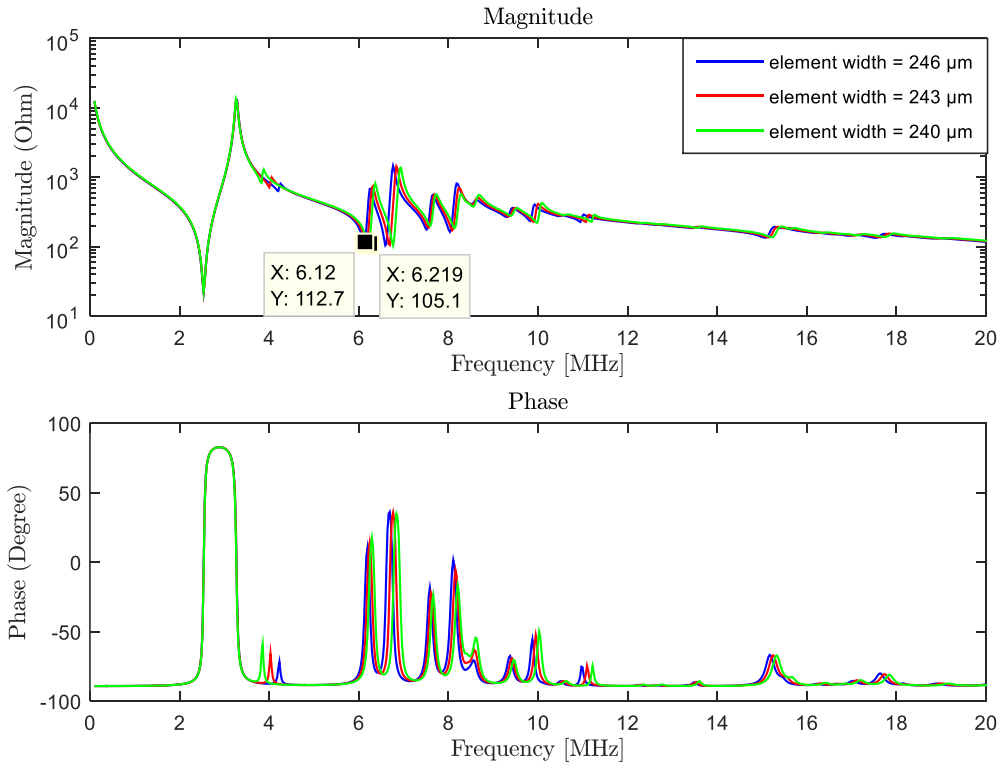


*Figure 4.61: FEM-simulations of electrical impedances with different element widths*

Table 4.25 numerically demonstrated the influence of element width variation at 3 vibrational modes on electrical impedance curves.

*Table 4.25: The variance of resonance and anti-resonance frequencies at 3 vibrational modes due to piezoelectric material thickness variation*

| Modes | $f_{rmax}$ (MHz) | $f_{rmin}$ (MHz) | Variance (%) | $f_{amax}$ (MHz) | $f_{amin}$ (MHz) | Variance (%) |
|---|---|---|---|---|---|---|
| TM | 2.54 | 2.54 | 0 | 3.26 | 3.26 | 0 |
| 2nd mode | 6.22 | 6.12 | 1.6 | 6.37 | 6.24 | 2.0 |
| 3rd mode | 6.77 | 6.60 | 2.5 | 6.94 | 6.77 | 2.5 |

#### 4.3.5.2 Piezoelectric material thickness

Variation in piezoelectric material thickness was seen under optical microscopy (Figure 4.62)

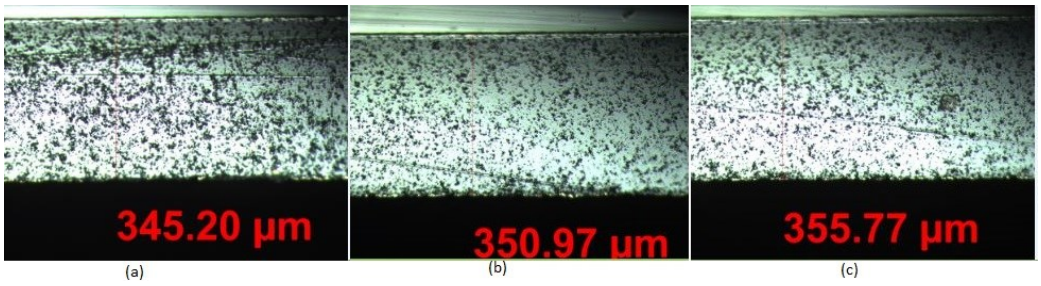


*Figure 4.62: Element width variance (a) 345 µm (b) 350 µm (c) 355 µm*

The piezoelectric material thickness and standard deviation measurements of fabricated array elements were shown in Table 4.26. PZT thickness between elements was seen to differ by 10 µm.

*Table 4.26: PZT thickness measurements for array elements*

| | | | |
|---|---|---|---|
| PZT thickness (µm) | 345.4 | 351.1 | 355.3 |
| PZT thickness σ (µm) | 0.7 | 0.7 | 0.45 |

COMSOL simulation results with 3 different piezoelectric material thickness parameters were plotted in Figure 4.63. Overall, PZT thickness factor was seen to create almost 2 % variation at thickness vibrational modes (Table 4.27).

*Table 4.27: The variance of resonance and anti-resonance frequencies at 3 vibrational modes due to piezoelectric material thickness variation*

| Modes | $f_{rmax}$ (MHz) | $f_{rmin}$ (MHz) | Variance (%) | $f_{amax}$ (MHz) | $f_{amin}$ (MHz) | Variance (%) |
|---|---|---|---|---|---|---|
| TM | 2.59 | 2.54 | 2 | 3.33 | 3.28 | 1.5 |
| 2nd mode | 6.15 | 6.10 | 0.8 | 6.27 | 6.22 | 0.8 |
| 3rd mode | 6.54 | 6.54 | 0 | 6.54 | 6.54 | 0 |

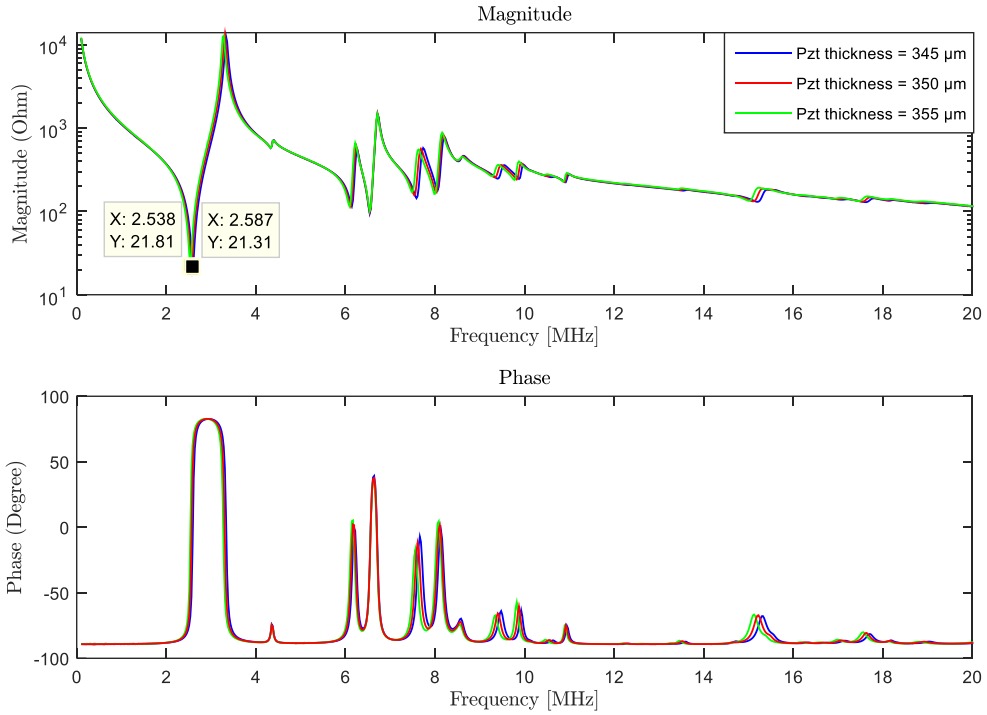


*Figure 4.63: FEM-simulations of electrical impedances with different piezoelectric material thicknesses*

#### 4.3.5.3 Epoxy bond line thickness

Variation in epoxy bond line thickness between piezoelectric material and WC substrate was seen under optical microscopy (Figure 4.64).

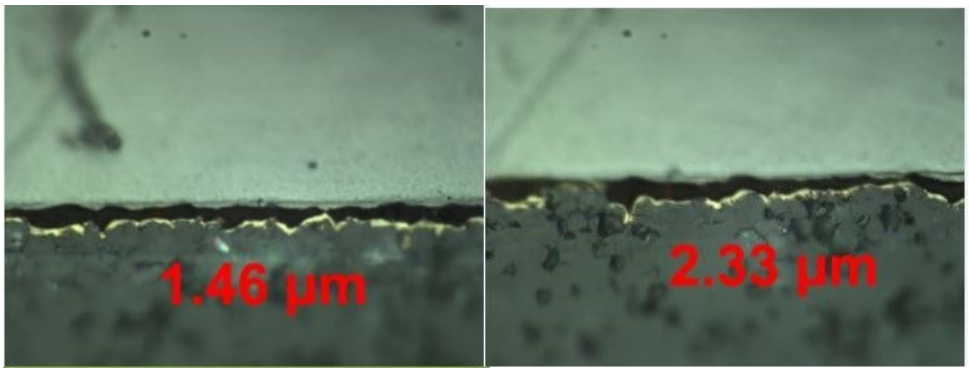


*Figure 4.64: Epoxy bond line variation between PZT and WC*

COMSOL simulations with 3 different epoxy thickness parameters was investigated in Figure 4.65. Overall, epoxy bond line thickness factor was observed to generate almost 5 % variation at thickness vibrational modes (Table 4.28).

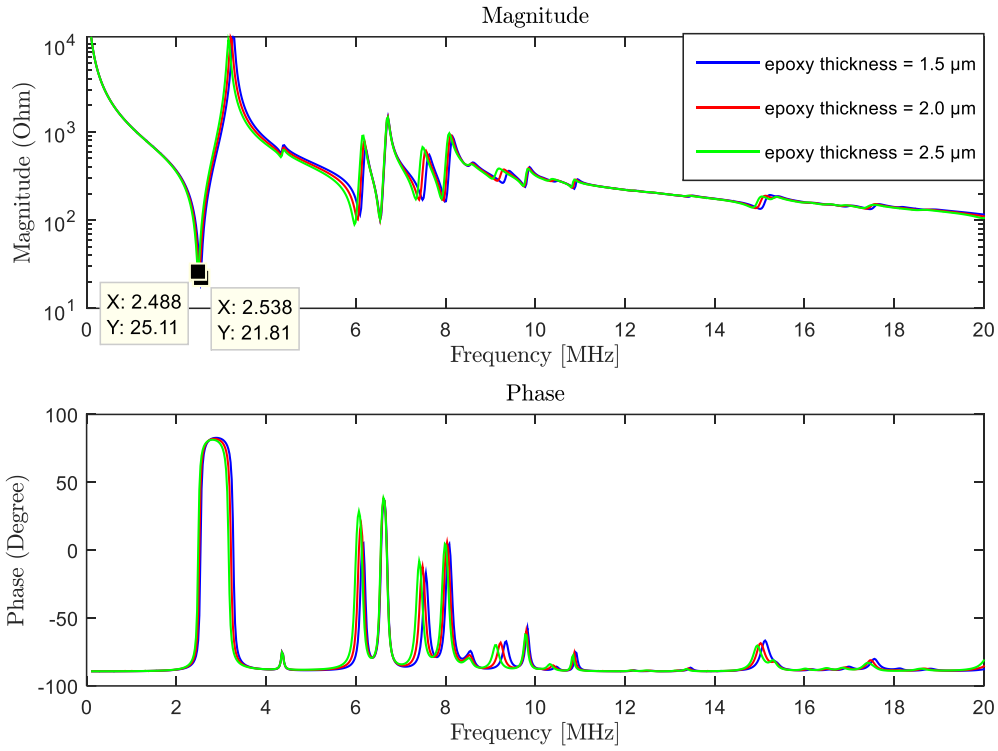


*Figure 4.65: FEM-simulations of electrical impedance with different epoxy bond line thicknesses*

*Table 4.28: The variance of resonance and anti-resonance frequencies at 3 vibration mode due to epoxy thickness variance*

| Modes | $f_{rmax}$ (MHz) | $f_{rmin}$ (MHz) | Variance (%) | $f_{amax}$ (MHz) | $f_{amin}$ (MHz) | Variance (%) |
|---|---|---|---|---|---|---|
| TM | 2.54 | 2.49 | 2.0 | 3.29 | 3.16 | 4.0 |
| 2nd mode | 6.10 | 5.97 | 2.1 | 6.22 | 6.17 | 0.8 |
| 3rd mode | 6.54 | 6.54 | 0 | 6.72 | 6.72 | 0 |

### 4.3.6 Comparison between SLID and epoxy bonding methods

Overall, the impedance response of the transducer using SLID and conventional epoxy bonding method showed similar results. Variation of electrical impedance responses was present in both cases being investigated. The transducer shifted down a little more at thickness vibration mode in SLID bonding method than in epoxy bonding method when intermetallic layers was present between PZT and WC. However, the SLID bondline can be ten times thicker than conventional epoxy bondline for nearly the same amount of frequency shift. In addition, the epoxy's bondline thickness must be substantially small compared to the sound wavelength. For transducers operating at frequencies above, the desirable thickness and thickness uniformity of the bonding epoxy layer is difficult to

achieve. Direct casting method often be used in these cases [13]. Suppose that the requirement of epoxy bond line thickness was not well achieved in fabrication process. A comparison betwwen SLID and epoxy bonding method with different bonding layer thicknesses was shown in Figure 4.66 and Figure 4.67.

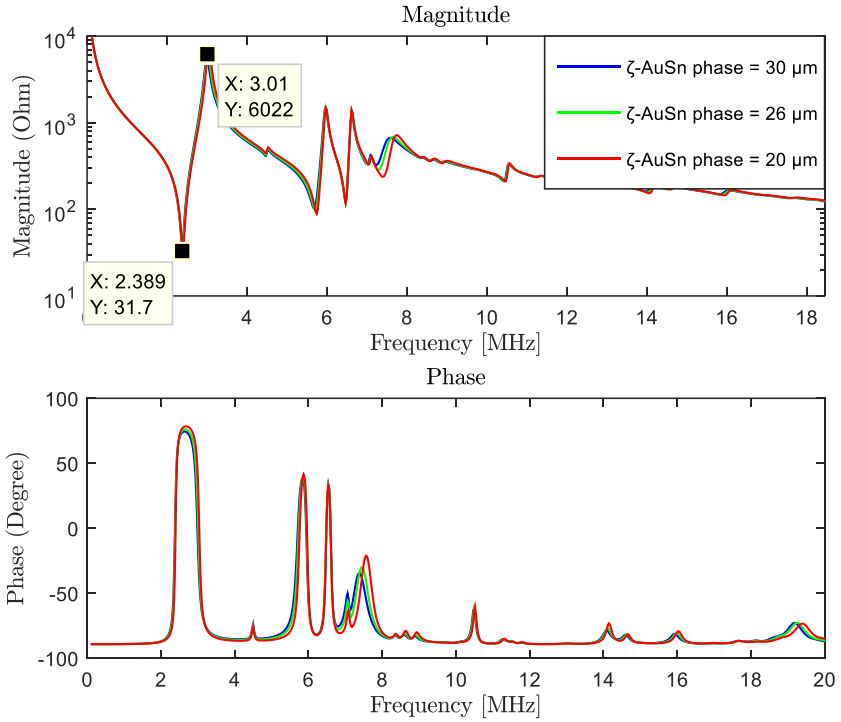


*Figure 4.66: FEM-simulations of electrical impedance with different intermetallic layer thicknesses*

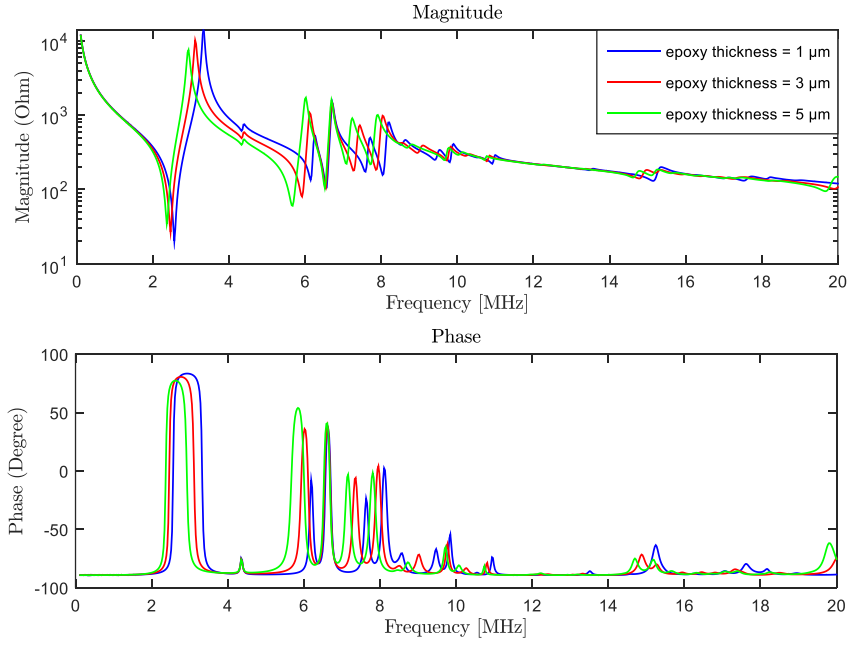


*Figure 4.67: FEM-simulations of electrical impedance with different epoxy layer thicknesses*

The most remarkable result is that in epoxy bonding technique, electrical impedances vary significantly with a small amount of variation in bondline. However, in SLID bonding technique, not measurable variation was observed even when thickness uniformity of intermetallic bondline changes greatly.

Based on these results, a more comprehensive comparison between SLID and epoxy bonding methods is illustrated in Table 4.29.

*Table 4.29: Comparison between SLID and epoxy bonding methods*

| Criteria | SLID | Epoxy |
|---|---|---|
| Time | < 1 hour | 3 hours |
| Temperature | $300^0$ C | $60^0$ C |
| Thickness and uniformity | Thickness requirement is relaxed | Small compared to sound wavelength |
| Acoustic Impedance | Z ~ 33 (MRayl) | Z ~ 3 (MRayl) |

# CHAPTER 5. Discussion

This chapter consists of three sections. Firstly, section 5.1 discusses the results of single-element transducers. Secondly, section 5.2 discusses the electrical impedance variation in one-dimensional linear array ultrasonic transducer. Measurement and FEM simulation results are compared. Finally, section 5.3 discusses variance in electrical impedance of piezoelectric linear array ultrasonic transducer using different bonding methods: SLID and conventional epoxy. A comparison between these two bonding method are also described in depth.

## 5.1 Single Element Transducers

Our results show that the experimental measurement of electrical impedance agrees fairly well with both simulations (1D and 2D). The 1D model is valid because the transducer's diameter is much larger than its thickness. The variation in matching layer thickness also generates small difference in electrical impedances between measurement and modelling results. The actual thickness variation of the matching layer in transducer Type I is more than that of Type II. Therefore, it could be one of the possible reasons that its bandwidth is a little smaller than that of Type II transducer. In addition, the electrical impedance of transducer Type II is better matched to the input impedance of transmitting and receiving electronics compared to that of Type I. In addition, these in-house transducers had high sensitivity because using air-backing.

## 5.2 One-Dimensional Linear array ultrasonic transducer

### 5.2.1 Find fitted material data for Pz27 used in Comsol 2D Simulation

Our result indicates that the pz27 material data given by the manufacturer are not sufficiently accurate enough to simulate the performance of our transducers. The first material data [24] were extracted from measurement results of piezoelectric transducer disks operating at thickness mode approximately 1 MHz. The second material data [25] were used to simulate disk transducer operating at frequency lower than 1 MHz. These datasets were characterized at frequency four times lower than our transducer performance frequency; therefore, poor agreement between simulation and measurement results were expected.

The third material data [9] were characterized at 4.78 MHz fundamental antiresonance frequency that was comparable to our transducer design. In addition, this study was

performed on a large number of samples. Therefore, we regard this as the most accurate dataset for our simulations.

### 5.2.2 Mesh independend study

The result of mesh independent study shown in Figure 4.10 provides an appropriate mesh size that will be used for all COMSOL simulations. An inconsiderable difference in electrical impedance curves was observed in these simulations.

### 5.2.3 Electrical characterization of linear transducer array

Our overall results suggest that the close agreement between simulation and measurements strongly confirms the validity of our simulation process. Various variation between array elements is expected. As shown in Figure 4.15, the range of imperfect elements is from element 15 to element 22 with a decrease in magnitude at anti-resonance and an increase in magnitude at resonance. The rest follows a general trend with a little bit variation. The reasons and influence of these variations will be discussed in depth in the following sections.

### 5.2.4 Parameters causing variation in Electrical Impedances

#### 5.2.4.1 Element width

Our finding confirms that variation in element width may origin from vibration of dicing saw blade operating at different revolution speeds [31]. This variation causes downshift at frequency around 6.1 MHz because width-extensional resonant mode is present at that frequency (Figure 4.20). This phenomenon makes perfect sense because element width is inversely proportional to resonance frequency at this mode. Element width has no large effect on thickness vibration mode.

#### 5.2.4.2 Kerf Shape

The observed variations in kerf shape were found to have less than 1% influence on the electrical impedance. These results support the idea that kerf shape has minor effect on piezoelectric performance. Therefore, this factor is not the main reason causing variation in electrical impedance.

#### 5.2.4.3 Piezoelectric material thickness

Our results support classical theory that piezoelectric material thickness is inversely proportional to resonance frequency at thickness mode. This factor is the primary reason creating variation in resonances at main thickness extention mode.

#### 5.2.4.4 Electrode thickness

Our results confirm that variation in electrode thickness creates shift down in frequency at thickness mode. This can be explained due to mass loading effect. General speaking, adding mass to the piezoelectic material surface provides a convenient means of frequency adjustment. Sherar and Foster also showed the mass-loading effects of sputtered gold electroding on 9 μm thick PVDF [32]. L.F. Brown [33] also presented the same result. These results confirm that the electrode thickness can have a measurable impact on transducer performance.

#### 5.2.4.5 Material properties changes

Our finding suggests that the origin of this phenomenon could be due to change of material properties of small regions at both side of array element [26]. Specifically, loss values at this region were changed due to local heating of the piezoelectric material during the dicing.

During dicing step, friction between diamond blade and material generates heat. The dicing blade fill the kerf in addition to a thin layer of water coolant and debris. Small differences in the electrical properties are created due to thermal asymmetry of the dicing process. Particularly, on the left side of the kerf, heat is conducted to a single element while the heat is conducted to the rest un-diced piezoelectric material. Specifically, the dicing process creates piezoelectric a few micrometers thick dead zone of a single element, resulting in thermal and mechanical damage. These damaged zones have a negative impact on the array performance. As shown in Table 3.2, these imperfect elements was cut with high revolution speed 30000 rpm, so much more severe thermal and mechanical damage may be generated compared to other elements.

Both the effects of mechanical loss and dielectric loss were investigated (Figure 4.27, Figure 4.29). For the mechanical loss, peaks change simultaneously and get wider with the increase of the losses. This is the classical result that low-Q (high mechanical loss) presents wide peaks. The effect of the dielectric losses is significantly observed only at the anti-resonance. With the increase of the dielectric losses, anti-resonance gets lower value of the Q-factor.

Some elements in the array having large impedance at resonance makes electrical matching the element to the transmitting and receiving electronics of the imaging system

very challenging. To avoid this problem, it is highly recommended that we should operate the dicing saw at around 20000 rpm.

The variation in magnitude at resonance and anti-resonance may be solely caused by modification in mechanical loss or dielectric loss or both. There may be influence of piezoelectric loss that we have not fully investigated. Loss mechanism is a difficult topic that needs more time and effort to study.

#### 5.2.4.6 Debris inside the kerf

Our findings suggest that debris inside the kerfs may cause the occurrence of spurious mode. The phase at spurious mode has two peaks. Occurrence of spurious mode was also described in piezoelectric ceramics resonator [34], [35]. There may be other potential reasons that create spurious mode that we could not know.

Fewer spurious resonance is highly recommended for transducer performance. It means that less mechanical interference generates a cleaner electrical signal. Therefore, to avoid excitation of spurious responses, we should use higher water flow during dicing step to clean the diamond blade or cleaning sample to wash away the debris.

## 5.3 Piezoelectric linear array ultrasonic transducer using different bonding methods

### 5.3.1 Intermetallic layer property in SLID bond line and mesh independent study

A trivial discrepancy at fourth vibrational mode in electrical impedance curves was observed for three different intermetallic layer property in SLID bond line. It means that this factor does not have a significant impact on altering electrical impedance of array elements in the transducer. Mesh independent study was also performed to choose the most approximate mesh size for the rest of simulations.

### 5.3.2 Electrical characterization of array element in SLID bonding method

Our results shown in Figure 4.36, Figure 4.37, Figure 4.38 confirm a significant spread in electrical impedance curve of each array element that is similar to the finding conducted by Marc Lukacs [36]. Certainly, SLID bonding method used in our fabrication process is the primary different from previous researches. The difference in the sharpness of the resonant peaks between the experimental curves and the simulation curve is due to the fact that in the FEM simulation, the electrical and mechanical losses of materials that were used in the design were not exactly characterized. Small discrepancy between simulation and

experimental results may be due to unknown material property of the intermetallic bond line such as loss, longitudinal velocity parameters.

Table 4.12 suggests that all array elements were well fabricated. The repeatability and stability of this transducer array are highly consistent across the array. Variation in resonace and anti-resonance at different vibrational modes of array elements presented in Figure 4.39, Figure 4.40, Figure 4.41, Figure 4.42 is expected. What are the primary reasons that generate these deviations in electrical impedance curves ? Where do these sources come from ? To answer these questions, Finite Element simulations by COMSOL utilized to investigate these factors will be thoroughly presented in the next sections.

The variance in magnitude at resonant and anti-resonant frequencies of thickness mode can be attributed to different losses of each array elements, i.e. mechanical, dielectric and electromechanical losses. Specially, loss mechanism of SLID bondline may also contributes to these deviations.

Although we assumed a ζ-AuSn phase in the intermetallic SLID bond line, this still created a small mismatch between simulation and measurement results at resonance of third vibrational mode. Future research should concentrate on extensively characterizing SLID bond line and its related properties to input to COMSOL model.

### 5.3.3 Parameters causing variations in electrical impedance in SLID bonding method

One of the main goals of this experiment was to attempt to find variance between array elements. Each factor that contributed to variation in electrical impedance will be thoroughly discussed along with result sections.

#### 5.3.3.1 Element Width

Our results presented in Figure 4.43 indicate that the width of a single array element approximately differs from 245 µm to 255 µm. This can be explained due to vibration from hubless-blade type used in dicing step.

The difference in element width generates variation at second, third and fourth vibrational modes (Figure 4.44). With larger element width, the positions of resonant peaks shift down in frequency. The observed variations in element width were found to have no measurable influence at thickness mode. It means that element width has effect at frequency

range higher than the thickness resonant frequency. This trend also agrees with the case transducer array using only piezoelectric material described in section 5.2.4.1.

#### 5.3.3.2 Piezoelectric material thickness

Variance in PZT thickness also contributes to variation in electrical impedance of array elements. Our results confirm that piezoelectric material thickness variance has primary influence in thickness vibration mode. The resonances of this mode shift down in frequency with thicker piezoelectric material thickness. The thickness of piezoelectric material is mainly related to thickness resonance mode [29]. Therefore, a significant variation is observed at that mode.

#### 5.3.3.3 Thickness of intermetallic layer in SLID bondline

Our findings indicate that the reaction between gold and Au-Sn preform during SLID bonding procedure were not uniform; therefore, thickness of intermetallic layer in SLID bond line varied slightly from element to element. However, this variation did not create large spread at thickness mode (Figure 4.48). These observations provide compelling evidence that the requirements of both bondline thickness and uniformity are substantially relaxed when bonding stacks of piezoelectric ultrasonic transducers using SLID bonding method. To date no work has been published on SLID bonding method on transducers, their use as novel bonding technique could be a breakthrough in piezoelectric ultrasonic transducers fabrication.

#### 5.3.3.4 Void inside SLID bondline

Our results confirm that voids in SLID bond line shift the resonances to lower frequency and introduce higher loss compared to the intact SLID layer. The amount of variation of the resonances and anti-resonances is proportional to increasing void fraction in the bond line. This overall trend is clearly seen at thickness, second and fourth vibrational modes. These findings provide a substantial insight of void fraction effect on electrical impedance of piezoelectric transducer.

It appears that we only investigated several cases of void fraction using 2D COMSOL model. A greater number characterization of samples could lead to a higher generalization of our results. To more accurately characterize void effect in performance of piezoelectric transducer, more experiments on void shapes effect should be conducted. In addition, future research should optimize parameters in SLID bonding process in order to minimize void formation in the bond line.

There may be other unexplored reasons that generate variation across 64 array elements such as material properties of SLID bond line, loss mechanism, etc. Using 2D COMSOL simulations, we only can investigate possible sources that contribute to these variances. In order to precisely inspect other reasons, it is absolutely important to fully characterize the properties of SLID bond line. This task requires comprehensive knowledge of material science field, especially SLID method.

### 5.3.4 Electrical characterization of array element in Epoxy bonding method

Our results shown in Figure 4.54 indicate indisputable variation in electrical impedance curves at different frequency ranges. Resonance and anti-resonance at thickness mode varied the most compared to other vibrational modes. Discrepancy between measurement and simulation results at fourth and fifth peaks may come from thickness uniformity of epoxy bond line.

Some elements had small peaks at frequency range 4 MHz - 6 MHz. It appears that imperfection in fabrication process caused this phenemenon. Although 5 error elements (element 57-61) were recognized in the array, Table 4.21 suggests that the array elements were fairly fabricated. The repeatability and stability of this linear transducer array are up to 95 %. The origin of these error elements comes from the delamination phenomenon in the bonding process between WC and piezoelectric material (Figure 4.56). A resonance at 4 MHz is due to delamination. Therefore, we need to pay close attention to thickness uniformity of epoxy bond line to avoid this problem in fabrication process.

Variation in resonace and anti-resonance at three different vibrational modes of array elements presented in Figure 4.57, Figure 4.58, and Figure 4.59 is expected. Sources generating this variance may be geometric difference of components in the fabricated structure such as element width, piezoelectric material thickness. These factors will be discussed completely in the next sections.

These results will be compared to that of SLID bonding method in the next section to explore what are the main advantages and disadvantages of these 2 methods.

### 5.3.5 Parameters causing variation in electrical impedance in Epoxy bonding method

Variations in electrical impedance were observed in the result section. Each factor that contributed to these variations in electrical impedance will be discussed in the next sections.

#### 5.3.5.1 Element Width

Our results presented in Figure 4.61 indicate that the width of a single array element approximately differed by only 5 μm. This variation was less than that for SLID sample because the hub-blade type was used in the dicing step.

The variance in element width also generated similar variation at vibrational modes, excluding thickness mode. The positions of resonant peaks shift down in frequency as element width is wider. It means that element width has effect at frequency range higher than the thickness resonant frequency. This result follows the trend of SLID sample's.

#### 5.3.5.2 Piezoelectric material thickness

Variance in PZT thickness also contributes to variation in electrical impedance of array elements. Our data confirms that the resonances of thickness mode shift down in frequency with thicker piezoelectric material thickness. This observation also agrees with SLID sample's.

#### 5.3.5.3 Epoxy bond line thickness

Our results suggest that epoxy bonding layer thickness and uniformity affect the transducer performance. A downshift in frequency at thickness mode is contributed to thickness uniformity of bonding layer. In addition, a desirable thickness is also difficult to achieve because delamination often occur when bonding a piezoelectric material to a backing substrate with very small surface roughness. L.F. Brown [33] also described the bonding process between an active polymer film to a high impedance backing at high frequency, the result was typically a transducer whose resonant frequency was unexplainably lower than anticipated due to the effects of the adhesive layer. Therefore, desirable thickness and thickness uniformity of epoxy bond line should greatly be taken into account when bonding these materials.

It appears that we can not investigate all possible thickness uniformity. However, the effect of epoxy bond line on electrical impedance has been pointed out with FEM simulations.

### 5.3.6 Comparison between SLID and epoxy bonding methods

Our results show how SLID bonding method can provide advantages over conventional epoxy bonding. Almost the same average resonances were observed at two transducers at 2.44 MHz and 2.55 MHz for SLID and epoxy bonding method, respectively. We can control SLID bond line thickness to reduce the downshift in frequency.

While SLID bonding method only requires less than 1 hour at 300 $^0$C to perform, epoxy bonding method is more time-consuming with 3 hours at 60$^0$C to get desired bond line. Although one additional step,i.e. repoling the sample, needs to be conducted after bonding, the bonding time for SLID is still less than that for epoxy.

Desirable thickness and thickness uniformity of the bondline are not strickly required for SLID bonding method. However, these conditions must be highly recommended for epoxy, especially for transducer working at high frequencies. No measurable variation at resonances was observed at different intermetallic thickness, while a significant variance at resonances was detected for thick epoxy bond line (Figure 4.66 and Figure 4.67). However, voids inside SLID bondline is also a challenging problem that we need to solve.

In addition, SLID produces a bond layer including intermetallics with acoustic impedance better matched to the impedances of the substrates compared to epoxy. That is an advantage of SLID to epoxy bonding method. SLID method is novel and still not fully mature and needs to be improved in the future. It appears that we still have not fabricated a complete transducer with matching and backing layer using SLID bonding method. However, these electrical impedance results shows that feasibility of adopting a potentially novel bonding technique to assembly stacks of piezoelectric ultrasonic transducers.

# CHAPTER 6. Conclusion

## 6.1 Thesis contribution

In this thesis, the variance in linear transducer array using only piezoelectric material was fabricated and characterized. Different sources of variance such as element width, piezoelectric material thickness, electrode thickness, material properites change due to heating effect and spurious modes were compresensively characterized and compared to FEM simulations. Specifically, element width variance from 244 μm to 260 μm was found to create a 5% downward shift of the width extensional mode. The observed variations in kerf shape was found to have less than 1% influence on the electrical impedance. A 3% shift in frequency from the resonant (2.81 MHz) to the anti-resonant frequency (3.54 MHz) could be attributed to thickness variations in the piezoelectric plate, from 483 μm to 498 μm. Electrode thickness variations from 18 μm to 22 μm resulted in around 2% shift in the resonance region. Debris inside the kerfs may cause spurious modes, and thereby influence the main thickness extension mode. Material property changes were identified as the main source of the impedance variations, causing a decrease of nearly 50% in magnitude at the anti-resonant frequency, and an increase of 160% to 200% at the resonant frequency.

Two single-elements transducer using two different matching layer materials were also fabricated and characterized by pulse-echo response to estimate the transducers' performance. Both 1D, 2D FEM simuations and fabrication were carried out in this experiment. The -6dB bandwidth of the fabricated single-element transducers was 44 % (Type I) and 49% (Typpe 2), respectively. Transmitting sensitivities were 0.5146 m/(sA) and 0.6 m/(sA) for Type I and Type II transducers, respectively.

A different transducer structure consisting of a piezoelectric material and DML substrate was performed. In these transducers, two different bonding methods such as SLID and conventional epoxy were implemented. Various combinations of factors such as element width, piezoelectric material thickness, intermetallic layer thickness and voids inside SLID were evaluated for SLID bonding method. Element width variation from 245 μm to 255 μm resulted in variance at vibrational modes, except thickness mode. A 3% shift in resonance region could be attributed to thickness variations in the piezoelectric plate, from 345 μm to 355 μm. Voids in the SLID bondline shift the resonances to lower frequency and introduce higher loss compared to the intact SLID layer.

Element width, piezoelectric material thickness and epoxy bond line were supposed to be primary factors causing variation in electrical impedance responses of transducer using conventional epoxy. Contributions from these sources on the electrical impedance of each element were studied and compared to Finite Element simulations using COMSOL. The results provided a substantial insight of essential reasons causing variance in array elements and a comprehensive comparison between these two bonding methods. In the light of these findings, we believe that our analysis may contribute to explanations of variation in fabricated transducer structure and applicaltion of SLID as a potential bonding method in bonding stacks of piezoelectric ultrasonic transducers at high frequencies. Future work will entail fabricating a complete transducer using SLID boding method.

## 6.2 Future works

Based on the results presented in this thesis, several interesting directions for future work are described as follows:

- Fabricate a linear transducer array with matching layers, explain the variance between array elements and compare to FEM simulations
- Fully characterize the properties of SLID bond line, especially void formation and its distribution inside SLID bondline
- Design and fabricate a linear array tranducer using SLID bonding method, including matching, and/or backing layers

# Bibliography


[1] W. Hendee and E. Ritenour, *Medical Imaging Physics, 4th Edition*. Wiley, 2003.

[2] T. Szabo, *Diagnostic Ultrasound Imaging: Inside Out, 2nd Edition,* Academic Press Series in Biomedical Engineering, Academic Press. 2013.

[3] J. Krautkramer and H. Krautkramer, *Ultrasonic Testing of Materials*, Springer-Verlag. 1983.

[4] A. Carovac, F. Smajlovic, and D. Junuzovic, "Application of Ultrasound in Medicine," *Acta Inform. Medica*, vol. 19, no. 3, pp. 168–171, Sep. 2011.

[5] K. Shung, "Ultrasound: Past, Present and Future - Springer," *J. Med. Biol. Eng.*, vol. 27, pp. 371–374, 2010.

[6] Lawrence E. Kinsler, Austin R. Frey, Alan B. Coppens, and James V. Sanders, *Fundamentals of Acoustics*. New York: John Wiley & Sons, 1982.

[7] Desilets CS, Fraser JD, and Kino GS, "The design of efficient broad-band piezoelectric transducers," *IEEE Trans Sonics Ultrason*, p. 25:115–25, 1978.

[8] Goldberg, RL., and Smith, SW, *The biomedical engineering handbook*. CRC Press, 1994.

[9] L. P. Tran-Huu-Hue, F. Levassort, N. Felix, D. Damjanovic, W. Wolny, and M. Lethiecq, "Comparison of several method characterise the high frequency behaviour of piezoelectric ceramics for transducer." ELSEVIER, 2000.

[10] Y. Chen, K. H. Lam, D. Zhou, W. F. Cheng, J. Y. Dai, H. S. Luo, and H. L. W. Chan, "High frequency PMN-PT single crystal focusing transducer fabricated by a mechanical dimpling technique," *Ultrasonics*, vol. 53, no. 2, pp. 345–349, Feb. 2013.

[11] J. Yuan, S. Rhee, and X. N. Jiang, "60 MHz PMN-PT based 1-3 composite transducer for IVUS imaging," in *2008 IEEE Ultrasonics Symposium*, 2008, pp. 682–685.

[12] S. T. Lau, H. Li, K. S. Wong, Q. F. Zhou, D. Zhou, Y. C. Li, H. S. Luo, K. K. Shung, and J. Y. Dai, "Multiple matching scheme for broadband 0.72Pb(Mg1⁄3Nb2⁄3)O3−0.28PbTiO3 single crystal phased-array transducer," *J. Appl. Phys.*, vol. 105, no. 9, May 2009.

[13] T. A. Ritter, T. R. Shrout, R. Tutwiler, and K. K. Shung, "A 30-MHz piezo-composite ultrasound array for medical imaging applications," *IEEE Trans. Ultrason. Ferroelectr. Freq. Control*, vol. 49, no. 2, pp. 217–230, Feb. 2002.

[14] K. K. Shung and M. Zippuro, "Ultrasonic transducers and arrays," *IEEE Eng. Med. Biol. Mag.*, vol. 15, no. 6, pp. 20–30, Nov. 1996.

[15] N. Hoivik and K. Aasmundtveit, "Wafer-Level Solid–Liquid Interdiffusion Bonding," in *Handbook of Wafer Bonding*, P. Ramm, J. J.-Q. Lu, and aike M. V. Taklo, Eds. Wiley-VCH Verlag GmbH & Co. KGaA, 2012, pp. 181–214.

[16] Thi Thuy Luu, "Solid Liquid Interdiffusion wafer-level bonding for MEMS packaging," PhD Thesis, Buskerud and Vestfold University College (HBV), 2015.

[17] J.-F. Gelly, D. M. Mills, F. Lanteri, C. E. Baumgartner, and S. G. Calisti, "Method for optimized dematching layer assembly in an ultrasound transducer," US7621028 B2, 24-Nov-2009.

[18] B. J. Savord and W. J. Ossmann, "Acoustic imaging systems adaptable for use with low drive voltages," US6685647 B2, 03-Feb-2004.

[19] W. Mason, "Electromechanical transducers and wave filters." Princeton, N.J-1948.

[20] M. Redwood, "Transient Performance of a Piezoelectric Transducer," *J. Acoust. Soc. Am.*, vol. 33, no. 4, pp. 527–536, Apr. 1961.

[21] R. Krimholtz, D. A. Leedom, and G. L. Matthaei, "New equivalent circuits for elementary piezoelectric transducers," *Electron. Lett.*, vol. 6, no. 13, pp. 398–399, Jun. 1970.

[22] Richard L. Goldberg, Michael J. Jurgens, David M. Mills, Craig S. Henriquez, David Vaughan, and Stephen W. Smith, "Modeling of Piezoelectric Multilayer Ceramics Using Finite Element Analysis," *IEEE Trans. Ultrason. Ferroelectr. Freq. CONTROL*, vol. 44, Nov. 1997.

[23] "High quality components and materials for the electronic industry," *Hejreskovvej 18A DK-3490 Kvistgard*, Denmark 2003.

[24] Magne Aanes Espen Storheim and Magne Vestrheim, and Per Lunde, "Ultrasonic piezoceramic transducers for air- finite element analysis and measurement." 2010.

[25] M.Aanes, E. Storheim, M. Vestrheim, and P. Lunde, "Finite element analysis and measurements of ultrasonic piezoceramic transducers in air and water."

[26] E.L. Nix, J. Corbett, J.H. Sweet, and M. Ponting, "Dicing and Grinding of Electro-Ceramics."

[27] J. M. Cannata and K. K. Shung, "A comparison of model and experiment for a high frequency (35 MHz) linear ultrasonic array," in *2003 IEEE Symposium on Ultrasonics*, 2003, vol. 2, p. 1658–1662 Vol.2.

[28] T. Tollefsen, A. Larsson, and O. M. Løvvik, "Au-Sn SLID Bonding—Properties and Possibilities," in *2011 The Minerals, Metals & Materials Society and ASM International*, 2011, vol. Vol. 43, p. 397.

[29] R. E. McKeighen, "Design guidelines for medical ultrasonic arrays," in *Medical Imaging'98*, 1998, pp. 2–18.

[30] K. Weinberg and T. Bohme, "Condensation and Growth of Kirkendall Voids in Intermetallic Compounds," *IEEE Trans. Compon. Packag. Technol.*, vol. 32, no. 3, pp. 684–692, Sep. 2009.

[31] H. Zhou, S. Qiu, Y. Huo, and N. Zhang, "High-speed dicing of silicon wafers conducted using ultrathin blades," *Int. J. Adv. Manuf. Technol.*, vol. 66, no. 5–8, pp. 947–953, Jul. 2012.

[32] M. D. Sherar and F. S. Foster, "The design and fabrication of high frequency poly(vinylidene fluoride) transducers," *Ultrason. Imaging*, vol. 11, no. 2, pp. 75–94, Apr. 1989.

[33] L. F. Brown, “Design considerations for piezoelectric polymer ultrasound transducers,” in *Proceedings of the 2000 12th IEEE International Symposium on Applications of Ferroelectrics, 2000. ISAF 2000*, 2000, vol. 1, pp. 265–270 vol. 1.

[34] Tomohisa Azuma, Junichi Yamazaki, Masayoshi Inoue, and Kazuo Miyabe, “Investigation of Spurious Mode in Piezoelectric Ceramic Resonators,” *J. Korean Phys. Soc.*, vol. 32, p. S1294~S1297, Feb. 1998.

[35] G. Piazza, P. J. Stephanou, and A. P. Pisano, “Piezoelectric aluminum nitride vibrating contour-mode MEMS resonators,” *Microelectromechanical Syst. J. Of*, vol. 15, no. 6, pp. 1406–1418, 2006.

[36] M. Lukacs, J. Yin, G. Pang, R. C. Garcia, E. Cherin, R. Williams, J. Mehi, and F. S. Foster, “Performance and characterization of new micromachined high-frequency linear arrays,” *IEEE Trans. Ultrason. Ferroelectr. Freq. Control*, vol. 53, no. 10, pp. 1719–1729, Oct. 2006.

## Publications

P1: **Duy Le-Anh**, Tung Manh, Lars Hoff, "A Study on Electrical Impedance Variations between Transducer Elements in One-Dimensional Piezoelectric Arrays", **submitted to** IEEE International Ultrasonics Symposium, 2016.

P2: Hoang-Vu Nguyen, Tung Manh, **Duy Le-Anh**, Knut Aasmundtveit, Lars Hoff, Tonni Franke Johansen, Trym Eggen, Frederic Lanteri, Jean-Francois Gelly, "Au-Sn Solid-Liquid Interdiffusion (SLID) bonding for Piezoelectric Ultrasonic Transducers", **submitted to** IEEE International Ultrasonics Symposium, 2016.